

**SOLUTION STRUCTURE AND BIOCHEMISTRY OF AN INTRAMEMBRANE
ASPARTYL PROTEASE (IAP)**

A Dissertation
Presented to
The Academic Faculty

by

Swe-Htet Naing

In Partial Fulfillment
of the requirements for the Degree
Doctor of Philosophy in Biochemistry

Georgia Institute of Technology

May 2018

Copyright © 2018 by Swe-Htet Naing

**SOLUTION STRUCTURE AND BIOCHEMISTRY OF AN INTRAMEMBRANE
ASPARTYL PROTEASE (IAP)**

Approved by:

Dr. Raquel Lieberman, Advisor
School of Chemistry and Biochemistry
Georgia Institute of Technology

Dr. Adegboyega (Yomi) Oyelere
School of Chemistry and Biochemistry
Georgia Institute of Technology

Dr. Loren Williams
School of Chemistry and Biochemistry
Georgia Institute of Technology

Dr. Pamela Peralta-Yahya
School of Chemistry and Biochemistry
Georgia Institute of Technology

Dr. Roger Wartell
School of Biological Sciences
Georgia Institute of Technology

Date Approved: Jan 25th, 2018

ACKNOWLEDGEMENTS

I would like to thank my research advisor, Dr. Raquel Lieberman for her endless guidance and support. In addition, I would like to thank Dr. Jason Drury, Dr. Sibel Kalyoncu and Dr. Jennifer Johnson for their contribution towards the foundation of my research project. I would also like to thank current and former members of Lieberman Lab: Dr. Shannon Hill, Dr. Dustin Huard, Dr. Rebecca Donegan and Athéna Patterson-Orazem for their insightful feedback and advice on my research; Jay Xingjian Tao, Iramofu Dominic, Federico Urbano-munoz, Casey Bethel, Elaine Nguyen, Chiamaka Ukachukwu, Michelle Womack-Davis for the smiles and laughter they brought to the lab; and undergraduate students including Jacqueline Harris, Afoma Umeano, Josh George, David Heaner, James Going, Michelle Kwon, Quincy Faber, Moya Tomlin, Hayeon Cho, Ivan Morales, James Rives and Dana Freeman for their help with our research experiments.

Next, I would like to thank my collaborators: Dr. Matthew Torres, Dr. David Smalley, Dr. Krishna Vukoti, Hyojung Kim and Alex Jonke for their fantastic mass spectrometric analysis of my experiments; Dr. Volker Urban, Dr. Ryan Oliver, Dr. Kevin Weiss and staffs at Oak Ridge National Laboratory (ORNL) for their help in obtaining successful solution structure of our intramembrane aspartyl protease; and Dr. Schmidt-Krey and Kasahun Neselu for their collaboration of cryo-EM crystallization. Special thanks to Dr. Julia Kubanek and College of Sciences at Georgia Institute of Technology for awarding me multiple travel grants to collect data at ORNL.

In addition, I would like to thank Williams Lab, Udit Brahmachari (Barry Lab), Wartell Lab, Prausnitz Lab, Shin Lab, Stephen Sarria and Amy Ehrenworth (Peralta-

Yahya Lab), Aaron McKee (Orlando Lab) and Pranav Kalelkar (Collard Lab) for their help with my research. I would also like to thank my thesis committee members, Dr. Loren Williams, Dr. Pamela Peralta-Yahya, Dr. Roger Wartell and Dr. Adegboyega (Yomi) Oyelere for their guidance and feedback towards my thesis dissertation.

Finally, I would like to thank my wonderful fiancé, Amanda Pierog, my mom and dad, my in-laws and my siblings. Your love, care and encouragement help me achieve my goals.

TABLE OF CONTENT

ACKNOWLEDGEMENTS	iii
LIST OF TABLES	viii
LIST OF FIGURES	ix
NOMENCLATURE.....	xii
SUMMARY	xvii
Chapter 1: Introduction to intramembrane proteases (IP)	1
1.1 Biology of intramembrane proteases (IP).....	1
1.1.1 Basic features of the four classes of IPs.....	1
1.2 Biology and biochemistry of IAPs	9
1.2.1 Biological roles of presenilin	9
1.2.2 Biological roles of SPP	10
1.2.3 IAP substrate requirements and specificity.....	10
1.3 Challenges working with IPs.....	11
1.4 IP involvement in human diseases.....	12
1.5 Thesis objectives.....	14
1.5.1 Development of a FRET-based IAP enzyme assay	14
1.5.2 Structure-function and substrate specificity of IAP	15
1.5.3 Solution structure of IAP using small-angle neutron scattering (SANS)	15
Chapter 2: Catalytic properties of intramembrane aspartyl protease substrate hydrolysis evaluated using a FRET peptide cleavage assay.....	17
2.1 Publication and author contributions.....	17
2.2 Introduction	17
2.3 Methods	21
2.3.1 Cloning, expression, and purification of MCMJR1 IAP variants	21
2.3.2 Standard assay and inhibitor studies	24
2.3.3 Data calibration and analysis.....	25
2.3.4 Circular dichroism (CD).....	26
2.3.5 Fluorescence polarization (FP).....	27
2.3.6 Bicelle preparation and reconstitution of IAP samples	27
2.3.7 Expression and purification of fusion protein substrate for gel assay.....	28
2.3.8 Gel-based enzyme assay with fusion substrate	29
2.3.9 In-gel protein digestion and LC-MS/MS analysis.....	30
2.4 Results and Discussion	32
2.4.1 Characterization of IAP and N-terminal deletion mutant IAP Δ N23	32
2.4.2 Development of a FRET-based assay	34
2.4.3 Kinetic analysis	38
2.4.4 Mode of inhibition of three small molecules	39

2.4.5	Gel-based assay	42
2.4.6	MS analysis.	43
2.4.7	Structure-function analysis of TM1.	50

Chapter 3: Both positional and chemical variables control in vitro proteolytic cleavage of a presenilin ortholog 52

3.1	Publication and author contributions	52
3.2	Introduction	52
3.3	Methods	54
3.3.1	Molecular biology	54
3.3.2	Expression and purification of enzyme variants and fusion substrates... ..	56
3.3.3	FRET assay and inhibitor studies	58
3.3.4	Gel-based assay	59
3.3.5	CD	60
3.3.6	SAXS and ab initio modeling.....	61
3.4	Results	62
3.4.1	Enzymatic analysis of mIAP mutants	62
3.4.2	Role of bulk water in mIAP catalysis.....	69
3.4.3	mIAP cleavage of the presenilin C100 substrate in the ‘ γ -site’ region... ..	69
3.4.4	mIAP cleavage of the presenilin C100 substrate in the ‘ ϵ -site’ region... ..	74
3.4.5	Probing substrate specificity by Thr-scanning within the MRS substrate 76	
3.5	Discussion.....	78

Chapter 4: Solution structure of an intramembrane aspartyl protease via small angle neutron scattering 82

4.1	Publication and author contributions	82
4.2	Introduction	82
4.3	Methods	84
4.3.1	Expression and Purification of Protonated and Deuterated MmIAP	84
4.3.2	Small-Angle Neutron Scattering Data Collection	87
4.3.3	SANS Data Analysis and Modelling.....	88
4.4	Results	89
4.4.1	SANS Analysis of d-MmIAP	89
4.4.2	Particle molecular volume estimates	94
4.4.3	Comparison to Crystal Structure and ab initio Modelling	96
4.5	Discussion.....	98

Chapter 5: Future directions 101

5.1	Introduction	101
5.2	Evaluate quantitatively the effects of FAD mutations within the C100 substrate on IAP kinetics and cleavage preferences	101
5.3	Clarify sequence preferences for IAP cleavage by expanding the substrate repertoire tested using assays developed in this thesis	102
5.4	Characterize the substrate-enzyme complex	104

REFERENCES.....	106
VITA	128

LIST OF TABLES

Table 2.1. Primers used for cloning and expression of IAPs.....	22
Table 2.2. Kinetic parameters of IAP and IAP Δ N23 using Ren390FRET substrate and inhibitors	35
Table 2.3. MRS cleavage reporter and control peptides observed by LC-MS/MS.	49
Table 3.1. Primers used for site-directed mutagenesis of enzyme IAP and substrates MRS and MCS	55
Table 3.2. Rationale of mIAP mutation and kinetics parameters associated with each mutant.	63
Table 3.3 Kinetic parameters obtained from mIAP cleavage of C100FRET in DDM and bicelles and effect of (ZLL) ₂ ketone inhibitor	72
Table 4.1. Summary of physical parameters from the SANS data, reconstructed DAM, and a related PDB entry (4HYC:A).	94
Table 5.1. Selected substrates where proposed cut site is underlined	103

LIST OF FIGURES

Figure 1.1. Structures of intramembrane proteases	3
Figure 1.2. PROMALS 3D sequence alignment of human presenilin-1 (accession P49768, PDB code 5FN5) and archael IAP (accession ABN57850, PDB code 4HYC)....	8
Figure 2.1. Illustration of FRET assay, chemical structures of fluorophores, quenchers, inhibitors and bicelle	20
Figure 2.2. Protein purification assessment by SDS-PAGE	29
Figure 2.3. Initial characterization of IAP and IAP Δ N23 constructs	33
Figure 2.4. Circular dichroism wavelength scan of substrate peptide (IHPFHLVIHTR) in PBS (0.05% DDM).	34
Figure 2.5. Fluorescence polarization and enzymatic analysis for angiotensinogen substrate	36
Figure 2.6. Assessment of initial catalytic rates for FRET assay	37
Figure 2.7. Assay calibration	37
Figure 2.8 . Inhibitor studies to determine mode of inhibition using Ren390FRET substrate	41
Figure 2.9. Gel cleavage assay using fusion protein substrate MBP-IHPFHLVIHT-SUMO	43
Figure 2.10. Mass spectrometric analysis of cleavage sites.....	45
Figure 2.11. Mass spectrometric analysis	47

Figure 2.12. Relative PSMs of cleavage products formed by IAP and IAP Δ N23 from two biological replicate indicated as experiment A and B. The LC-MS/MS analysis was carried out in 4 replicates (Rep1-4).	48
Figure 3.1. Characterization of mIAP mutants	64
Figure 3.2. SAXS analysis of MRS _{WT} substrate	65
Figure 3.3. Biophysical characterization of mIAP mutants	66
Figure 3.4. All LC-MS replicates for MRS substrates cut by mIAP mutants. MRS cleavage profile processed by (A) WT mIAP, (B) Y161A, (C) Y161F, (D) G219A, (E) Q272A, (F) L275F	68
Figure 3.5. C100FRET assay development	70
Figure 3.6 mIAP cleavage of C100 γ -site	71
Figure 3.7. All LC-MS replicates for MCS-related substrates cut by mIAP WT.....	73
Figure 3.8. MS analysis of MCS10 substrate incubated with mIAP in H ₂ ¹⁸ O.	73
Figure 3.9. Gel assay using MCS15 substrate	75
Figure 3.10. mIAP cleavage of C100 ε -site	75
Figure 3.11. Probing substrate specificity of IAP using MRS Thr-scanning mutants.....	77
Figure 3.12. All LC-MS replicates for MRS mutant substrates cut by mIAP WT.....	78
Figure 4.1. d-MmIAP purification	87
Figure 4.2. Preliminary (A) SAXS and (B) SANS data collected for solutions of micelles (DDM – unfilled markers) and the protein-detergent complex (PDC – filled markers) ..	90

Figure 4.3. SANS contrast match point measurements for DDM micelles, MmIAP with DDM, d-MmIAP with DDM (22% D ₂ O), and d-MmIAP with DDM / d25-DDM mixed micelles (48.5% D ₂ O)	91
Figure 4.4. SANS data obtained for d-MmIAP with contrast-matched DDM / d25-DDM mixed micelles (48.5% D ₂ O)	93
Figure 4.5. Determination of protein molecular weight from the SAS invariant Q _R	94
Figure 4.6. CRYSON results and comparison to SANS data.	98

NOMENCLATURE

Å	Angstrom
ABC	Ammonium bicarbonate
Afu	Arbitrary fluorescence units
Aph-1	Anterior pharynx-defective 1
APP	Amyloid precursor protein
A β	Amyloid beta peptide
C100	C-terminal 100 amino acids of amyloid precursor protein
CD	Circular dichroism
CHAPSO	3-([3-cholamidopropyl]dimethylammonio)-2-hydroxy-1-propanesulfonate
CMP	Contrast match point
CV	Column volume
D ₂ O	Deuterated water
Da	Dalton
DABCYL	[4-((4-(dimethylamino)phenyl)azo)benzoic acid]
DAPM	N-[N-3,5-Difluorophenacetyl]-L-alanyl-S-phenylglycine methyl ester
DAPT	N-[(3,5-Difluorophenyl)acetyl]-L-alanyl-2-phenyl]glycine-1,1-dimethylethyl ester
DDM	n-dodecyl- β -D-maltoside
Dmax	Maximum interatomic distance
DMPC	Dimyristoyl phosphatidylcholine

DMSO	Dimethyl sulfoxide
DNA	Deoxyribonucleic acid
DNP	2-nitrophenol
DTT	Dithiothreitol
<i>E. coli</i>	Escherichia coli
EDANS	5-[(2-aminoethyl)amino]naphthalene-1-sulfonic acid
EDTA	Ethylenediaminetetraacetic acid
EGFR	Epidermal growth factor receptor
ELISA	Enzyme-linked immunosorbent assay
EM	Electron microscopy
ER	Endoplasmic reticulum
FAD	Familial Alzheimer's disease
FITC	Fluorescein isothiocyanate
FPLC	Fast protein liquid chromatography
FRET	Förster Resonance Energy Transfer
GSI	γ -secretase inhibitor
H ₂ ¹⁸ O	Water with ¹⁸ O isotope
HLA	Human leukocyte antigen
HRP	Horse radish peroxidase
IAP	Intramembrane aspartyl protease
IP	Intramembrane protease
IPTG	Isopropyl- β -D-1-thiogalactopyranoside
k _{cat}	Turnover number

K _d	Dissociation constant
K _i	Inhibitor constant
K _m	Substrate concentration at half maximal velocity
L	Liter
L1	Amphiphilic loop 1
LB	Luria broth
LC-MS/MS	Liquid chromatography-tandem mass spectrometry
M	Molar
MALDI	Matrix Assisted Laser Desorption Ionization
MALS	Multi-angle light scattering
MBP	Maltose binding protein
MCMJR1	<i>Methanoculleus marisnigri JR1</i>
MCS10	MBP-GGVVIATVIV-SUMO
MCS15	MBP-GGVVIATVIVITLVM-SUMO
MCSGG	MBP-GGVIVITLVM-SUMO
MCSTV	MBP-TVIVITLVML-SUMO
MHC	Major histocompatibility complex
MRS	MBP-IHPFHLVIHT-SUMO
MW	Molecular weight
MWCO	Molecular weight cut-off
N _A	Avogadro's number
NMA	N-methyl anthranilate
NMR	Nuclear magnetic resonance

NSD	Normalized spatial discrepancy
Θ	Molar ellipticity
OD ₆₀₀	Optical density at 600 nm
ORNL	Oak Ridge National Laboratory
P(r)	Pair-distance distribution function
PBS	Phosphate-buffered saline
PDB	Protein data bank
PDC	Protein detergent complex
PEN	Presenilin enhancer 2
PSH	Presenilin homolog
PSM	Peptide spectral matches
PVDF	Polyvinyl difluoride membrane
Q	Scattering vector
R.M.S.D.	Root mean square deviation
RceI	Ras and α -factor converting enzyme I
Ren390FRET	Renin 390 FRET
RF	Restriction free cloning
R _g	Radius of gyration
S2P	Site-2-proteases
SANS	Small-angle neutron scattering
SAXS	Small-angle X-ray scattering
SDM	Site-directed mutagenesis
SDS-PAGE	Sodium dodecyl sulfate polyacrylamide gel electrophoresis

SEC	Size exclusion chromatography
SLD	Scattering length density
SPP	Signal peptide peptidase
SREBP	Sterol regulatory element-binding protein
SUMO	Small ubiquitin-like modifier
TM	Transmembrane
T _m	Melting temperature
V	Initial velocity
V _{max}	Maximal velocity
w/v	Weight/volume
λ _{em}	Emission wavelength
λ _{ex}	Excitation wavelength
(ZLL) ₂ ketone	1,3-di-(N-Carboxybenzoyl-L-leucyl-L-leucyl)aminoacetone

SUMMARY

Intramembrane proteases (IPs) play important roles in numerous biochemical processes in all kingdoms of life, including cell differentiation, development and metabolism. IPs are attractive targets for therapeutics development and have been implicated in the pathogenesis of human diseases, such as Alzheimer's disease, Hepatitis C, malaria and a variety of cancers. Despite their broad medical and biological relevance, structural and mechanistic details of IPs have remained largely obscure.

Intramembrane aspartyl proteases (IAP) are one of the four classes of IPs, and the least understood. Typically, discontinuous assays are used to study the biochemistry of IAPs. A major disadvantage of discontinuous assays is that the catalytic parameters, substrate preferences and modes of inhibition are difficult to extract with high degree of sensitivity and certainty. Therefore, in Chapter 2, I developed a continuous FRET peptide assay. The assay is fast, robust, and high throughput, and can be applied to screen multiple conditions simultaneously. In collaboration with the Torres Lab (School of Biological Sciences), we developed a liquid chromatography tandem mass spectrometry method (LC-MS/MS) to detect the cleavage sites with high-resolution. Catalytic parameters and cleavage sites of a fortuitous substrate, angiotensinogen, in detergent and bicelles condition were evaluated. In addition, the modes of inhibition of well-established IAP-directed inhibitors were identified.

Chapter 3 applies the methodology of Chapter 2 for structure-function analysis of a model IAP from the archaeon *Methanoculleus marisnigri* JR1 (mIAP). IPs are notorious as promiscuous enzymes where there is no consensus on substrate cleavage

motif; yet, IAPs are believed to be highly regulated so as to not accidentally deactivate proteomes. The catalytic effects of mutations on conserved catalytic and gating motifs, and familial Alzheimer's disease mutations on mIAP proteolysis were evaluated to shed light on the proteolytic mechanism, substrate recognition and gating. Utilizing LC-MS/MS, the cleavage profiles of substrate obtained after mutant mIAP cleavage were compared to understand how mIAP mutations affect processivity and specificity of cleavage. To probe factors influencing substrate specificity of mIAP, such as chemical preference towards particular amino acid residue and positional preference on a particular substrate sequence, a series of substrates, including mutants of the angiotensinogen sequence as well as the C-terminal region of amyloid precursor protein involved in Alzheimer disease, were generated and cleavage reactions with mIAP were evaluated.

Finally, in Chapter 4, I present a small-angle neutron scattering (SANS) study of mIAP. The oligomeric state of IAPs has been a subject of debate, with proposals from monomer through octamer. The presence of detergent or other amphiphilic systems required to solubilize and stabilize membrane proteins hinders structural characterization using standard analytical techniques such as size exclusion chromatography (SEC) coupled with multi-angle light scattering (MALS), or small-angle X-ray scattering (SAXS). SANS offers a unique feature that can highlight membrane protein rendering detergent micelles invisible by matching the scattering length density of solvent with that of detergent. This study was done in collaboration with the Biological Neutron Scattering group at Oak Ridge National Laboratory.

1 Chapter 1: Introduction to intramembrane proteases (IP)

1.1 Biology of intramembrane proteases (IP)

Intramembrane proteolysis is a biochemical process in which a membrane-embedded substrate is hydrolyzed within the transmembrane (TM) helix by an intramembrane protease (IPs) to release a biologically active peptide/protein that in turn translocates to different regions of the cell to elicit a biological function (1).

Intramembrane proteolysis plays an important role in cell metabolism, development and differentiation in organisms throughout the kingdoms of life (2). Eukaryotic IPs are composed of several membrane-spanning helices embedded in the membrane of endoplasmic reticulum (ER), Golgi, cell membrane. IPs are essential in cell signaling cascade that control metabolism, and control activation of transcription factors that then influence expression of different genes (1-4). Dysfunction of IPs lead to a multitude of diseases (5-7). As such, IP inhibition is a broad strategy in related drug development (8,9). Despite their biomedical importance, little is known about the mechanism and substrate specificity of IPs.

1.1.1 Basic features of the four classes of IPs

IPs are divided into four distinct classes based on their key catalytic nucleophile: (1) serine proteases called rhomboids, (2) Zn-dependent metalloproteases or site-2-proteases (S2P) (3) glutamate proteases and (4) aspartyl proteases (IAPs). IPs are found in all kingdoms of life except glutamate protease which is only found in eukaryotes (10-13). In *Drosophila melanogaster*, rhomboid is the primary regulator of epidermal growth factor receptor (EGFR) signaling pathway controlling the organismal development (14).

Mutations in rhomboid are found to be associated with developmental defects in *Drosophila* embryo (15,16). In addition, rhomboids play essential roles in other signaling pathways found in invasion of parasites (17) and quorum sensing of bacteria (18,19). In humans, rhomboid dysfunction has been linked to several diseases including Parkinson's disease, malaria infection and colorectal cancer (17,20-23).

Out of the four classes of IP, rhomboids are the best studied with several crystal structures available from various organisms. Rhomboids utilize a catalytic dyad containing Ser and His during proteolysis rather than utilizing a classical Asp-Ser-His catalytic triad of soluble serine proteases (24,25). The catalytic residues are buried at the bottom of a V-shaped cavity, about 10-12 Å away from the membrane surface (26). Catalytic Ser and His are located on TM4 and TM6 respectively (Figure 1.1A). Histidine is thought to activate Ser for direct nucleophilic attack on the substrate during proteolysis (27). Two models were initially proposed for substrate gating in which substrate is thought to enter active site via a lateral gate, which could be formed by amphiphilic loop 1 (L1) (28) or TM5 (26,29,30). The amphiphilic characteristic of L1 forms a lid between the active site and lipid, so movement of L1 could open up the path between TM1 and TM3 for substrate entry into the active site (28). Alternatively, and more convincingly, substrate could enter via lateral gate involving TM5 (29,30) (Figure 1.1A). Outward bending of TM5 is thought to create a lateral opening where substrate could enter the active site (26).

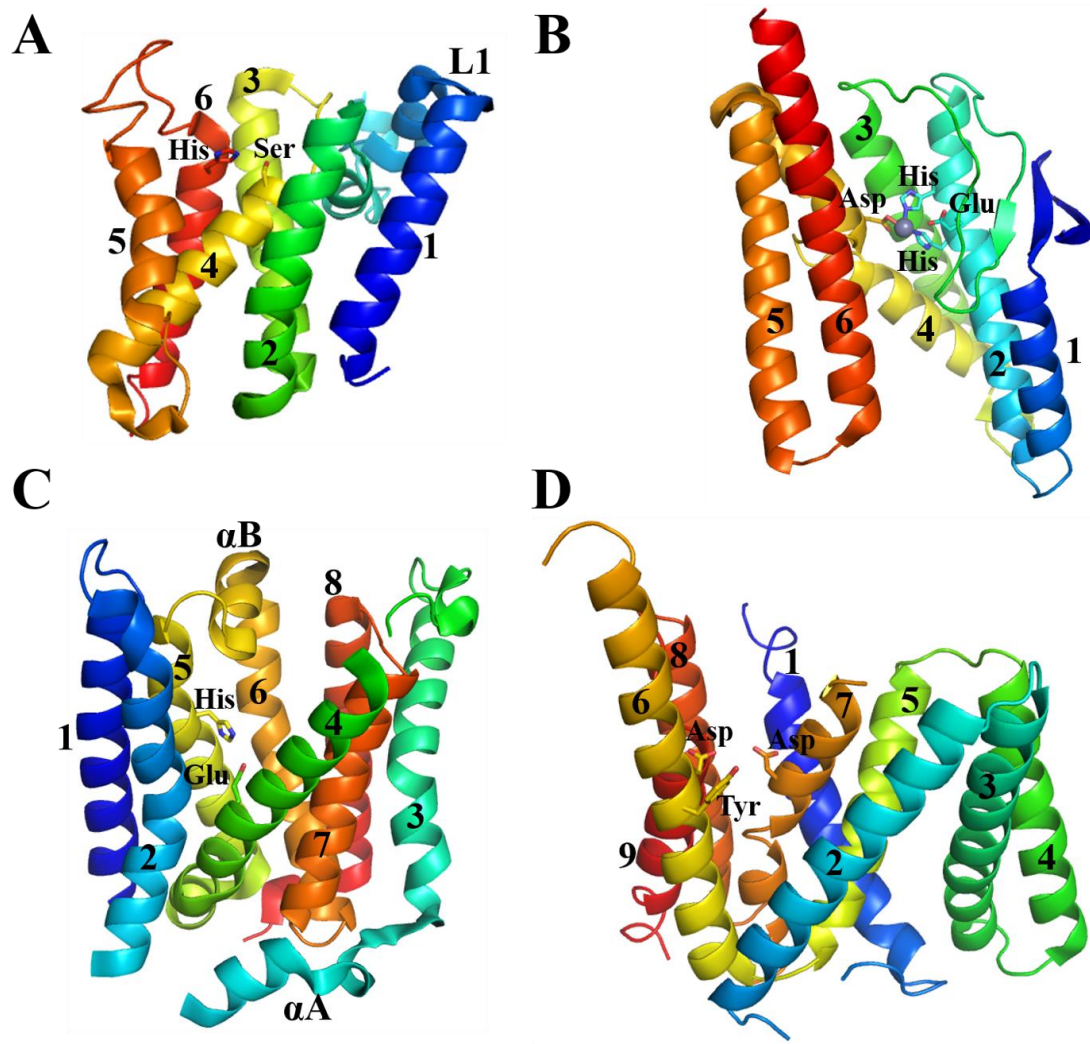


Figure 1.1. Structures of intramembrane proteases. (A) Rhomboid protease containing six TM helices, loop 1 (L1) and catalytic dyad Ser-His. (B) Site-2-protease containing six TM helices, zinc molecule (shown by gray sphere) coordinated to two His and an Asp residue, and Glu that is the activator of water for nucleophilic attack on scissile bond. (C) Glutamate protease, RceI, containing eight TM helices, catalytic Glu and His and peripheral helices αA and αB . (D) Aspartyl protease, presenilin homolog, containing nine TM helices and catalytic motifs, YD...GxGD.

Kinetic studies on rhomboid have raised a controversy about intramembrane proteolysis process. One study, using a biological substrate peptide consisting of a lipid-quenched fluorescein isothiocyanate (FITC) fluorophore, provocatively argued that intramembrane proteolysis by rhomboid is governed by turnover number (k_{cat}), not by substrate affinity (31). Screening structural variants of biological substrate yielded a weak affinity in high micromolar range for all substrate variants but a significant difference in k_{cat} among substrate variants tested. On the contrary, two other studies, utilizing a fluorescent casein or fusion substrate containing a cyan and yellow fluorescence proteins as a FRET pair, suggest a more conventional scenario in which substrate affinity plays an important role in intramembrane proteolysis (10,32).

In two studies with rhomboids, a specific sequence recognition motif has been identified (33,34). Seven residues on either side of the cleavage site were examined via mutagenesis to understand the substrate protein primary structural determinant on the substrate specificity of rhomboids. Three residue positions, P4 (fourth residue N-terminal to the cut site), P1 (first residue N-terminal to the cut-site) and P2' (second residue C-terminal to the cut site), were identified to be crucial in specificity, rate and efficiency of cleavage (33). While P4 position requires large and hydrophobic residues, P1 position prefers amino acids with small side chain and P2' position favors hydrophobic side chains regardless of their size. The aforementioned requirements at P4, P1 and P2' extend to diverse substrate proteins from prokaryotes and eukaryotes suggesting that the identified motif might be relevant to evolutionarily distant rhomboids (33,34).

S2P is a zinc-dependent metalloprotease mainly involved in cholesterol metabolism (35). In response to low level of cellular cholesterol, membrane-bound transcription factor called sterol regulatory element-binding protein (SREBP) is translocated from the ER to the Golgi apparatus, where it is sequentially cleaved by site-1-protease (S1P) and S2P (36,37). In the Golgi, S1P cleaves SREBP at its luminal loop, thus separating two transmembrane segments. S2P then cleaves the first transmembrane segment within lipid bilayer to release a mature amino-terminal (N-terminal) portion of SREBP, which in turn enters nucleus to activate transcription of genes that control biosynthesis and uptake of cholesterol (38,39).

S2P consists of six transmembrane helices (TM1 – TM6) (40). TM helices 2,3 and 4 together form the core domain of S2P, which has conserved amino acid sequence and conserved active site conformation across various species. In the core domain of S2P, TM 2 and 4 are stabilized by TM3. The active-site contains the catalytic zinc atom coordinated by two histidines in TM2 and one aspartate in TM4 (Figure 1.1B) (40). The zinc atom is ~14 Å from the membrane surface. S2P is crystalized in a closed and open conformation. Compared to the closed state, TM1 and TM6 are 10-12 Å farther apart in the open conformation. In the closed state, the active site is embedded in the transmembrane helices and is impermeable to the substrate peptide. However, water molecules, which are key for hydrolysis, can travel to the zinc ion in the active site via a polar, central channel that opens to the cytosolic side of the cell membrane. A glutamate residue is thought to activate the water molecule to initiate nucleophilic attack on substrate. The open conformation exposes the active site to the substrate entry via the deep groove that run roughly parallel to the TM segments. The conformational change

from closed to open state is thought to occur through the lateral gating mechanism in which two sides of the gates (ie. TM1 and TM6) move away from each other. It is still not clear if the substrate enters the active site between TM1 and TM2 or between TM6 and the core domain.

The glutamyl zinc-containing intramembrane protease, RceI (Ras and α -factor converting enzyme I) is a more recent addition to IPs because it utilizes catalytic glutamate residue that is distinct from three other classes of IPs (41). In addition, RceI has no sequence similarity to other IPs and strong evidence indicates that RceI is not a metalloenzyme because it can function without zinc (41,42). RceI was first identified in *Saccharomyces cerevisiae* as a type II CAAX prenyl endopeptidase (where C is cysteine, A is an aliphatic amino acid and X is any amino acid) (12,43). RceI is involved in the three-step posttranslational modification of CAAX proteins which affect multiple signaling pathways that control differentiation, proliferation and oncogenesis (44,45). First, a CAAX protein is prenylated with a help of prenyl-transferase, which attaches 15-carbon farnesyl or 20-carbon geranylgeranyl moiety to the cysteine of CAAX motif at the carboxy terminal (C-terminal). The prenylated CAAX protein is then cleaved by RceI releasing the last three amino acids (-AAX) and exposing isoprenyl cysteine which is further modified via methyl esterification. The cleavage of CAAX protein by RceI is required for proper localization (46). Germline knockout of *RceI* results in embryonic lethality in mice suggesting the importance of RceI in organismal development (47,48).

The RceI is composed of eight transmembrane helices (TM1-8) and two peripheral helices (α A and α B), which make it topologically distinct from other IPs (Figure 1.1C). Four transmembrane helices (TM4-7) are surrounded by less conserved

TM1-3 and TM8. A large conical cavity contains catalytic dyad, Glu and His, at the top of the cavity which open wide to the cytoplasm allowing unrestricted solvent access to the active site (41). Catalytic Glu, whose pKa is potentially raised by contacting two conserved Trp residues, is thought to deprotonate water for nucleophilic attack on the scissile bond. The oxyanion transition state is proposed to be stabilized by His and Asn, which are positioned on successive helical turns of TM7 opposite to the catalytic dyad. Protonation of the leaving amino group on the AAX tripeptide could perhaps be catalyzed by either residue of catalytic dyad, Glu or His. Substrate is proposed to enter active site laterally between TM2 and TM4. A large volume catalytic conical cavity is thought to accommodate various sizes of prenylated substrate proteins.

IAPs, the fourth class of IPs and the IP characterized in this thesis, is involved in various cellular processes such as cell differentiation, development, immune surveillance and viral maturation (2). IAP utilizes membrane-embedded two aspartic residues, which are located on two adjacent TM helices, during catalysis. Presenilin and signal peptide peptidase (SPP) are key members of IAP family. Although presenilins were once thought to be only found in vertebrates, bioinformatics analysis suggest that the presenilin-like proteins are present in fungi, plants and archaea (13).

```

Conservation:
P49768.1psn      1  MTELPAPLSYFQNAQMSSEDNHLSNTVRSQNDNRERQEHNDRRSLGHPEPLSNGRPQGNRSQVVEQDEED  70
5fn5_chainB_p002 1  -----EED  3
ABN57850.1mcm    1  -----MQIR-----  4
4hyc_chainA_p001 1  -----R-----  1
Consensus_aa:    .....
Consensus_ss:    hhh      hhh      hhhh      hhhhhhhhhhhh

Conservation:
P49768.1psn      71  EELTLKYGAKHVMILFVPVTLCLMVVVVATIKSVSF--YTRKDGQLIYTPFTEDTETVGQRALHSILNAAI  138
5fn5_chainB_p002  4  EELTLKYGAKHVMILFVPVTLCLMVVVVATIKSVSF--YTR-----  41
ABN57850.1mcm     5  -----DWLPLLGMPLMLLFVQIIAIVLVMP-MQAAGLV-----AF-----EDPESV-----ANPLI  49
4hyc_chainA_p001  2  -----DWLPLLGMPLMLLFVQIIAIVLVMP-MQAAGLV-----A-----PSSV-----ANPLI  43
Consensus_aa:    .....shb.ll.h.l.lhhbllhllhbs..b..h.....

Conservation:
P49768.1psn      139  MISVIVMTILLVVLKYRCYKVIHAWLIISLLLLFFFSFIYLGVEVFKTYNVAVD--YITVALLIWNFG  206
5fn5_chainB_p002  42  -----IISLLLLFFFSFIYLGVEVFKTYNVAVD--YITVALLIWNFG  81
ABN57850.1mcm     50  FIGMLLAFTLVLLVLLRTGGRRFI----AAFIGFALFMTFLYIFGALSLLALGPTTAAAGTLIGAVAVT  115
4hyc_chainA_p001  44  FIGMLLAFTLVLLVLLRTGGRRFI----AAFIGFALFMTFLYIFGALSLLALGPTTAAAGTLIGAVAVT  109
Consensus_aa:    .....hh...hLfh.hhhhG.l.bhh.sshs..hshhll.hshs

Conservation:
P49768.1psn      207  VVGMISIHMKGPLRLQQAYLIMISALMALVFIKYL-PEWTAWLILAVISVYDLVAVL-CPKGPLRMLVET  274
5fn5_chainB_p002  82  VVGMISIHMKGPLRLQQAYLIMISALMALVFIKYL-PEWTAWLILAVISVYDLVAVL-----  137
ABN57850.1mcm     116  ALLY----LYPEWYVIDILGVLISAGVASIFGI-SLAVLPVLVLLVLLAVYDAISVYRTK-----HMITL  175
4hyc_chainA_p001  110  ALLY----LYPEWYVIDILGVLISAGVASIFGI-SLEPLPVLVLLVLLAVYDAISVYRTK-----HMITL  169
Consensus_aa:    h1.h....hbs.h.lbphh.lhISA.hA.lf.b....hshhllhlltvydhltvh.....

Conservation:
P49768.1psn      275  AQERNETLFPAL-IYSSTMVWLVNMAEGDPEAQRVSKNSKYNAESTERESQDTVAENDDGGFSEEWAEQ  343
5fn5_chainB_p002  176  AEGVLETKAPIMVVVVKRADYSFRKEGLNISEG-----  208
ABN57850.1mcm     170  AEGV-----  173
Consensus_aa:    .....

Conservation:
P49768.1psn      344  RDSHLGPHRSTPESRAAVQELSSSILAGEDPEERGVKLGDFIFYSVLVGKASATASG-----DWNTT  407
5fn5_chainB_p002  138  -----CPVKLGLGDFIFYSVLVGKASATASG-----DWNTT  168
ABN57850.1mcm     209  -----EERGAFVMGMGDLIMPSILVASSHVFDAPAVLWTLASPT  248
4hyc_chainA_p001  174  -----GAFVMGMGDLIMPSILVVSSHVF-----LSAPT  201
Consensus_aa:    .....sh.hghGdhIh.SllVsptph.....sst

Conservation:
P49768.1psn      408  IACFVAILIGLCLTLLLLAIFKKALPALPISITFGLVFYFATDYLVPFMDQLAFHQFYI  467
5fn5_chainB_p002  169  IACFVAILIGLCLTLLLLAIFK----LPISITFGLVFYFATDYLVPFMDQLAFHQFYI  223
ABN57850.1mcm     249  LGAMVGSVLVGLAVLLYFVNKGN-PQAGLPPLNGGAILGF-LVGAALA----GSFSWLPF-  301
4hyc_chainA_p001  202  LGAMVGSVLVGLAVLLYFVNKGN-PQAGLPPLNGGAILGF-LVGAALA-----  246
Consensus_aa:    1tthvt.LlGLtlhLhlsb.p.....LP...s.tll.@.hhshh1.....

```

Figure 1.2. PROMALS 3D sequence alignment of human presenilin-1 (accession P49768, PDB code 5FN5) and archael IAP (accession ABN57850, PDB code 4HYC). Alignment conducted in PROMALS3D (49).

Both presenilin and SPP are composed of 6-9 TM helices (Figure 1.1D). Despite their low sequence identity of 19%, presenilin and SPP share catalytic motifs, YD (TM6)...GxGD (TM7) (where Y is tyrosine, G is glycine, D is aspartate and x is any

amino acid) (50-55); similarities extend to microbial orthologs (Figure 1.2) (51-53,56). However, the roles of 'Y' and 'G' in the signature motifs are not clear. Presenilin and SPP are inhibited by the same transition state analog (50-53) suggesting a conserved active site. Structural comparison of presenilin and SPP shows a nearly perfect register of the catalytic aspartates and similar features at active site (57). However, presenilin and SPP have opposite membrane topology which could be related to the fact that presenilin cleaves type I membrane proteins (where carboxyl-terminal faces cytosol) whereas SPP cleaves type II membrane proteins (where amino-terminal faces cytosol) (58). Although presenilin requires the other subunits of the γ -secretase complex for optimal activity, SPP does not require any other component for its activity (58-60). Finally, it has been proposed that conserved motif, Pro-Ala-Leu (PAL) on TM9 in presenilin could be involved in substrate recognition and gating (61-63).

1.2 Biology and biochemistry of IAPs

1.2.1 Biological roles of presenilin

A well-known involvement of presenilin is its role in cleaving substrates implicated in Alzheimer's disease (Section 1.4) but presenilin has been found to carry out multiple functions beyond the catalytic role for γ -secretase. Presenilin has been identified to be involved in protein trafficking, calcium homeostasis, and cell signaling pathways (64). For example, it has been reported that presenilin mutations promote the release of Ca^{2+} from overloaded ER stores leading to the abnormal intracellular calcium signaling (65). Presenilin may also function as a low-conductance, passive ER Ca^{2+} leak channel (66). Finally, presenilin negatively regulates the level of β -catenin, which is a signal transducer protein as well as cell adhesion molecule, by physically interacting with β -

catenin via the cytosolic loop of presenilin (67-71). In presenilin-deficient mice, the β -catenin signaling is enhanced leading to the development of skin cancer (72).

1.2.2 Biological roles of SPP

SPP is found in bacteria, archaea and eukaryotes including fungi, protozoa, plants and animals highlighting its physiological importance (13,58). SPP cleaves the remnant signal peptides remaining in the ER membrane after cleavage by signal peptidase, a soluble enzyme (51,73). SPP initiates the immune response by cleaving the signal peptide of polymorphic major histocompatibility complex (MHC) class I molecule, which then generate human leukocyte antigen (HLA) epitope. (74). In addition, SPP is involved in maturation of pathogens such as Hepatitis C virus and malaria parasites (75-77). Loss-of-function studies of SPP in various animal models demonstrate the essential role SPP plays in development. For example, antisense-mediated SPP knockdown in zebrafish resulted in developmental defects and neuronal cell death (78). Likewise, SPP deficient larvae of *Drosophila* have abnormal tracheae and died early (79). Exogenous addition of active SPP rescues normal development of *Drosophila* larvae, suggesting that the intramembrane proteolysis by SPP is crucial in larval development (79).

1.2.3 IAP substrate requirements and specificity

Currently, there are about 90 substrates identified for γ -secretase and 30 substrates for SPP, and no consensus motif for substrate cleavage has emerged (5,59). For both presenilin and SPP, most substrates are the products of another protease; β -secretase cleaves APP to provide C100 substrate for presenilin and signal peptidase cleaves its substrate to provide signal peptide for SPP (80-82). Although substrate transmembrane orientation and ectodomain length were initially thought to be required features for IAP

hydrolysis, substrates that fail to follow those two rules have been reported, suggesting that factors influencing substrate recognition are more complex (83). γ -secretase does not seem to recognize the scissile bond by TM depth as it is capable of cleaving at various sites throughout a given TM substrate (84-86) and comparative analysis of substrates reveals high variability in amino acid sequence and length (87,88). It has also been suggested that helix-breaking residues within TM helix at or around the scissile bond are required for the cleavage. This feature is thought to destabilize the TM helix by unwinding it, thereby exposing the scissile bond to the protease (80,89,90). However, there are examples of canonically helical cleavage sites in the literature (51,52). In sum, it is still unclear how intramembrane proteases differentiate substrates from non-substrates.

1.3 Challenges working with IPs

Working with membrane proteins like IAPs in the laboratory is notoriously challenging. First, IAPs are not soluble in aqueous solution, so mild detergents or other chemicals that can mimic the physiological lipid bilayer are required in order to retain the enzyme in an active state *in vitro*. Determination of suitable detergent or lipid system, and concentrations of these reagents, varies on a case-by-case basis and is empirically evaluated. Low and high detergent concentrations can be detrimental to the enzyme, rendering the membrane protein insoluble and denatured. Detergents can also interfere with the downstream analysis tools such as mass spectrometry (MS), circular dichroism (CD), nuclear magnetic resonance (NMR) and ligand-binding studies (91). In the case of MS, the presence of detergent interferes with protein digestion by commonly used soluble proteases (92,93). The ability of resulting cleaved peptides to bind to the chromatography column is also influenced by detergent. The final peptide peak

intensities are often reduced because detergent interferes with analyte ion signals, interfering with detection (94-96). In the case of CD, the hydrophobic and anisotropic nature of detergent gives rise to spectral artifacts such as solvent-induced wavelength shifts, differential light scattering and absorption flattening (97). The dielectric constant ($\sim 1-2$) of hydrophobic core of detergent is considerably lower than that of water (~ 80) causing bathochromic and hypsochromic shifts in CD spectrum of membrane proteins (98,99). Differential light scattering and absorption flattening, caused by detergent, influences the magnitudes and ratios of different peaks, thereby distorting the shape of the CD spectrum (100-102). In the case of NMR, membrane protein associated with detergent micelles tumbles as part of a larger complex leading to signal broadening, poor sensitivity and reduced spectral resolution (103).

1.4 IP involvement in human diseases

IPs are attractive targets for drug development due to their involvement in the pathogenesis of various human diseases. Mitochondrial rhomboid has been of interest in therapeutic development for type 2 diabetes and Parkinson's disease (21). Functionally impaired rhomboid has been detected in patients with Parkinson's disease raising the possibility of rhomboid inhibition as a viable strategy to increase mitophagy as a treatment for Parkinson's disease (104). Recently, S2P has been proposed as a novel therapeutic target for castration-resistant prostate cancer (105). Nelfinavir, originally developed as an HIV protease inhibitor, inhibits S2P, leading to accumulation of SREBPs, which in turn increases apoptosis for castration-resistant prostate cancer (105). RceI is a drug target in anticancer therapy. Inhibition of RceI disrupts the posttranslational modification of its substrate Ras, a family of membrane-bound G

protein involved in mitogen-activated protein kinase signaling pathway, which is linked to tumor growth (106).

Presenilin was first identified through genetic linkage studies of families with early onset familial Alzheimer's disease (FAD) (107). Presenilin is the catalytic subunit of γ -secretase, which also contains nicastrin, anterior pharynx-defective 1 (Aph-1), presenilin enhancer 2 (PEN-2) (64). All four protein components, which exist at 1:1:1:1 stoichiometry (108), are required for the optimal enzymatic activity (109,110). Nicastrin is a single span membrane protein with a large, heavily glycosylated extracellular domain and is thought to assist in substrate selection (111). Aph-1, which is composed of seven TM helices, promotes the assembly, stabilization and trafficking of γ -secretase complex (112). PEN-2, which is composed of two TM helices, triggers presenilin endoproteolysis into N- and C-terminal fragments that together are catalytically competent (113-115). Amyloid precursor protein (APP) is the key substrate of γ -secretase involving in the onset of Alzheimer's disease. APP is initially cleaved by a soluble aspartyl protease, β -secretase, to produce a membrane-bound carboxyl-terminal fragment commonly known as C100 or C99, which in turn is cleaved by γ -secretase sequentially to liberate various length of amyloid- β (A β) peptides. Data to date indicate that γ -secretase cleaves within C100 at two membrane-embedded sites, first within the so-called ϵ -site to generate 48- and 49-mer peptides (A β 48 and A β 49), then at the γ -site to release shorter fragments A β 38, A β 40 and A β 42 (116). Among the cleavage products of γ -secretase, A β 42 is particularly prone to aggregation and is a component of the amyloid- β plaques in the brain of Alzheimer patients (64).

In addition to its major role in Alzheimer's disease, γ -secretase has been associated with various cancers including breast cancer, lung cancer, colorectal cancer and T-cell acute lymphoblastic leukemia due to its cleavage of Notch (117). To date, clinical trials of γ -secretase inhibitors (GSIs) as a therapeutic for Alzheimer's disease, have failed due to their severe side effects that rise from simultaneous inhibition of APP and other γ -secretase substrates like Notch (118). In sum, it is essential to understand the physicochemical principles behind γ -secretase and other IAP function in order to better tackle the selective inhibition needed to develop a successful therapeutic for Alzheimer and other diseases.

1.5 Thesis objectives

1.5.1 Development of a FRET-based IAP enzyme assay

Chemical details of intramembrane proteolysis remain elusive despite its prevalence throughout biology. Typically, enzyme assay on IPs are discontinuous in which chemical reactions are quenched at specific time intervals and visualized using Western blot or ELISA. Discontinuous assay comes with different disadvantages: 1. data collection and processing takes days; 2. it is impractical to test on a variety of substrates and identify mode of inhibition from several inhibitors at once. Hence, we developed a continuous FRET peptide assay for an intramembrane aspartyl protease (IAP) from *Methanoculleus marisnigri* JRI (MCMJR1) to study enzyme kinetics. Continuous assays give us real time measurement of product formation in a fast, robust and high throughput manner. A former postdoctoral fellow in our lab screened several commercially available hydrophobic FRET peptides and found that the renin 390 FRET substrate was cleaved by our IAP. In collaboration with the Torres lab (School of Biological Sciences), we used a

gel assay in combination with high resolution liquid chromatography (LC)-MS technique to identify the cleavage site of substrate. Catalytic rates and cleavage sites were determined in detergent and bicelles, a bilayer that resembles the lipid membrane. The modes of inhibition by three well-established IAP inhibitors and the role of the first TM helix in catalysis, were directly investigated.

1.5.2 Structure-function and substrate specificity of IAP

Mechanistic and biochemical details of intramembrane proteolysis accomplished by the aspartyl sub-class of intramembrane proteases, which is central to a number of biological processes, remain largely obscure. In this study, we explored how structural mutations of IAP affect its catalytic activity and cleavage profile using our continuous FRET assay coupled to LC-MS analysis (Section 1.5.1). The influence of catalytic motifs YD...GxGD and conserved PAL motif on proteolysis were evaluated. Next, we expanded our study to the C100 substrate of presenilin. *In vitro* kinetic parameters and cleavage sites of IAP toward the fortuitous renin substrate and C100 were compared, revealing a preference for threonine (Thr). Thr-scanning mutagenesis of the renin substrate were used to tease out physicochemical factors influence the IAP substrate specificity. Cumulatively, our study indicates that both chemical and positional preferences exist for IAP cleavage of respective substrate.

1.5.3 Solution structure of IAP using small-angle neutron scattering

(SANS)

Despite their broad biomedical reach, basic structure-function relationships of IAPs remain active areas of research. Characterization of membrane-bound proteins is notoriously challenging due to their inherently hydrophobic character. For IAPs,

oligomerization state in solution is one outstanding question, with previous proposals for monomer, dimer, tetramer, and octamer. We used small angle neutron scattering (SANS) to characterize the solution structure of IAP. A unique feature of SANS is the ability to modulate the solvent composition to mask all but the enzyme of interest. The signal from the IAP can be enhanced by deuteration, and, uniquely, scattering from detergent and buffers were matched by the use of both tail-deuterated detergent and D₂O. Results of our study indicate the our IAP is a compact monomer in solution, not higher ordered states as previously reported in the literature.

2 Chapter 2: Catalytic properties of intramembrane aspartyl protease substrate hydrolysis evaluated using a FRET peptide cleavage assay

2.1 Publication and author contributions

The data presented in Chapter 2 has been published in ACS Chemical Biology with a citation: Naing, S. H., Vukoti, K. M., Drury, J. E., Johnson, J. L., Kalyoncu, S., Hill, S. E., Torres, M. P., and Lieberman, R. L. (2015) Catalytic Properties of Intramembrane Aspartyl Protease Substrate Hydrolysis Evaluated Using a FRET Peptide Cleavage Assay. *ACS chemical biology* **10**, 2166-2174. The molecular cloning, site-directed mutagenesis, membrane protein expression and purification protocol were developed by Swe Htet Naing, Jason Drury, Sibel Kalyoncu and Jennifer Johnson under the guidance of Dr. Raquel Lieberman. The FRET peptide cleavage assay and gel-based assay were developed and performed by Swe Htet Naing. The expression and purification of substrate protein and fluorescence polarization study was carried out by Swe Htet Naing. The mass spectrometric methodology development and analysis were carried out by Krishna Vukoti and Matthew Torres. Shannon Hill performed the circular dichroism experiment for substrate, MRS.

2.2 Introduction

In spite of their biological importance and implications in diseases, relatively few details are known about the biochemistry of IPs. Contrary to intuition and knowledge of soluble proteases (119,120), data to date suggest that the three canonical IP classes do not exhibit a sequence recognition motif within their TM substrate, and, while helix disfavored residues within the TM segment are thought to be important for cleavage

(80,90), examples to the contrary appear in the literature (51,52). Detailed biochemical investigations of intramembrane proteins are notoriously challenging due to the need for lipids or lipid-mimicking detergents, which are largely incompatible with downstream analytical methods such as mass spectrometry (MS) often used to rigorously confirm products. For IPs, high levels of purity are also necessary to remove contamination by low abundance but active cellular proteases. Standard in the IP field is the use of a discontinuous activity assay involving the incubation of enzymes with epitope tagged substrates followed by detection of cleavage products by Western blot, ELISA, or Matrix Assisted Laser Desorption Ionization (MALDI) MS analysis. Such assays have been used extensively to clarify biological processes (reviewed in (121)), optimize purification protocols for the presence of lipid and/or detergent (122,123), and, especially for γ -secretase, develop transition-state and non-transition-state γ -secretase inhibitors with therapeutic potential to selectively treat Alzheimer disease without affecting Notch (124).

A recognized disadvantage of discontinuous assays is that catalytic parameters, substrate preferences, and modes of inhibition are difficult to extract with high degree of certainty, details that would be readily measured using a continuous assay. To the best of our knowledge, continuous assays to date have only been employed in the case of rhomboid, the most biochemically tractable IP. One provocative study proposes that catalysis is governed by the turnover number (k_{cat}) and not substrate affinity, based on measurements with a biological peptide substrate containing a lipid-quenched fluorescein isothiocyanate (FITC) fluorophore (31). However, two other studies, one utilizing fluorescent casein and another involving a fusion protein containing Förster Resonance Energy Transfer (FRET) pairs cyan and yellow fluorescent proteins, present more a

conventional scenario for an enzyme, with measured Michaelis constant (K_m) and maximal velocity (V_{max}) values in the low micromolar and mid nanomolar per minute range, respectively (10,32). The aforementioned studies and a related study on γ -secretase that used intensities from ELISA measurements in the discontinuous assay to extract catalytic parameters(125) converge on slow catalytic rates, but not substrate affinities or effect of detergent/lipid on reaction rates for IPs. Moreover, in the aforementioned studies, cleavage site(s) were not thoroughly investigated. Conversely, in a recent study of the purified and structurally characterized (54) intramembrane aspartyl protease (IAP) from *Methanoculleus marisnigri* JR1 (MCMJR1) in which resulting peptides were identified by MS, kinetics were not investigated (53). These examples motivate the study of IP enzymology to compare biochemical features among IP classes and resolve apparent disparities, as well as demonstrate the need to develop standard continuous assays coupled to high resolution analytical techniques to better comprehend biological intramembrane peptide processing.

Here in Chapter 2, we present and implement a sensitive and rapid FRET peptide cleavage assay (Figure 2.1) to study the kinetic properties of purified MCMJR1 IAP, for which a structure is known but not biological function or substrate(s). The effects of detergent/lipid environment, the role of first N-terminal helix in activity, and mode of inhibition for three IAP- and γ -secretase-specific inhibitors (Figure 2.1), were examined. Results are compared to the typical gel-based discontinuous assay and cleavage sites are identified using quantitative proteomics MS analysis. Taken together, our study offers biochemical details of IAP and their inhibitors; demonstrates previously unappreciated

similarities with soluble aspartyl proteases; and provides new tools to study other IP family members in molecular detail.

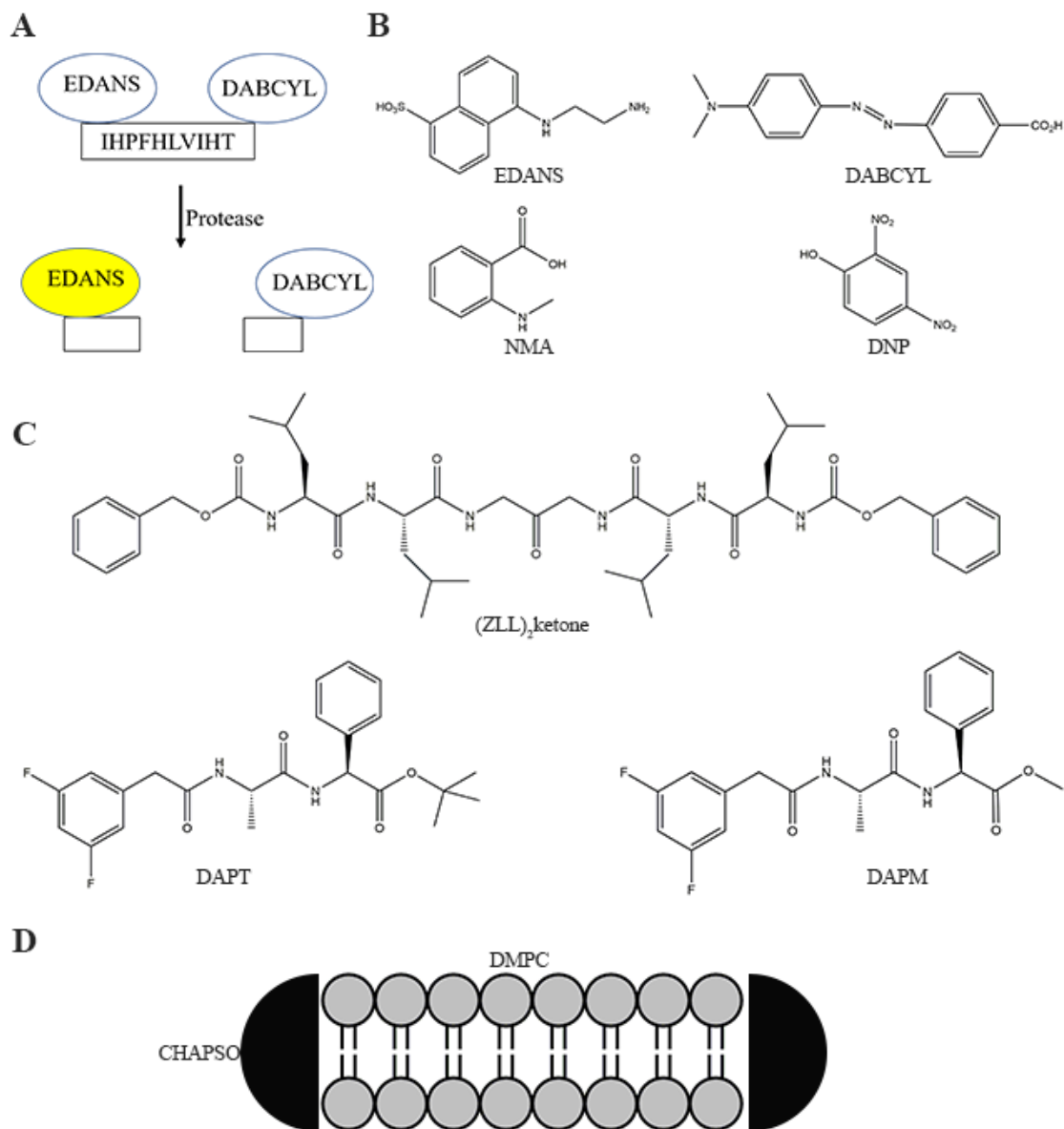


Figure 2.1. Illustration of FRET assay, chemical structures of fluorophores, quenchers, inhibitors and bicelle. (A) Pictorial demonstration of FRET assay. The release of fluorescence from EDANS is seen after cleavage by protease. (B) Chemical structures of fluorophores-quencher pairs (EDANS-DABCYL and NMA-DNP). (C) SPP-specific inhibitor $(ZLL)_2$ ketone and specific inhibitor of γ -secretase, DAPM and DAPT. (D) Bilayer of bicelle is formed by DMPC and the hydrophobic tails at the edge are sealed by CHAPSO

2.3 Methods

2.3.1 Cloning, expression, and purification of MCMJR1 IAP variants

The full length IAP plasmid was generated by restriction free (RF) cloning (126). The target gene sequence was first amplified from genomic DNA of MCMJR1 (ATCC 35101D-5) using specifically designed primers harboring 5' NcoI and 3' SalI restriction sites for ligation into pET-22b(+) vector (Table 2.1) and methods described in the RF cloning website (<http://www.rf-cloning.org>). The demethylated plasmid mixture was transformed into *E. coli* XL-10 Gold (Agilent), single colonies selected for overnight growth in Luria broth (LB media, Fisher) supplemented with 60 µg/mL ampicillin, and plasmid purified using QIAprep Spin Miniprep Kit (Qiagen). The sequence of IAPΔN23 was amplified from genomic DNA using primers listed in Table 2.1 and ligated using traditional cloning procedures into the pET-22b(+) using restriction sites for NcoI and SalI. The two catalytic aspartates Asp 162 and Asp 220 were sequentially mutated to Ala in each IAP plasmid via site-directed mutagenesis (Agilent QuickChange II, Agilent) (Table 2.1). Fidelity of all sequences were confirmed by MWG Operon.

Table 2.1. Primers used for cloning and expression of IAPs.

Primers for RF cloning to generate full length IAP	Sequence - 5' to 3'
Forward primer	CGCTGCCCAGCCGGCGATGGCCATGCAGATACGCGACTGG
Reverse primer	GTGCGGCCGCAAGCTTGTCGACGAAAGGAAGCCACGAAAACG
Primers for cloning of IAPΔN23	
Forward primer	CTAGCGCCATGGGGATGCAGATACGCGACTGGCTGCCTCT
Reverse primer	GTACGTGTCGACGAAAGGAAGCCACGAAAACGAACC
Primers for mutagenesis of D162A	Sequence - 5' to 3'
Forward primer	CTCGCGGTCTACGCCGCCATATCGCTC
Reverse primer	GACCGATATGGCGGCGTAGACCGCGAG
Primers for mutagenesis of D220A	Sequence - 5' to 3'
Forward primer	GTCATGGGTATGGGCGCTCTCATCATGCC
Reverse primer	GGCATGATGAGAGCGCCCATACCCATGAC

For large scale expression of IAPs, plasmids of interest described above were transformed into *E. coli* Rosetta 2 cells (Novagen). Individual colonies were selected and grown overnight in 200 mL cultures of LB media supplemented with 34 μ g/mL chloramphenicol and 60 μ g/mL ampicillin at 37°C. Large cultures (1 L) were inoculated with overnight inoculum and grown in LB media supplemented with 34 μ g/mL chloramphenicol and 60 μ g/mL ampicillin in an orbital shaker (225 rpm, 37°C) until

OD_{600nm} = 0.8-1 was reached. After chilling the cultures to 18°C for ~1.5 hr, protein expression was induced by the addition of 0.5 mM isopropyl-β-D-1-thiogalactopyranoside (IPTG). Cultures were grown overnight and cells were harvested by centrifugation at 5,000 x g, flashed cooled with liquid nitrogen for -80°C storage.

To lyse cells, 8 g of cell paste was suspended in 35 mL of 50 mM Hepes (pH 7.5), 200 mM NaCl containing Complete EDTA-free protease inhibitor cocktail (Roche). The cell suspension was lysed using a French press via 2 passages at 15,000 psi, and then centrifuged at 5,000 x g for 15 min for four times to remove cell debris. The supernatant was decanted and subjected to ultracentrifugation at 162,000 x g for 45 min. The pelleted membrane fraction was resuspended in the same buffer using a Dounce homogenizer, and the membrane fraction collected following repelleting by ultracentrifugation. For purification, ~0.3 g of membranes were first solubilized in 20 mL of 50 mM Hepes (pH 7.5), 500 mM NaCl, 20 mM imidazole and 1% (w/v) DDM (1:10 DDM: cell mass, Anatrace) by gentle rocking for 1.5 hr at 4°C. Unsolubilized material was then isolated by ultracentrifugation at 162,000 x g for 45 min. The supernatant containing solubilized membranes was purified on a 1mL HisTrap FF Crude column (GE Healthcare) connected to an Akta FPLC or Purifier system. Purified enzyme was eluted by a linear gradient generated by mixing buffers containing 50 mM Hepes (pH 7.5), 500 mM NaCl, 20 mM imidazole, 0.1% DDM (buffer A) and 50 mM Hepes (pH 7.5), 500 mM NaCl, 500 mM imidazole, 0.1% DDM (buffer B). Elution fractions were pooled and buffer was exchanged to 20 mM Hepes (pH 7.5), 250 mM NaCl, 0.05% DDM (gel filtration buffer) in a 15 mL Amicon Ultra MWCO 50K concentrator (Millipore). The final sample (500-900 μL) was further fractionated using a HiPrep 16/60 Sephacryl -S300 (GE Healthcare)

equilibrated with gel filtration buffer. Pure enzyme, which elutes from the column at a retention volume of ~60 mL, was exchanged to phosphate-buffered saline (PBS, 10 mM sodium phosphate, pH 7.2, 150 mM NaCl) supplemented with 0.05% DDM (pH 7.2) using the aforementioned concentration device. Protein purity was assessed by denaturing sodium dodecyl sulfate polyacrylamide gel electrophoresis (SDS-PAGE) analysis (12% polyacrylamide) stained with Coomassie (127) (Figure 2.2) and concentration was measured using a NanoDrop spectrophotometer (ThermoScientific) ($\epsilon = 33,920 \text{ M}^{-1} \text{ cm}^{-1}$ for IAP and $\epsilon = 27,300 \text{ M}^{-1} \text{ cm}^{-1}$ for IAP Δ N23 calculated using the ExPASy ProtParam Tool (128) and molecular weights calculated from respective amino acid sequences for a monomer) at 280 nm.

2.3.2 Standard assay and inhibitor studies

The renin 390 FRET (Ren390FRET) substrate (R-E(EDANS)-IHPFHLVIHT-K(DABCYL)-R, Anaspec) (where EDANS stands for 5-[(2-aminoethyl)amino]naphthalene-1-sulfonic acid and DABCYL stands for [4-((4-(dimethylamino)phenyl)azo)benzoic acid] was dissolved in DMSO (500 μM stock concentration). Freshly purified IAP sample (0.5 μM) in 10mM sodium phosphate, pH 7.2, 150 mM NaCl (PBS), 0.05% DDM or reconstituted into bicelles (see below), and Ren390FRET (3-40 μM) in PBS with 0.05 % DDM, were mixed by gentle pipetting in a 96-well black-bottomed non-binding plate (Corning Inc.) and sealed with optical adhesive film (MicroAmp). The fluorescence values were monitored every 2 min over the course of an hour at 37°C in a Synergy 2 plate reader (BioTek, filters $\lambda_{\text{ex}} = 360 \pm 40 \text{ nm}$, $\lambda_{\text{em}} = 485 \pm 20 \text{ nm}$). A blank at each substrate concentration was prepared without IAP enzyme and data analyzed as described below.

The three inhibitors used in this study, 1,3-di-(N-Carboxybenzoyl-L-leucyl-L-leucyl)aminoacetone ((ZLL)₂ketone), N-[(3,5-Difluorophenyl)acetyl]-L-alanyl-2-phenylglycine-1,1-dimethylethyl ester (DAPT) and N-[N-3,5-Difluorophenylacetyl]-L-alanyl-S-phenylglycine methyl ester (DAPM) were obtained from Calbiochem and prepared as 1 mM stock solutions in DMSO. The range of concentration of inhibitors used was 2x-60x molar excess over enzyme. Freshly purified enzyme (0.5 µM) in the buffer listed above containing DDM was first incubated for an hour at 37°C with varying inhibitor concentration, then with Ren390FRET as described for the kinetics assay lacking inhibitors. Negative controls were prepared with all components except enzyme. Data were analyzed as described below.

2.3.3 Data calibration and analysis.

Fluorescence of free EDANS was plotted against concentration using the same settings as for the enzyme assay to convert from arbitrary fluorescence units (Afu) to concentration of hydrolyzed substrate. A correction factor (C) for the inner filter effect was established at each concentration of peptide used in the assay, as given by the following relationship (129)

$$C = \frac{F(EDANS)}{F(EDANS + DABCYL)}$$

where F(EDANS) is the fluorescence reading of free EDANS and F(EDANS+DABCYL) is the fluorescence reading of EDANS in the presence of equimolar amount of DABCYL. For each FRET peptide concentration used in experiments, C was applied to yield the corrected fluorescence value in nM/min.

Data were well fit using the Michaelis-Menten analysis option within GraphPad Prism 5. Initial velocities were determined by the fluorescence reading over first 20 min,

subtracted from blank fluorescence, and then plotted against corresponding substrate concentrations. The Michaelis-Menten equation is $V = V_{\max}[S]/(K_m + [S])$ where V is the initial velocity, V_{\max} is the maximum velocity at infinite substrate concentration, $[S]$ is substrate concentration, and K_m is the substrate concentration required to reach half the maximal velocity. Numerous independent samples of cell paste and purified enzyme were tested for each experiment; data and corresponding statistics presented include at least 20 assay replicates for determination of kinetic parameters and 9 replicates for inhibitor studies. For each inhibitor, the mode of inhibition was determined by evaluating fits of different models, and K_i values were calculated from the competitive inhibition model within GraphPad Prism 5 using the equation

$$V = \frac{V_{\max} [S]}{K_m \left(1 + \frac{[I]}{K_i} \right) + [S]}$$

where K_i is the inhibition constant and $[I]$ is the inhibitor concentration.

2.3.4 Circular dichroism (CD).

CD spectra and melts were conducted using a Jasco J-815 spectropolarimeter equipped with a Neslab RTE 111 circulating water bath and a Jasco PTC-4245/15 temperature control system using a 0.1-cm pathlength cell. Ren390FRET without the fluorophore or quencher (IHPFHLVIHTR, Celtek) was dissolved in PBS with 0.05% DDM (0.2 mM peptide concentration). The spectrum was acquired from 300-195 nm at room temperature with a data pitch of 1 nm and a scan rate of 200 nm min⁻¹. Duplicate samples of purified IAP and IAPΔN23 were prepared at 4 μM in same buffer at peptide concentration and spectra acquired from 300-200 nm at 4°C. The spectra presented are the average of 30 duplicate scans. Data were blank-subtracted and converted to molar

ellipticity $\Theta = (\Theta_{\text{obs}} \times 106)/(\text{pathlength (mm)} \times c \times n)$, where Θ_{obs} is the observed ellipticity (mdeg) at wavelength λ ; c is the protein or peptide concentration (μM); and n is the number of residues. Enzyme thermal melts were performed in a 0.1-cm pathlength cell with 1°C min^{-1} increase in temperature from 4 to 80°C . Ten scans at 200 nm min^{-1} from 300 to 200 nm were averaged at each temperature. Data at 222 nm were blank-subtracted, converted to molar ellipticity, and plotted against temperature in GraphPad Prism 5.

2.3.5 Fluorescence polarization (FP)

Ren390FRET lacking the DABCYL quencher (Anaspec) was dissolved in DMSO at $500 \mu\text{M}$. Different concentrations of IAP double mutant D162A/D220A, ($0.6\text{--}50 \mu\text{M}$ in PBS with 0.05% DDM), were titrated with renin 390 substrate (50 nM in PBS with 0.05% DDM) for one minute and anisotropy readings were taken on an ISS spectrofluorometer ($\lambda_{\text{ex}} = 335 \text{ nm}$; $\lambda_{\text{em}} = 495 \text{ nm}$) for ten iterations at 37°C . The data was analyzed with different models in GraphPad Prism 5 software, of which the best was one-site total, which accounts for a specific binding site as well as a non-specific binding component.

2.3.6 Bicelle preparation and reconstitution of IAP samples

A 25% bicelle stock concentration was prepared as described previously (130). Briefly, dimyristoyl phosphatidylcholine (DMPC) and 3-([3-cholamidopropyl]dimethylammonio)-2-hydroxy-1-propanesulfonate (CHAPSO) were added in molar ratio of 2.8:1 and dissolved in deionized water with 8-12 cycles of (1) heating at 42°C for 10 min, (2) cooling on ice for 10 min, (3) vortexing and (4) freezing at -20°C for 10 min. The cold bicelle stock solution was added to the IAP enzyme sample

to obtain a final enzyme concentration of 0.5 μ M for FRET-based assay and 16 μ M for gel-based assay in 5% bicelle. The cold sample was mixed gently and then incubated on ice for an hour to complete the reconstitution process.

2.3.7 Expression and purification of fusion protein substrate for gel assay

DNA corresponding to fusion substrate MBP-IHPFHLVIHT-SUMO-6xHis cloned in pEX-K vector was purchased from MWG Operon. The plasmid was transformed into E. coli BL21 DE3 (Novagen) cells. A single colony was selected and grown overnight in 200 mL of LB media supplemented with 50 μ g/mL kanamycin. Large scale cultures were grown in LB media containing 50 μ g/mL kanamycin in an orbital shaker (225 rpm, 37°C) to an OD_{600nm} = 0.6-0.8. Protein expression was induced with 0.5 mM IPTG followed by growth for 3 hr at 37°C. Cells were harvested by centrifugation at 5,000 x g, and flashed cooled with liquid nitrogen. For purification, 5 g of cells were first lysed by using a protocol analogous to that of enzymes above, except that the cell debris and membranes were removed in a single step by ultracentrifugation at 162,000 x g for 45 min. The supernatant was loaded onto 1 mL HisTrap FF Crude column (GE Healthcare) and purified as above with buffers A and B, but omitting detergent. The elution fractions were pooled and buffer was exchanged to 10 mM Na_2HPO_4 , 10 mM KH_2PO_4 , 200 mM NaCl, 1 mM EDTA (Buffer A for MBPTrap HP Column purification) by four-fold concentration and dilution in a 15 mL Amicon Ultra MWCO 30K concentrator. The sample was further purified on a 5 mL MBPTrap HP column (GE Healthcare) connected to an AKTA FPLC or Purifier system equilibrated with buffer A. Purified substrate was eluted with buffer A supplemented with 10 mM maltose. Protein

purity (Figure 2.2) and concentration were evaluated as described above (calculated $\epsilon = 67,280 \text{ M}^{-1} \text{ cm}^{-1}$).

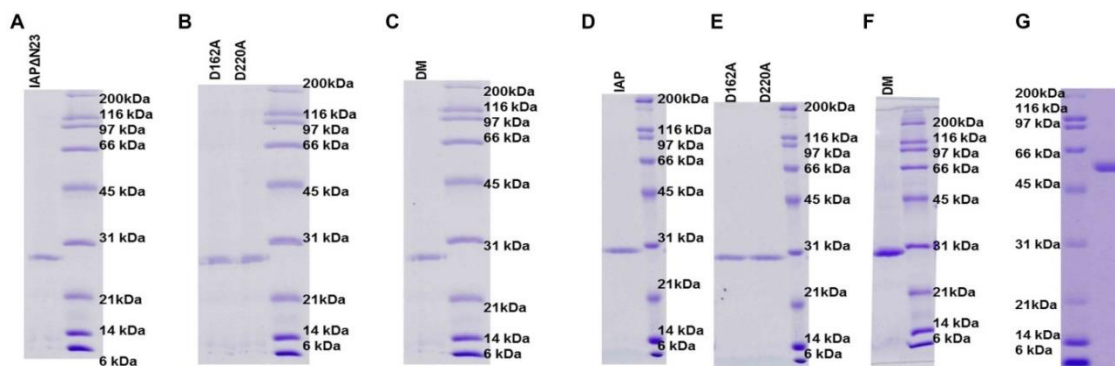


Figure 2.2. Protein purification assessment by SDS-PAGE. (A) IAP Δ N23 (B) single catalytic mutants of IAP Δ N23 D162A, and D220A (C) IAP Δ N23 double mutant (DM) (D162A/D220A) (D) IAP (E) single catalytic mutants of IAP D162A, and D220A (F) IAP DM. (G) MRS (MBP-IHPFHLVIHT-SUMO) substrate used for gel based assay.

2.3.8 Gel-based enzyme assay with fusion substrate

The fusion protein MRS substrate (4 μM) was incubated at 37°C with varying concentrations of freshly prepared enzyme sample in PBS, 0.05 % DDM or 5% bicelles and the reaction was stopped at varying time points by the addition of equal volume of Laemmli sample buffer containing β -mercaptoethanol, followed by storage at -20°C. The effect of enzyme concentration on cleavage was tested by incubating 4 μM fusion substrate with 1 μM - 48 μM of purified IAP or IAP Δ N23 for 24 hrs at 37°C. For time course experiments, 4 μM substrate was incubated with 16 μM enzyme and samples were stopped at intervals between 2 hr – 48 hr.

For inhibitor studies, (ZLL)₂ketone, DAPT and DAPM (32 -320 μM) were added to 16 μM purified IAP or IAP Δ N23 followed by the addition of 4 μM fusion substrate in

PBS, 0.05% DDM. The reaction was incubated at 37°C for 24 hours. Cleavage results were analyzed in two ways. First, 7 μ L of quenched reaction samples were separated by SDS-PAGE (12% polyacrylamide) and visualized by Coomassie staining. Second, 2 μ L of quenched reaction was subjected to SDS-PAGE followed by transfer to polyvinyl difluoride membrane (Biorad) and standard Western blot analysis using anti-MBP mouse monoclonal IgG primary antibody (Santa Cruz Biotechnology, 1:500 dilution), and horse radish peroxidase (HRP)-conjugated goat anti-mouse monoclonal IgG secondary antibody (KPL, 1:5000 dilution). Membranes were sprayed with HyGLO Quick Spray (Denville) and the images developed with autoradiography film.

2.3.9 In-gel protein digestion and LC-MS/MS analysis

For analysis of cleavage sites, in-gel assays were conducted as described above, with the following modifications. At 4, 20, 24, and 48 hr, the reaction was stopped by the addition of ice-cold acetone (6.5 x sample volume) and samples were stored in -20°C until the completion of the experiment. Samples were centrifuged at 8,000 x g at 4°C for 5 min followed by decanting the acetone and air-drying at room temperature for 30 min. Reducing Laemmli sample buffer was added to the precipitated materials which were then boiled in a 95°C bath for 15 min, pooled together and loaded onto a 12 % polyacrylamide gel for SDS-PAGE analysis and Coomassie staining.

In-gel protein digestion was accomplished using a variation of the approach described previously (5). Unless otherwise noted, the various steps of the procedure were performed at room temperature and all incubation steps were performed under shaking (~750 rpm). Protein bands of interest in the Coomassie-stained SDS-PAGE gel were excised, cut into small pieces, transferred into a 1.5 mL microcentrifuge tube and washed

with 100 μ L of deionized water. The supernatant was discarded and 100 μ L of acetonitrile/50 mM ammonium bicarbonate (NH_4HCO_3 ; ABC) (1:1) was added to the gel pieces. This step was performed several times until the gel pieces were completely destained. After removal of the supernatant, the gel pieces were dehydrated with 100% acetonitrile followed by removal of the liquid by speedvac. After the gel pieces were completely dry, the proteins were reduced and alkylated with 10 mM DTT followed by 55 mM iodoacetamide to eliminate disulfide bonding. The gel pieces were again dehydrated with acetonitrile and speedvac followed by rehydration with sequencing-grade Glu-C (Promega) dissolved in 50 mM ABC until completely rehydrated. The excess liquid was removed and replaced with 50-100 μ L of 50 mM ABC and incubated with shaking at 37 °C overnight. Acetonitrile was then added to 50% and shaken for 10 min at room temperature followed by collection of the supernatant into a fresh 1.5 mL microcentrifuge tube. The gel pieces were incubated with 50% acetonitrile again as before and finally with 100% acetonitrile until the gel pieces were completely dehydrated. Supernatant was repeatedly collected in 1.5 mL tube, frozen and concentrated to dryness using a centrivap, and then resuspended in 5% acetonitrile/0.1% formic acid. In-gel digested peptides were analyzed by LC-MS/MS using a Nanoacquity UPLC (Waters) coupled with an LTQ Orbitrap XL mass spectrometer (Thermo) run in data-dependent mode (top-12). Resultant RAW files were analyzed by database matching using Proteome Discoverer (Thermo) and SEQUEST MS data interpretation algorithms trained on the protein of interest. Searching for unique cleavage sites was accomplished by setting the enzyme specificity to 'none', which facilitates a non-biased search for peptides generated through variable cleavage.

2.4 Results and Discussion

2.4.1 Characterization of IAP and N-terminal deletion mutant

IAP Δ N23

IAP and a construct lacking the first 23 amino acids (IAP Δ N23) were designed to examine the functional role of the first TM helix (TM1). This helix was previously believed to be structural (60,131) but the 3.3 Å resolution crystal structure of IAP, a tetramer in an inactive conformation, reveals the location of TM1 in the second shell of helices surrounding the apparent IAP active site, where it is not obviously involved in tetramer stabilization (54) (Figure 2.3A). TM1 abuts catalytic Asp220-containing TM7 approximately at its midpoint. The N-terminus of TM1 and neighboring TM7 and TM8 are rich in Leu and other hydrophobic residues (Figure 2.3A), raising the possibility that low energy alternative TM helical arrangements exist. We postulated that an IAP construct missing half of TM1 (IAP Δ N23) would retain the overall quaternary structure, and insight into the role of TM1 could be gained. Specifically, if TM1 gates substrate access, the deletion construct would exhibit increased activity, a rationale used previously

for rhomboid (29), whereas if TM1 is needed to form a catalytically-competent active site, activity of IAP Δ N23 would decrease.

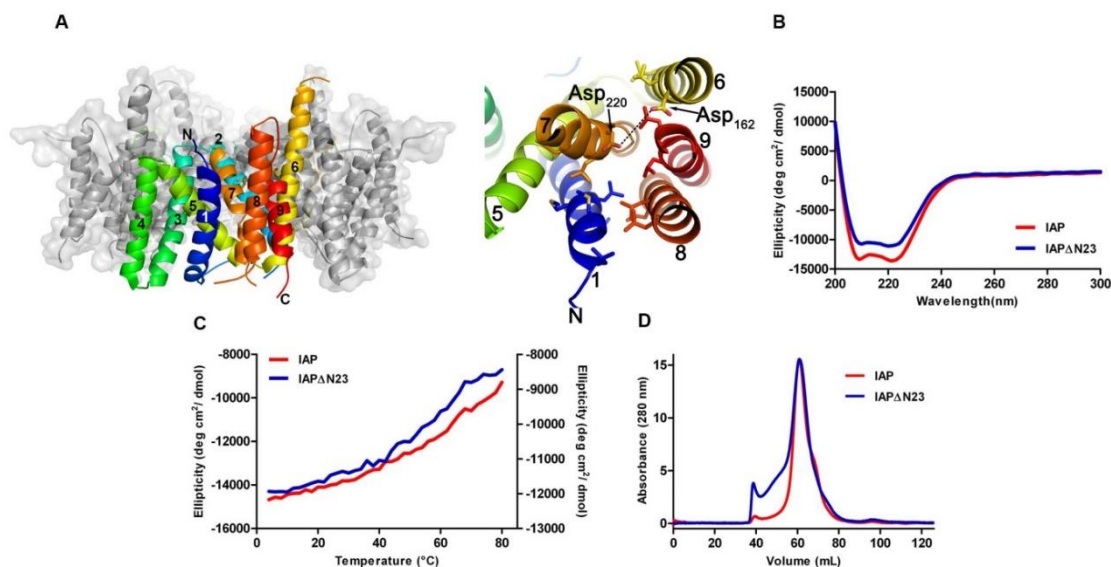


Figure 2.3. Initial characterization of IAP and IAP Δ N23 constructs. (A) Structure of IAP (PDB code 4HYC) showing the nine transmembrane helices of one IAP monomer in the context of the crystallographic tetramer (grey except for red catalytic aspartates) in two orientations (left, center) and top-down zoom into the active site from top face depicting two catalytic aspartate residues and neighboring leucine residues (right). (B) CD spectra acquired at 4°C. (C) CD thermal melts over the range of 4–80°C, monitored at 222 nm. (D) Overlay of size exclusion chromatographs produced from HiPrep 16/60 Sephacryl-S300.

Both full-length IAP and IAP Δ N23 were successfully purified to homogeneity (Figure 2.2). Their characterization by circular dichroism (CD) reveals, as expected, somewhat higher helical content in IAP than IAP Δ N23 (Figure 2.3B). Thermal melts for both proteins are irreversible (not shown), but transitions related to the change in helical content are highly similar (Figure 2.3C). Finally, the main retention peak from size

exclusion chromatography remains unchanged between the IAP variants and IAP Δ N23 (Figure 2.3D).

2.4.2 Development of a FRET-based assay

After testing several commercially available fluorogenic substrates lacking charged residues renin 390 FRET (Ren390FRET) was identified. Ren390FRET contains the angiotensinogen sequence (IHPFHLVIHT) cleaved by the soluble aspartyl protease renin, flanked by EDANS fluorophore and DABCYL quencher. Incubation of freshly purified IAP with Ren390FRET resulted in enzyme concentration-dependent increases in fluorescence over time and thus Ren390FRET was used for the subsequent assay development and implementation. Assay parameters such as buffer, pH, plate type, plate seal, enzyme concentration, detergent identity and concentration, temperature, and duration were optimized for fluorescence signal. Characterization of the substrate lacking FRET pairs dissolved in the n-dodecyl- β -D-maltoside (DDM)-containing buffer used in the assay reveals no obvious secondary structure (Figure 2.4).

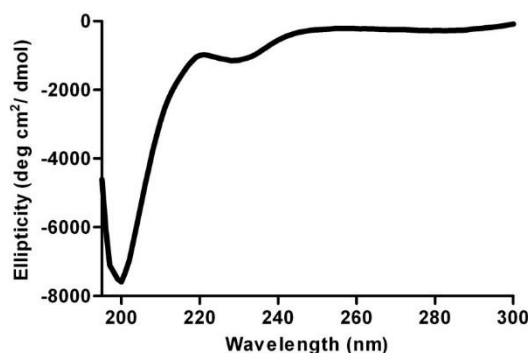


Figure 2.4. Circular dichroism wavelength scan of substrate peptide (IHPFHLVIHTR) in PBS (0.05% DDM).

Pseudo-first order, steady-state reaction conditions were implemented by using at minimum a five-fold molar excess of substrate over enzyme (132). Confirmation of this set up is supported by the similar values measured for the K_m (Table 2.2) and dissociation constant K_d assessed by fluorescence polarization (FP) (Figure 2.5).

Table 2.2. Kinetic parameters of IAP and IAP Δ N23 using Ren390FRET substrate and inhibitors: (ZLL)₂ketone, DAPT and DAPM, performed in DDM unless otherwise noted.

Enzyme	Inhibitor	K_m (μ M)	V_{max} (nM min ⁻¹)	$k_{cat} \times 10^{-3}$ (min ⁻¹)	$(k_{cat} / K_m) \times 10^{-4}$ (μ M ⁻¹ min ⁻¹)
IAP	-	5.2 \pm 0.5	2.25 \pm 0.07	4.6 \pm 0.3	8.8 \pm 1.3
IAP Δ N23	-	8.3 \pm 0.6	1.12 \pm 0.03	2.2 \pm 0.1	2.7 \pm 0.3
IAP ^a	-	5.1 \pm 0.6	2.16 \pm 0.09	4.3 \pm 0.4	8.4 \pm 1.0
IAP Δ N23 ^a	-	8.2 \pm 0.6	1.06 \pm 0.03	2.1 \pm 0.1	2.6 \pm 0.3
IAP	(ZLL) ₂ ketone				
IAP	2x	8.9 \pm 0.6	2.24 \pm 0.06	4.5 \pm 0.2	5.1 \pm 0.6
IAP	5x	11.2 \pm 0.8	2.18 \pm 0.06	4.4 \pm 0.2	3.9 \pm 0.5
IAP	10x	17.7 \pm 2.1	2.20 \pm 0.10	4.4 \pm 0.4	2.5 \pm 0.6
IAP Δ N23	2x	12.6 \pm 0.9	1.11 \pm 0.04	2.2 \pm 0.2	1.7 \pm 0.4
IAP Δ N23	5x	17.3 \pm 1.0	1.11 \pm 0.04	2.2 \pm 0.2	1.3 \pm 0.2
IAP Δ N23	10x	24.5 \pm 2.0	1.11 \pm 0.05	2.2 \pm 0.2	0.9 \pm 0.2
IAP	DAPT				
IAP	20x	6.6 \pm 0.5	2.05 \pm 0.05	4.1 \pm 0.2	6.2 \pm 0.8
IAP	40x	7.7 \pm 0.6	1.97 \pm 0.05	3.9 \pm 0.2	5.1 \pm 0.7
IAP	60x	9.8 \pm 0.9	1.87 \pm 0.07	3.7 \pm 0.3	3.8 \pm 0.7
IAP Δ N23	20x	14.0 \pm 1.0	1.07 \pm 0.04	2.1 \pm 0.2	1.7 \pm 0.3
IAP Δ N23	40x	19.0 \pm 2.0	1.06 \pm 0.06	2.1 \pm 0.2	1.1 \pm 0.3
IAP Δ N23	60x	29.7 \pm 3.0	1.04 \pm 0.07	2.1 \pm 0.3	0.7 \pm 0.9
IAP	DAPM				
IAP	20x	7.5 \pm 0.6	2.13 \pm 0.07	4.3 \pm 0.3	5.7 \pm 1.0
IAP	40x	8.4 \pm 0.7	2.14 \pm 0.07	4.3 \pm 0.3	5.1 \pm 0.9
IAP	60x	11.7 \pm 1.0	2.09 \pm 0.09	4.2 \pm 0.4	3.6 \pm 0.7
IAP Δ N23	20x	10.35 \pm 0.8	1.10 \pm 0.04	2.2 \pm 0.2	2.2 \pm 0.3
IAP Δ N23	40x	15.0 \pm 1.0	1.11 \pm 0.04	2.2 \pm 0.2	1.5 \pm 0.2
IAP Δ N23	60x	19.5 \pm 2.0	1.11 \pm 0.05	2.2 \pm 0.2	1.1 \pm 0.3

^aPerformed in bicelles

Binding of the substrate to the enzyme is best fit by a one-site binding model with K_d of $6.5 \pm 2.0 \mu\text{M}$ (Figure 2.5A). Thus, in our experiment, peptide cleavage events are the subsequent slow steps. Initial velocities were calculated as the slope of the increase in fluorescence over the first 20 min, after which a second slower rate was observed (Figure 2.6). Data were converted to nM min^{-1} using the standard calibration curve for EDANS (Figure 2.7A), and a correction factor for the inner filter effect (Figure 2.7B) was applied. Lastly, DMSO is tolerated up to 4.2% (v/v) in the reaction mixture (Figure 2.7C), the highest concentration used for inhibitor described below.

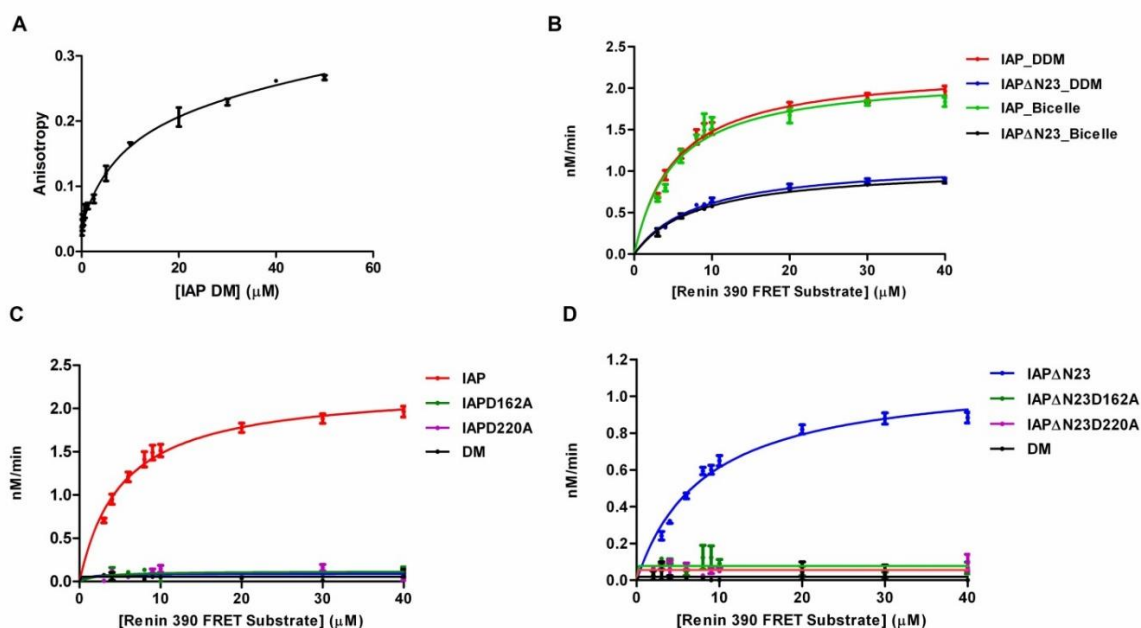


Figure 2.5. Fluorescence polarization and enzymatic analysis for angiotensinogen substrate. (A) Fluorescence polarization using IAP double catalytic mutant D162A/D220A and Ren390FRET substrate lacking DABCYL. (B) Michaelis-Menten kinetics of Ren390FRET cleavage by IAP and IAP Δ N23 in DDM and bicelles. (C), (D) Comparison of catalysis for wild-type IAP and IAP Δ N23 along with single catalytic mutants (D162A or D220A), and double mutants (DM).

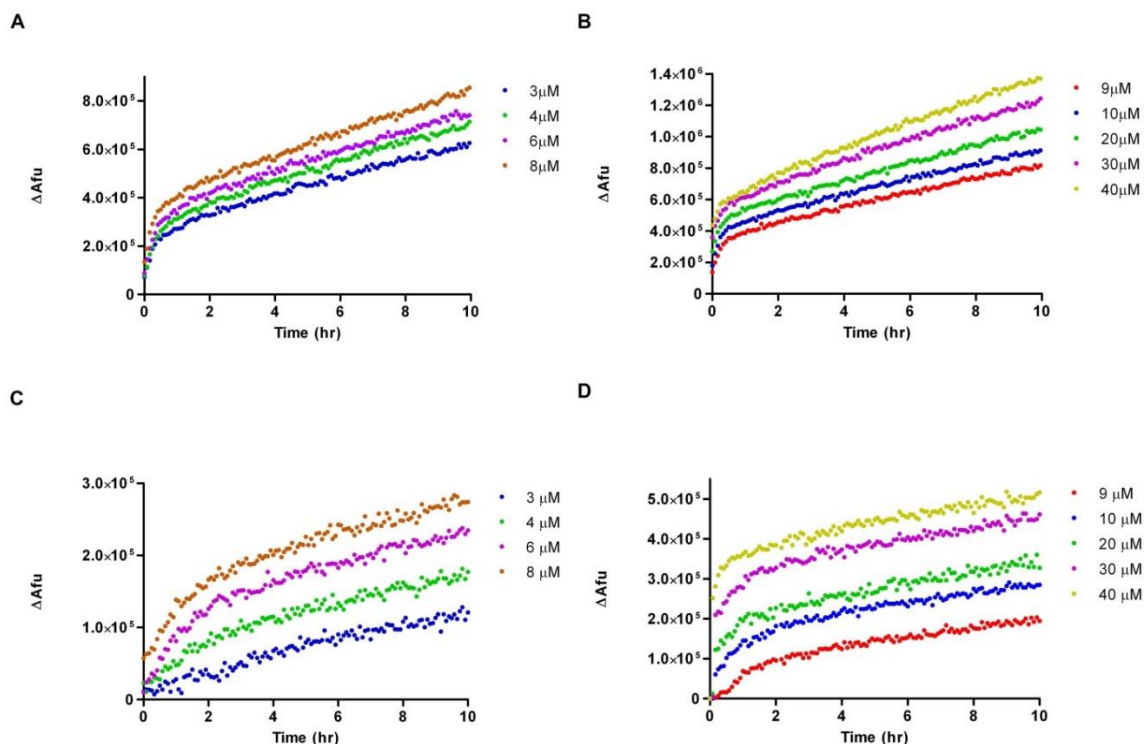


Figure 2.6. Assessment of initial catalytic rates for FRET assay. (A, B) Fluorescence readings for IAP at indicated concentrations over the course of 10 hrs. Initial velocity was found to be within the first 20 min of reaction. (C,D) Corresponding data for IAP Δ N23.

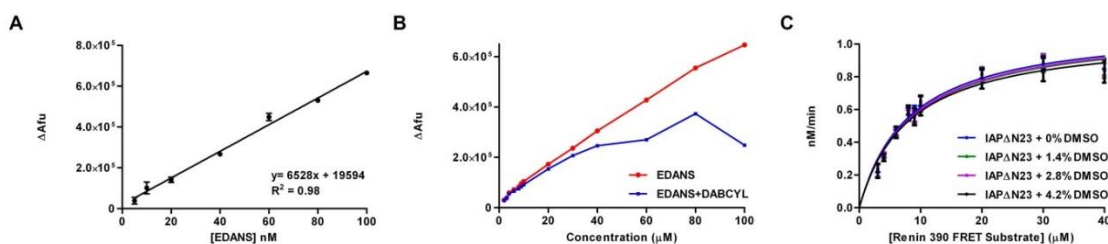


Figure 2.7. Assay calibration. (A) Standard calibration curve of EDANS plotting the arbitrary fluorescence unit (Afu) against concentration of EDANS (nM). The fluorescence reading of free EDANS (5-100 nM) were taken under conditions used for FRET assay. (B) Inner filter effect (IFE) correction (C) Vehicle control test of DMSO on the enzymatic activity of IAP Δ N23.

2.4.3 Kinetic analysis

The reaction set-up in our FRET assay enabled direct determination of Michaelis-Menten kinetics parameters, namely, K_m and k_{cat} , for cleavage of Ren390FRET by IAP and IAP Δ N23 (Figure 2.5B). Catalysis was tested in detergent and after reconstitution into lipid bicelles, which are well-defined lipid bilayer discs with a central plane of phospholipid surrounded by amphiphile (130) that thus mimics the native lipidic milieu. Both enzymes are active, but IAP exhibits two-fold faster kinetics compared to IAP Δ N23, in both in detergent and bicelles (Table 2.2). Alternative analysis of data by the Hill equation yielded poor fits (not shown); there is no evidence of the cooperativity observed in rhomboid (10) for IAP or IAP Δ N23. As estimated by K_m , affinity of Ren390FRET for IAP Δ N23 is about 1.6 fold weaker than for IAP. The requirement for aspartates present in the signature motif YD and GXGD (where X is any amino acid) (133) was confirmed by single catalytic variants of IAP and IAP Δ N23 harboring D162A, D220A, or the double mutant D162A/D220A; none exhibited enzyme activity (Figure 2.5C,D). Thus, results from the FRET assay indicate that while both IAP and IAP Δ N23 are active, require the previously identified aspartates, but kinetics remain unchanged in bicelles and detergent.

The low micromolar K_m measured for the fortuitous Ren390FRET substrate is in the range for that reported for renin (1.8 μ M) (134) and a renin-like fungal aspartic protease (4.3 μ M) (135), as well as for purified, detergent-solubilized γ -secretase with the physiological and widely used C100-flag substrate, which contains a flag-tagged TM substrate and the C-terminal 100 residues of APP (0.28-1 μ M) (125,136). Regarding other IPs, our K_m is in line with reports for purified, detergent-solubilized *E. coli*

rhomboid GlpG using the non-biological and soluble fluorescent substrate casein (0.87 μM) (32), purified *P. stuartii* rhomboid AarA paired with its substrate TatA (7.6 μM) (10), as well as Rce1 with its biological substrate K-ras (0.5 μM) (137); however, our value is notably lower than the $\sim 135 \mu\text{M}$ value measured for rhomboids with a quenched peptide substrate (31). Our k_{cat} values are detectable and similar to that reported recently for partially active γ -secretase with C100-flag ($8 \times 10^{-3} \text{ min}^{-1}$) (125) but slower than purified rhomboid in detergent (0.8 min^{-1} (31), and $0.066\text{-}1.06 \text{ min}^{-1}$, depending on rhomboid ortholog paired with the TatA substrate (10)). Slow catalytic rates measured in our assay may be explained in part by the fact that the angiotensinogen sequence is not the native substrate for our IAP, and likely could be increased if a biological substrate in the host organism MCMJR1 were identified. Nevertheless our results are consistent with the idea that in contrast to well-studied soluble proteases (119,120), proteolysis in the membrane is sluggish.

2.4.4 Mode of inhibition of three small molecules

Numerous inhibitor studies have compared inhibition profiles of γ -secretase and other IAPs (50,138-140), but details of pharmacological differences among compounds are active areas of investigation, typically relying on radio-(136), photoaffinity-(138,141) labeling methods. Here, the inhibitory effects of the SPP-specific inhibitor (ZLL)₂ketone, (50,136), and γ -secretase inhibitors, DAPT (142) and DAPM (143) on IAP and IAP Δ N23 activity were examined in detergent; parallel experiments in bicelles were not possible due to the incompatibility of DMSO required to dissolve inhibitors with the low temperature incubation for IAP bicelle reconstitution. (ZLL)₂ketone was most potent, displaying a reduction of activity with just 2x molar excess over the enzyme

(Figure 2.8A, B). Comparison of different inhibition models favors competitive inhibition for both IAP and IAP Δ N23, consistent with the apparent increase in K_m and unchanged V_{max} with the increase in compound concentration (Table 2.2). The calculated K_i for (ZLL)₂ketone toward IAP is $1.9 \pm 0.2 \mu\text{M}$. DAPT and DAPM are weaker inhibitors of IAP and IAP Δ N23, as they require significantly higher concentrations to reduce enzyme activity (Figure 2.8C–F). Like (ZLL)₂ketone, DAPT appears to be a weak competitive inhibitor of IAP, and inhibition is even less efficient toward IAP Δ N23 (Table 2.2). DAPM is a very weak competitive inhibitor, increasing the apparent K_m of both enzyme versions by just 2.3-fold even at the concentration of 60x, without appreciably altering V_{max} . The corresponding K_i values for DAPT and DAPM for IAP are 16.9 ± 1.7 and $20.5 \pm 2.2 \mu\text{M}$, respectively.

Although comparison of the substrate- and enzyme-concentration independent inhibitor constant (K_i) values for (ZLL)₂ketone, DAPT, and DAPM from our continuous assay are not directly comparable to reported half-inhibitory concentration (IC_{50}) values for different inhibitors toward SPP or γ -secretase, analysis of their modes and potency of inhibition is revealing. Early in vitro studies of SPP presumed that (ZLL)₂ketone is an active site directed and a transition-state analog inhibitor (136) even though weakly electrophilic ketones are not used as inhibitors of soluble aspartyl proteases (144). Our assay demonstrates that (ZLL)₂ketone is indeed a competitive inhibitor of IAP acting on Ren390FRET, but with a modest K_i . This result points to possible different mechanistic details between soluble and intramembrane classes of aspartyl proteases, perhaps due to the dearth of available water within the membrane. Conversely, for the two γ -secretase inhibitors, competitive inhibition ~10-fold weaker than (ZLL)₂ketone was measured. To

date, multiple studies have been unable to measure appreciable inhibition of SPP by the γ -secretase inhibitor DAPT (50,145,146), which has been characterized as a non-transition state analog that binds to an allosteric site on the C-terminal fragment of presenilin, with possible partial overlap with the active site (138,142). We anticipate that structure-activity-relationship inhibitor studies will be readily extended using our multiplexed continuous assay, or variations thereof using different substrates, to generate scaffolds with improved potency and selectivity for IAPs.

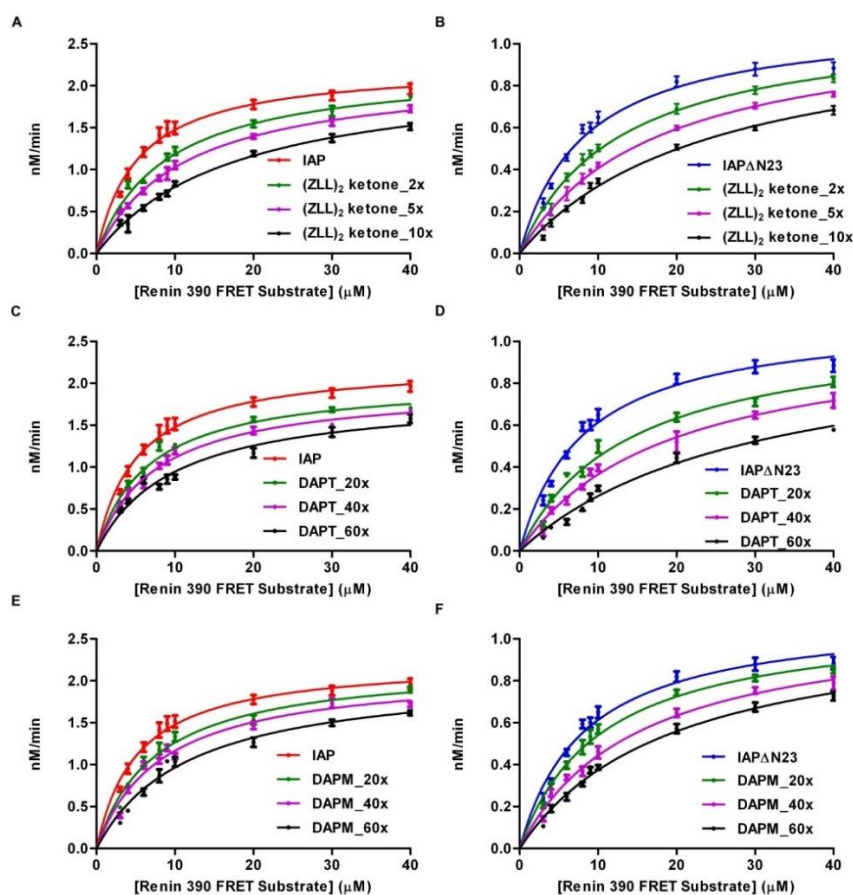


Figure 2.8 . Inhibitor studies to determine mode of inhibition using Ren390FRET substrate. Kinetic data for (A) IAP treated with increasing (ZLL)₂ketone, (B) IAPΔN23 treated with increasing (ZLL)₂ketone, (C) IAP treated with increasing DAPT, (D) IAPΔN23 treated with increasing DAPT, (E) IAP treated with increasing DAPM, and IAPΔN23 treated with increasing DAPM.

2.4.5 Gel-based assay.

To independently verify cleavage and enable clear identification of cleavage site by MS, a discontinuous, gel-based proteolytic assay was employed. A fusion protein containing the angiotensinogen sequence flanked by an N-terminal maltose binding protein (MBP) and a C-terminal small ubiquitin-like modifier (SUMO) (MRS substrate) was designed to readily differentiate uncleaved substrate (~60 kDa) and the N- and C-terminal products (~45 kDa and ~15 kDa). Western blot analysis clearly shows an increase in N-terminal product formation over the course of the reaction (2 h – 48 h) for IAP and IAP Δ N23 in detergent and bicelles (Figure 2.9A, B), in an enzyme concentration-dependent manner (Figure 2.9C). Samples prepared without enzyme confirm that the substrate is not degraded over the course of the experiment. Similarly, catalytic aspartate-inactivated mutants do not form any cleavage products (Figure 2.9D, E). Reduced product formation was observed after incubation of either enzyme with 2x molar excess of (ZLL)₂ketone and 10x of DAPT or DAPM (Figure 2.9F), and product formation was completely abrogated with 5x excess (ZLL)₂ketone and 20x excess DAPT and DAPM over enzyme (Figure 2.9F).

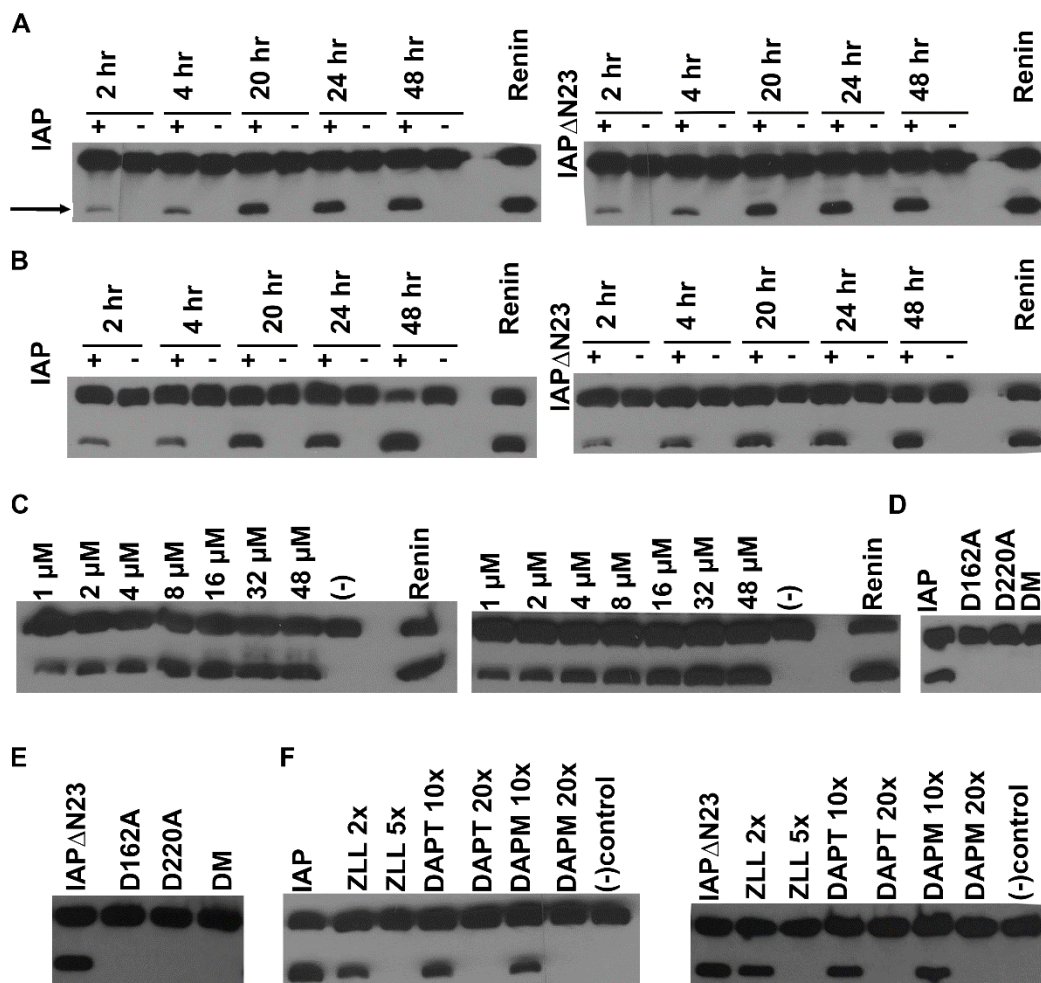


Figure 2.9. Gel cleavage assay using fusion protein substrate MBP-IHPFHLVIHT-SUMO. (A) Time course in detergent. (B) Time course in bicelles. (C) Product formation as a function of enzyme concentration in detergent. (D,E) Activity of catalytic mutants, D162A, D220A and double mutant (DM) D162A/D220A. (F) Inhibition by (ZLL)₂ketone, DAPT and DAPM. Negative control without enzyme (indicated by (-)) and positive control with renin are included. The uncut substrate and cleavage product (indicated by arrow in panel A) were detected by Western blot (see text).

2.4.6 MS analysis.

Although not all available TM sequences are expected to be substrates for IPs due to the need for tight regulation in the cell, cleavage of non-physiological substrates have been repeatedly demonstrated for S2P (90), IAPs (51-53), and rhomboid (10,31,32), and

there is a lengthy list of biological substrates documented for γ -secretase (147). Thus, even though signal sequences can be predicted by bioinformatics to ever-increasing degrees of certainty (148), details of recognition elements within IP substrates, particularly of the IAP class, remain obscure. Direct detection of cleavage products from our FRET assay proved unsuccessful likely due to the presence of a multitude of MS incompatible components within the reaction mixture. Thus, to determine cleavage-site specificity of IAP and IAP Δ N23, we analyzed the 45 kDa MBP product from the gel-based assay by in-gel digestion and LC-MS/MS. As a design feature of the MRS substrate, digestion with Glu-C protease produces a reporter peptide containing a single lysine residue, near the C-terminus of MBP but outside the angiotensinogen sequence, to enhance positive ionization of the peptide by nano-electrospray (Figure 2.10A). The average coverage of the MBP product band by LC-MS was between 87% – 93% and included the extreme N- and C-termini (across all experiments). Cleavage sites within the angiotensinogen sequence were detected by liquid chromatography (LC)-MS/MS of a product mixture after Glu-C digestion. Renin was used as a positive control to validate the cleavage assay with the MRS substrate. LC-MS/MS analysis of the resulting MR product correctly revealed L-V as the preferred cleavage site (149) (Figure 2.10B).

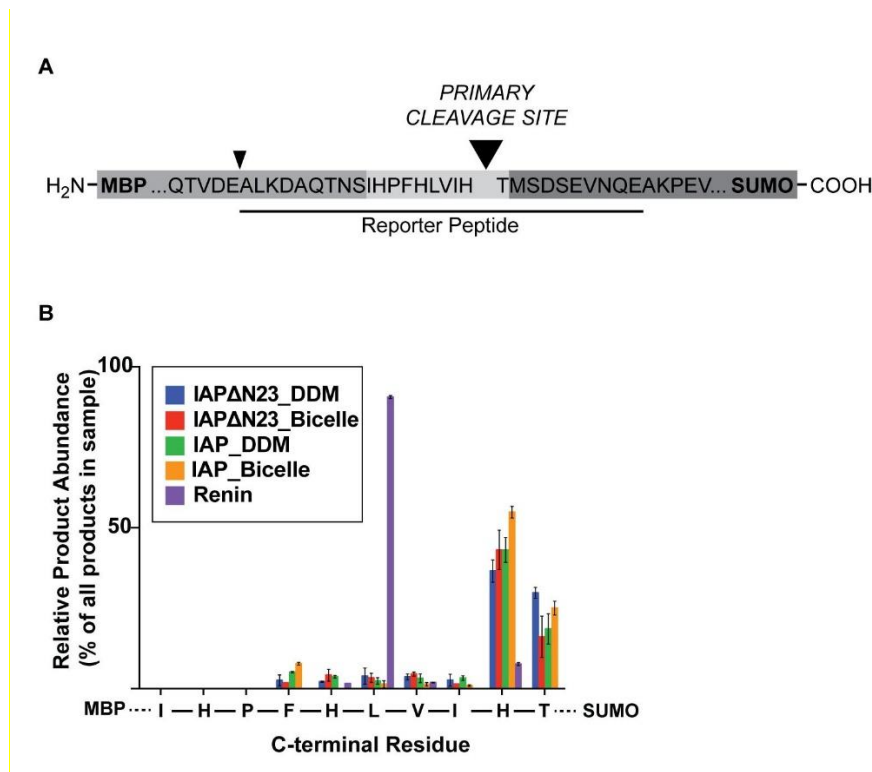


Figure 2.10. Mass spectrometric analysis of cleavage sites. (A) IAP and IAPΔN23 primary cleavage site identified in this study. Peptides were generated by Glu-C digestion of the N-terminal product, facilitated by a C-terminal Glu within MBP (smaller triangle). (B) Peptide spectral matches (PSMs) of the reporter peptide relative to the PSMs for 5 independent peptides from the N-terminal product after proteolytic cleavage in each condition. Bars represent the proportion of each cleavage reporter peptide (indicated by its C-terminal residue) relative to total PSMs across all detected version of the reporter peptide in each sample. Error bars represent the standard deviation among 3 LC-MS analyses from each sample. See also Figure 2.11, Figure 2.12 and Table 2.3

Cleavage profiles of IAP and IAPΔN23 in both bicelles and detergent were examined next. To broadly survey cleavage with time and detect processivity, if present, each conditional reaction was stopped at four intervals (4, 20, 24, 48 hrs) and then combined into a single analysis. Thus, each MBP band contains a population of products resulting from cleavage at four different time points. In total, 24 independent LC-MS analyses were conducted across two biological replicates and each enzyme/detergent

combination. Three major observations were made based on the resulting data after quantitation of peptide spectral matches(Figure 2.10, Figure 2.11, Figure 2.12). First, cleavage by either IAP or IAP Δ N23 was restricted to the reporter peptide and no other peptides were found that did not correspond to Glu-C peptides, confirming that, as expected, both IAP and IAP Δ N23 cleavage were specific to the sequence between MBP and SUMO. Second, IAP and IAP Δ N23 exhibited preferential cleavage between His and Thr within the renin substrate sequence and distinct from the renin cleavage site. To the best of our knowledge, the cleavage site His-Thr has only been reported once, for a secreted aspartic protease from *C. albicans*, coincidentally using the same angiotensinogen substrate (135). Cleavage was also found between T and M (the N-terminal residue of SUMO) at approximately 50% abundance compared to H-T cleavage (Figure 2.10). Third, there was no significant difference observed in the cleavage site preference of IAP and IAP Δ N23 in either bicelles or detergent, although the relative abundance of the H-T cleavage product was two times greater in bicelles versus detergent, suggesting that the reaction is more selective in bicelles (Table 2.3).

Given the fact that the angiotensinogen sequence, while hydrophobic, is not a biological TM helix, nor does it exhibit obvious helical structure in solution (Figure 2.4), and in light of the promiscuity mentioned above for IAPs, additional sites were anticipated. Only one other cleavage position, T-M, not present in Ren390FRET, was detected at appreciable levels. This site is similar to T-L reported as a primary cleavage position for IAP using a MBP-C100-His fusion protein (53); notably, we do not observe significant cleavage at L-V or V-I also reported in the same study. Thus, our findings raise new peculiarities regarding substrate recognition for IAPs and will enable systematic

investigations of sequence preferences at and beyond the scissile bond, as well as the extent of positional preferences or processivity, which are important aspects of γ -secretase biology because such action leads to peptides of varying pathogenicity (150) but has only been explored to a limited extent in other IAPs (51,53).

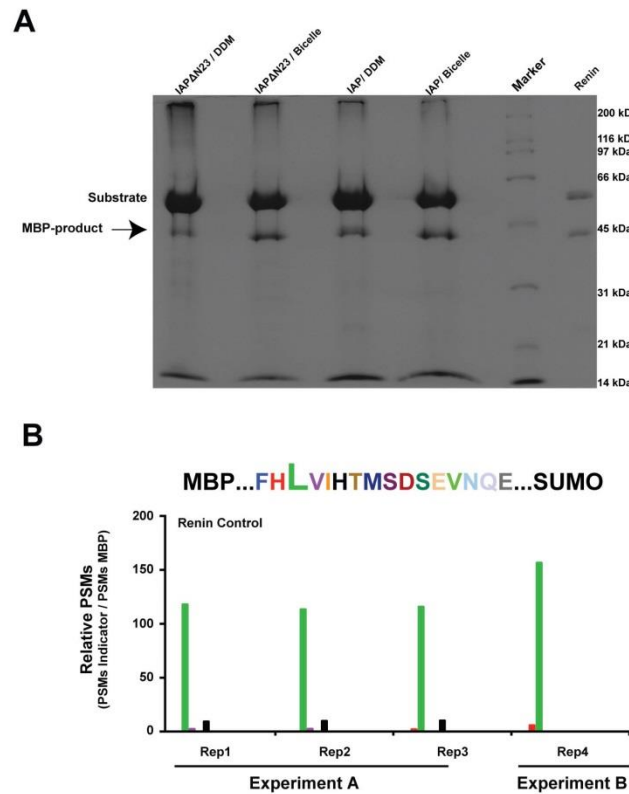


Figure 2.11. Mass spectrometric analysis (A) Representative SDS-PAGE analysis of N-terminal product (MBP product, indicated by an arrow) produced by IAP and IAP Δ N23 in DDM and bicelle conditions. Positive control was prepared with renin and MRS. (B) Relative PSMs of cleavage products by renin from two biological replicates indicated as experiment A and B. The LC-MS/MS analysis was carried out in 4 replicates (Rep1-4).

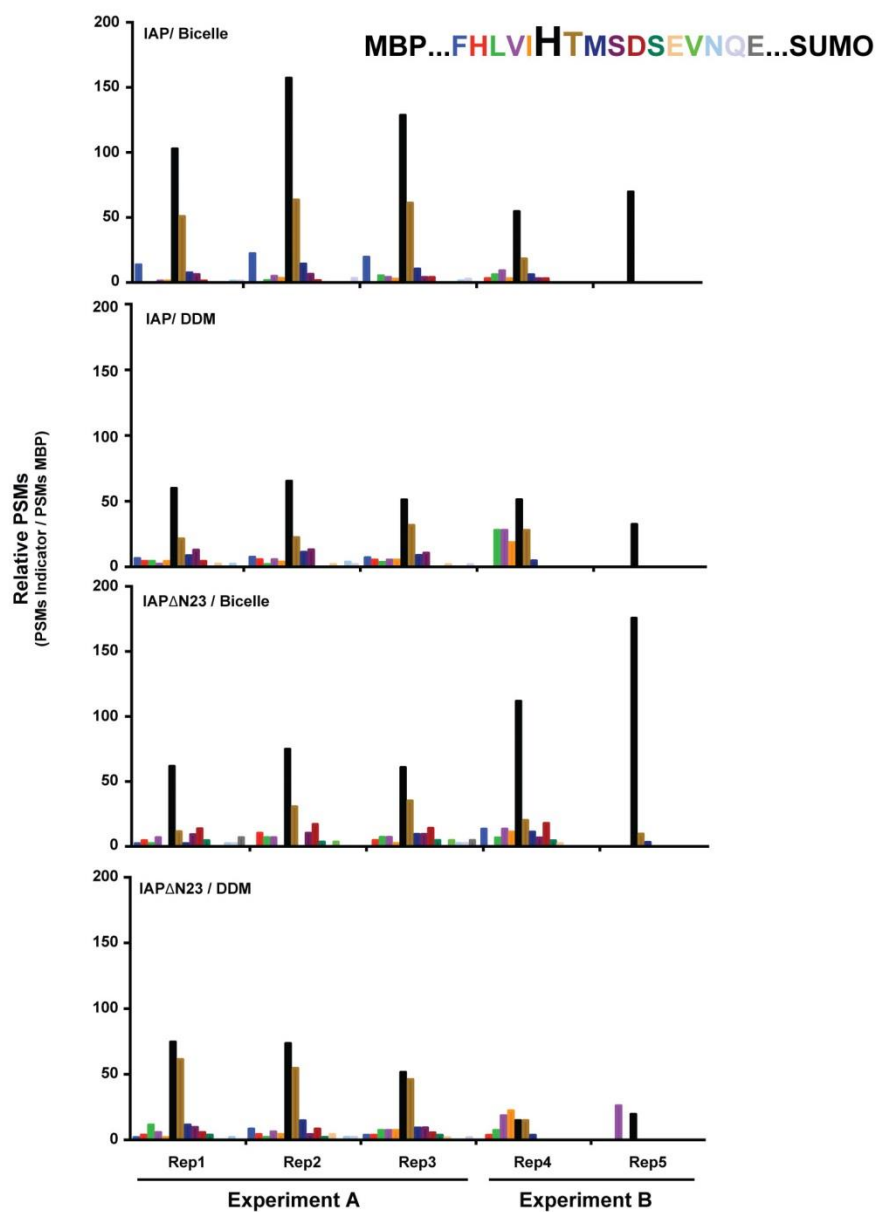


Figure 2.12. Relative PSMs of cleavage products formed by IAP and IAP Δ N23 from two biological replicate indicated as experiment A and B. The LC-MS/MS analysis was carried out in 4 replicates (Rep1-4).

Table 2.3. MRS cleavage reporter and control peptides observed by LC-MS/MS.

MRS Reporter and MBP Control Peptides Observed				IAPΔN23 / DDM						IAPΔN23 / Bicelle					
Peptide #	Sequence	MH+ [Da]	# INDEPENDENT LC-MS/MS OBS	Ave PSMs	PSM STDev	Charge	Ave Xcorr	SDev Xcorr	Ave ΔM	Ave PSMs	PSM STDev	Charge	Ave Xcorr	SDev Xcorr	Ave ΔM
Peptide-1	ALKDAQTNSHPFF	1441.741	11	2.33	1.53	3	3.33	0.32	-0.00207	3.50	3.54	3	2.48	0.52	-0.0074
Peptide-2	ALKDAQTNSHPFH	1578.801	13	1.75	0.50	3	4.24	0.24	-0.00095	2.33	0.58	3	4.68	0.13	-0.00217
Peptide-3	ALKDAQTNSHPFHL	1691.884	19	3.25	2.22	3	4.90	0.39	-0.00022	2.25	0.96	3	4.27	1.32	0.000293
Peptide-4	ALKDAQTNSHPFHLV	1790.953	19	3.80	0.84	3	4.16	0.71	-0.00052	3.50	1.73	3	4.53	0.32	0.000663
Peptide-5	ALKDAQTNSHPFHLVH	1904.038	14	3.25	2.22	4	3.23	0.31	-0.00049	3.00	2.83	3 & 4	3.39	0.20	6.71E-05
Peptide-6	ALKDAQTNSHPFHLVH	2041.095	23	21.80	17.17	4	4.38	0.96	0.000202	36.00	15.28	4	5.12	0.33	0.000436
Peptide-7	ALKDAQTNSHPFHLVHT	2142.146	17	21.75	12.23	4	4.89	0.61	0.000557	8.20	4.60	4	4.51	1.06	0.001328
Peptide-8	ALKDAQTNSHPFHLVHTM	2273.183	16	4.75	2.63	4	5.07	1.45	-0.00051	2.75	2.06	4	3.97	1.45	-0.00033
Peptide-9	ALKDAQTNSHPFHLVHTMS	2360.215	14	4.00	1.73	4	4.76	0.96	-0.00241	3.50	0.58	4	3.71	0.45	-0.00077
Peptide-10	ALKDAQTNSHPFHLVHTMSD	2475.243	12	3.33	0.58	4	4.69	0.28	-0.00169	6.25	1.26	4	5.45	0.44	-0.00041
Peptide-11	ALKDAQTNSHPFHLVHTMSDS	2562.273	7	1.67	0.58	4	3.48	0.91	-0.00215	1.75	0.50	4	4.37	0.26	-0.0026
Peptide-12	ALKDAQTNSHPFHLVHTMSDSE	2691.319	5	1.50	0.71	4	3.65	0.36	9.16E-05						
Peptide-13	ALKDAQTNSHPFHLVHTMSDSEV	2790.388	2							1.50	0.71	4	3.17	0.28	-0.00107
Peptide-14	ALKDAQTNSHPFHLVHTMSDSEVNQ	3032.483	9	1.00	0.00	4	3.38	0.56	-0.00687	1.00	0.00	4	2.67	0.45	-0.00154
Peptide-15	ALKDAQTNSHPFHLVHTMSDSEVNGE	3161.531	9	1.00	0.00	4	2.63	0.05	-0.0004	1.00	0.00	5	2.54	0.04	-0.00112
Peptide-16	ALKDAQTNSHPFHLVHTMSDSEVNGEAKPE	3586.755	2							2.50	0.71	4 & 5	2.79	0.73	-0.00219
MBP -1	AVNKDKPGALVAKSYEE	2061.088	24	61.00	18.01	3	5.70	0.64	0.000807	62.80	13.14	3	5.83	0.35	-0.00069
MBP -2	KDTGKVTVEHPKLE	1938.016	23	53.40	23.82	3	5.05	0.30	0.000599	43.25	5.56	3	4.76	0.86	-0.00092
MBP -3	NYLTDEGLE	1166.558	24	31.80	19.01	2	3.17	0.46	0.000674	32.60	3.58	2	2.96	0.24	0.000112
MBP -4	LVDKPRIATME	1343.736	19	23.75	12.23	2	2.84	0.23	0.002121	18.75	4.65	2	2.62	0.43	-0.00083
MBP -5	LAKFLE	849.475	22	14.60	6.66	2	2.10	0.20	0.00017	11.75	6.18	2	2.24	0.16	-0.00017
MBP Ave				36.91						33.83					
Sumo Avg				2.30						1.10					
				Relative to MBP Control Peptides						Relative to MBP Control Peptides					
Peptide #	Sequence	MH+ [Da]		Ave PSMs	PSM /MBP	Relative	Δ-SUMO/SUMO			Ave PSMs	PSM /MBP	Relative	Δ-SUMO/SUMO		
Peptide-1	ALKDAQTNSHPFF	1441.741		2.33	6.32		0.01			3.50	10.35		2.18		
Peptide-2	ALKDAQTNSHPFH	1578.801		1.75	4.74		-0.24			2.33	6.90		1.12		
Peptide-3	ALKDAQTNSHPFHL	1691.884		3.25	8.81	0.1	0.41			2.25	6.65	0.0	1.05		
Peptide-4	ALKDAQTNSHPFHLV	1790.953		3.80	10.30		0.65			3.50	10.35		2.18		
Peptide-5	ALKDAQTNSHPFHLVH	1904.038		3.25	8.81		0.41			3.00	8.87		1.73		
Peptide-6	ALKDAQTNSHPFHLVH	2041.095		21.80	59.06	0.4	8.48			36.00	106.41	0.8	31.73		
Peptide-7	ALKDAQTNSHPFHLVHT	2142.146		21.75	58.93	0.8	8.46			8.20	24.24	0.3	6.45		
Peptide-8	ALKDAQTNSHPFHLVHTM	2273.183		4.75	12.87		1.07			2.75	8.13		1.50		
Peptide-9	ALKDAQTNSHPFHLVHTMS	2360.215		4.00	10.84		0.74			3.50	10.35		2.18		
Peptide-10	ALKDAQTNSHPFHLVHTMSD	2475.243		3.33	9.03		0.45			6.25	18.47		4.68		
Peptide-11	ALKDAQTNSHPFHLVHTMSDS	2562.273		1.67	4.52		-0.28			1.75	5.17		0.59		
Peptide-12	ALKDAQTNSHPFHLVHTMSDSE	2691.319		1.50	4.06		-0.35								
Peptide-13	ALKDAQTNSHPFHLVHTMSDSEV	2790.388								1.50	4.43		0.36		
Peptide-14	ALKDAQTNSHPFHLVHTMSDSEVNQ	3032.483		1.00	2.71		-0.57			1.00	2.96		-0.09		
Peptide-15	ALKDAQTNSHPFHLVHTMSDSEVNGE	3161.531		1.00	2.71		-0.57			1.00	2.96		-0.09		
Peptide-16	ALKDAQTNSHPFHLVHTMSDSEVNGEAKPE	3586.755								2.50	7.39				

MRS Reporter and MBP Control Peptides Observed				IAP / DDM						IAP / Bicelle					
Peptide #	Sequence	MH+ [Da]	# INDEPENDENT LC-MS/MS OBS	Ave PSMs	PSM STDev	Charge	Ave Xcorr	SDev Xcorr	Ave ΔM	Ave PSMs	PSM STDev	Charge	Ave Xcorr	SDev Xcorr	Ave ΔM
Peptide-1	ALKDAQTNSHPFF	1441.741	11	3.67	0.58	2	3.56	0.24	-0.00147	13.33	2.08	2	3.95	0.31	-0.00116
Peptide-2	ALKDAQTNSHPFH	1578.801	13	2.67	0.58	3	4.41	0.40	-0.00241	1.00	0.00	3	3.58	0.00	0.004914
Peptide-3	ALKDAQTNSHPFHL	1691.884	19	2.75	2.22	3	4.23	1.06	-0.00107	2.33	1.53	3	4.28	1.19	-0.00234
Peptide-4	ALKDAQTNSHPFHLV	1790.953	19	3.25	2.06	3	4.54	0.25	-0.0014	2.50	1.00	3	5.12	0.38	2.21E-05
Peptide-5	ALKDAQTNSHPFHLVH	1904.038	14	2.75	0.96	4	3.12	0.13	-0.00186	1.50	0.58	4	3.14	0.37	-0.00126
Peptide-6	ALKDAQTNSHPFHLVH	2041.095	23	21.40	13.20	4	4.73	0.61	-0.00031	62.40	43.35	4	4.94	0.58	8.52E-05
Peptide-7	ALKDAQTNSHPFHLVHT	2142.146	17	11.50	5.00	4	4.58	0.83	-0.00261	33.50	18.59	4	5.24	0.82	0.000251
Peptide-8	ALKDAQTNSHPFHLVHTM	2273.183	16	4.00	2.16	4	5.07	1.40	-0.00272	6.25	3.10	4	5.16	1.19	0.001316
Peptide-9	ALKDAQTNSHPFHLVHTMS	2360.215	14	6.33	0.58	4	4.60	0.25	-0.0016	3.25	1.71	4	3.83	0.56	0.001438
Peptide-10	ALKDAQTNSHPFHLVHTMSD	2475.243	12	2.00	0.00	4	4.85	0.00	-0.00121	1.50	1.00	4	4.53	1.00	0.000991
Peptide-11	ALKDAQTNSHPFHLVHTMSDS	2562.273	7												
Peptide-12	ALKDAQTNSHPFHLVHTMSDSE	2691.319	5	1.00	0.00	4	3.57	0.40	-0.00032						
Peptide-13	ALKDAQTNSHPFHLVHTMSDSEV	2790.388	2												
Peptide-14	ALKDAQTNSHPFHLVHTMSDSEVNQ	3032.483	9	1.50	0.71	4	2.67	0.31	-0.00187	1.00	0.00	4	2.88	0.41	-0.0037
Peptide-15	ALKDAQTNSHPFHLVHTMSDSEVNGE	3161.531	9	1.00	0.00	4	2.90	0.13	-0.00345	1.67	0.58	4	3.10	0.26	-0.00189
Peptide-16	ALKDAQTNSHPFHLVHTMSDSEVNGEAKPE	3586.755	2												
MBP -1	AVNKDKPGALVAKSYEE	2061.088	24	58.40	24.79	3	5.83	0.64	-0.00139	79.60	37.37	3	6.02	0.48	-3.6E-05
MBP -2	KDTGKVTVEHPKLE	1938.016	23	43.00	34.52	3	4.33	1.36	-0.00104	79.20	56.90	3	4.75	0.85	0.000635
MBP -3	NYLTDEGLE	1166.558	24	32.80	18.98	2	2.97	0.56	-0.00025	28.00	7.00	2	3.00	0.29	0.000103
MBP -4	LVDKPRIATME	1343.736	19	32.67	4.16	2	2.62	0.63	0.0009	31.75	17.29	2	2.88	0.13	0.003487
MBP -5	LAKFLE	849.475	22	17.00	8.60	2	2.16	0.27	-0.00015	17.20	6.02	2	2.30	0.13	-0.00016
MBP Ave				36.77333333						47.15					
Sumo Avg				1.10						2.10					
				Relative to MBP Control Peptides						Relative to MBP Control Peptides					
Peptide #	Sequence	MH+ [Da]		Ave PSMs	PSM /MBP	Relative	Δ-SUMO/SUMO			Ave PSMs	PSM /MBP	Relative	Δ-SUMO/SUMO		
Peptide-1	ALKDAQTNSHPFF	1441.741		3.67	9.97		2.33			13.33	28.28		5.35		
Peptide-2	ALKDAQTNSHPFH	1578.801		2.67	7.25		1.42			1.00	2.12		-0.52		
Peptide-3	ALKDAQTNSHPFHL	1691.884		2.75	7.48	0.1	1.50			2.33	4.95	0.0	0.11		
Peptide-4	ALKDAQTNSHPFHLV	1790.953		3.25	8.84		1.95			2.50	5.30		0.19		
Peptide-5	ALKDAQTNSHPFHLVH	1904.038		2.75	7.48		1.50			1.50	3.18		-0.29		
Peptide-6	ALKDAQTNSHPFHLVH	2041.095		21.40	58.19	0.4	18.45			62.40	132.34	1.0	28.71		
Peptide-7	ALKDAQTNSHPFHLVHT	2142.146		11.50	31.27	0.4	9.45			33.50	71.05	1.0	14.95		
Peptide-8	ALKDAQTNSHPFHLVHTM	2273.183		4.00	10.88		2.64			6.25	13.26		1.98		
Peptide-9	ALKDAQTNSHPFHLVHTMS	2360.215		6.33	17.22		4.76			3.25	6.89		0.55		
Peptide-10	ALKDAQTNSHPFHLVHTMSD	2475.243		2.00	5.44		0.82			1.50	3.18		-0.29		
Peptide-11	ALKDAQTNSHPFHLVHTMSDS	2562.273													
Peptide-12	ALKDAQTNSHPFHLVHTMSDSE	2691.319		1.00	2.72		-0.09								
Peptide-13	ALKDAQTNSHPFHLVHTMSDSEV	2790.388			0.00										
Peptide-14	ALKDAQTNSHPFHLVHTMSDSEVNQ	3032.483		1.50	4.08		0.36			1.00	2.12		-0.52		
Peptide-15	ALKDAQTNSHPFHLVHTMSDSEVNGE	3161.531		1.00	2.72		-0.09			1.67	3.53		-0.21		
Peptide-16	ALKDAQTNSHPFHLVHTMSDSEVNGEAKPE	3586.755													

Table 2.3. (continued)

MRS Reporter and MBP Control Peptides Observed				Renin Control					
Peptide #	Sequence	MH+ [Da]	# INDEPENDENT LC-MS/MS OBS	Ave PSMs	PSM STDev	Charge	Ave Xcorr	SDev Xcorr	Ave ΔM
Peptide-1	ALKDAQTNSIHPPF	1441.741	11						
Peptide-2	ALKDAQTNSIHPPFH	1578.801	13	1.00	0.00	3 & 4	3.46	1.02	-0.00058
Peptide-3	ALKDAQTNSIHPPFHL	1691.884	19	45.25	12.97	3	5.46	0.59	-0.00091
Peptide-4	ALKDAQTNSIHPPFHLV	1790.953	19	1.00	0.00	3	2.77	0.44	-0.00102
Peptide-5	ALKDAQTNSIHPPFHLVI	1904.038	14						
Peptide-6	ALKDAQTNSIHPPFHLVIH	2041.095	23	4.33	0.58	4	5.08	0.29	-0.00183
Peptide-7	ALKDAQTNSIHPPFHLVIHT	2142.146	17						
Peptide-8	ALKDAQTNSIHPPFHLVIHTM	2273.183	16						
Peptide-9	ALKDAQTNSIHPPFHLVIHTMS	2360.215	14						
Peptide-10	ALKDAQTNSIHPPFHLVIHTMSD	2475.243	12						
Peptide-11	ALKDAQTNSIHPPFHLVIHTMSDS	2562.273	7						
Peptide-12	ALKDAQTNSIHPPFHLVIHTMSDSE	2691.319	5						
Peptide-13	ALKDAQTNSIHPPFHLVIHTMSDSEV	2790.388	2						
Peptide-14	ALKDAQTNSIHPPFHLVIHTMSDSEVNQ	3032.483	9						
Peptide-15	ALKDAQTNSIHPPFHLVIHTMSDSEVNQE	3161.531	9						
Peptide-16	ALKDAQTNSIHPPFHLVIHTMSDSEVNQEAKPE	3586.755	2						
MBP -1	AVNKDKPLGAVALKSYEEE	2061.088	24	62.00	14.31	3	5.77	0.54	0.000358
MBP -2	KDTGKVTVEHPDKLEE	1938.016	23	50.00	26.34	3	5.17	0.36	-0.00135
MBP -3	NYLLTDEGLE	1166.558	24	29.25	10.18	2	3.35	0.17	-0.00046
MBP -4	LYKDPRIAATME	1343.736	19	20.00	10.61	2	2.99	0.32	-4.6E-05
MBP -5	LAKEFLE	849.475	22	7.33	5.13	2	2.21	0.19	-0.00038
MBP Ave				33.72					
Sumo Avg				0.00					
				Relative to MBP Control Peptides					
Peptide #	Sequence	MH+ [Da]		Ave PSMs	PSM /MBP	Relative			
Peptide-1	ALKDAQTNSIHPPF	1441.741		1.00	2.97				
Peptide-2	ALKDAQTNSIHPPFH	1578.801		45.25	134.21	1.0			
Peptide-3	ALKDAQTNSIHPPFHL	1691.884		1.00	2.97				
Peptide-4	ALKDAQTNSIHPPFHLV	1790.953							
Peptide-5	ALKDAQTNSIHPPFHLVI	1904.038							
Peptide-6	ALKDAQTNSIHPPFHLVIH	2041.095		4.33	12.85	0.1			
Peptide-7	ALKDAQTNSIHPPFHLVIHT	2142.146							
Peptide-8	ALKDAQTNSIHPPFHLVIHTM	2273.183							
Peptide-9	ALKDAQTNSIHPPFHLVIHTMS	2360.215							
Peptide-10	ALKDAQTNSIHPPFHLVIHTMSD	2475.243							
Peptide-11	ALKDAQTNSIHPPFHLVIHTMSDS	2562.273							
Peptide-12	ALKDAQTNSIHPPFHLVIHTMSDSE	2691.319							
Peptide-13	ALKDAQTNSIHPPFHLVIHTMSDSEV	2790.388							
Peptide-14	ALKDAQTNSIHPPFHLVIHTMSDSEVNQ	3032.483							
Peptide-15	ALKDAQTNSIHPPFHLVIHTMSDSEVNQE	3161.531							
Peptide-16	ALKDAQTNSIHPPFHLVIHTMSDSEVNQEAKPE	3586.755							

2.4.7 Structure-function analysis of TM1.

The cumulative results of our assay indicate a role for TM1 in IAP catalysis.

Direct comparison of activity was possible because the truncated IAPΔN23 construct remains stable and unchanged in oligomeric state compared to full length; such an experimental set up is expected to be difficult to probe other TM helices, such as TM6 or TM9 implicated previously in substrate binding (54,63). The lower V_{\max} , somewhat higher K_m , more promiscuous cleavage, as well as weaker inhibition profile of IAPΔN23 compared to full length IAP favors our proposed role for TM1 primarily in forming the native conformation of the active site over the possibility of substrate gating. For

example, TM1 could support TM7 in the proper position for Asp220, or provide physicochemical nuances relevant to proper substrate positioning within the active site. Taken together, our study reveals numerous heretofore unappreciated nuances of IAP family members. Our results and methodology set the stage for efficient in vitro investigations of this important enzyme class with unprecedented biochemical detail.

3 Chapter 3: Both positional and chemical variables control in vitro proteolytic cleavage of a presenilin ortholog

3.1 Publication and author contributions

The data presented in Chapter 3 has been published in Journal of Biological Chemistry with a citation: Naing, S. H., Kalyoncu, S., Smalley, D. M., Kim, H., Tao, X., George, J. B., Jonke, A. P., Oliver, R. C., Urban, V. S., Torres, M. P., and Lieberman, R. L. (2018) Both positional and chemical variables control in vitro proteolytic cleavage of a presenilin ortholog. *The Journal of biological chemistry*. The site-directed mutagenesis, FRET-based enzyme assays, CD thermal melts and protein expression/purification were carried out by Swe Htet Naing, Sibel Kalyoncu, Xingjian Tao and Josh George under the guidance of Dr. Raquel Lieberman. The gel-based assays and isotopic ^{18}O labelling experiment were carried out by Swe Htet Naing, Xingjian Tao and Josh George. Mass spectrometric analysis was carried out by David Smalley, Hyojung Kim, Alex Jonke and Matthew Torres. Small angle X-ray scattering (SAXS) study and *ab initio* modelling were performed by Ryan Oliver and Volker Urban.

3.2 Introduction

Despite intense work in the area, how IPs distinguish substrates from non-substrates and thus avoid deactivating a significant percentage of the proteome remains unclear (2). For γ -secretase, ~90 different substrates have been reported, and for SPP, the number is ~30, yet a consensus motif for substrate cleavage remains elusive (5,59). Substrate sequences exhibit high variability in amino acid sequence and length (87,88). Early studies suggested that helix-breaking residues within the TM substrate at or around

the cleavage site are required. These residues were proposed to destabilize the TM helix and thus serve as a driving force for exposure of the scissile bond to the protease (80,89,90). However, this proposal has not persisted, as many canonically helical residues have been reported as cleavage sites for IAPs (51,52). Conversely, residues other than aspartate within the IAP enzyme that affect catalysis – kinetics, cleavage specificity, substrate and water entry – are largely obscure. For example, the specific roles of Tyr and Gly within the highly conserved YD...GxGD motif remain to be clarified. Finally, recent structures (54,57) do not clarify substrate or water entry. The TM helices proximal to the proposed substrate-gating motif PAL (63,151,152) need to undergo a substantial conformational change to enable entry of an exogenous TM substrate to the active site, a motion that is chemically incompatible with the presence of water in the active site.

Here in Chapter 3, we compare *in vitro* kinetic parameters and cleavage sites of an IAP ortholog from *Methanoculleus marisnigri* (mIAP) toward two substrates, one fortuitous (angiotensinogen of renin, a soluble aspartyl protease) (56) and one biological (fragments of amyloid precursor protein C-terminal segment, C100). Our studies reveal a preference for a polar residue, Thr, at the scissile bond. Using the renin substrate, we first examined mutants of the YD...GxGD and PAL motifs. We demonstrate that kinetics are impaired except in the case of Y161F, and the His-Thr cleavage site dominates (56). mIAP cleaves the C100 sequence at Ala-Thr, the so-called γ -secretase ‘ γ -site’ (153) leading to the formation of Alzheimer-associated amyloid- β species A β ₄₂ (154), faster and with higher affinity in bicelles than renin or C100 in detergent solution. The ortholog also cleaves the so-called γ -secretase ‘ ϵ -site’ corresponding to longer A β peptides (153), centered around Thr. However, Thr-scanning mutagenesis within the renin substrate

reveals cleavage is preferred at the original site, even absent a Thr residue. Our systematic biochemical study further refines the features that govern peptide hydrolysis by IAPs, providing a foundation for elucidating substrate entry and other mechanistic details that better enable the development of selective inhibitors for diseases associated with IAP catalysis, such as Alzheimer and Hepatitis C viral infection, without affecting processing of substrates for other biological processes.

3.3 Methods

3.3.1 Molecular biology

The gene sequence for mIAP was cloned into the pet 22b(+) (Novagen) vector with C-terminal hexa-histidine tag as described previously (56). MRS_{WT} was cloned in pEX-K vector by MWG Operon. Substrates MCSTV (MBP-TVIVITLVML-SUMO) and MCSGG (MBP-GGVIVITLVM-SUMO) were cloned into pMAL-c4x and purchased from GenScript. Mutations to mIAP, MRS substrates, and MCS were carried out via site-directed mutagenesis (Agilent QuickChange Lightning kit, primer sequences in (Table 3.1) and verified by DNA sequencing (Operon).

Table 3.1. Primers used for site-directed mutagenesis of enzyme IAP and substrates MRS and MCS

IAP mutants	Forward (F) and Reverse (R) Primers (5'-3')
Y161A	F: GCTGCTCGCGGTCGCCGACGCCATATCGGTCTACC R: GGTAGACCGATATGGCGTCGGCGACCGCGAGCAGC
Y161F	F: GCTGCTCGCGGTTCTCGACGCCATATCGGTCTACC R: GGTAGACCGATATGGCGTCGAAGACCGCGAGCAGC
D162N	F: GCTGCTCGCGGTTCTACAACGCCATATCGGTCTACC R: GGTAGACCGATATGGCGTTGTAGACCGCGAGCAGC
G219A	F: CGTTCGTCATGGGTATGGCCGATCTCATCATGC R: GCATGATGAGATCGGCCATACCCATGACGAACG
D220N	F: CGTCATGGGTATGGGCAATCTCATCATGCCCTCG R: CGAGGGCATGATGAGATTGCCCATACCCATGACG
Q272A	F: GTCAACAAGGGCAACCCCGCGGCGGGTCTCCCCCCC R: GGGGGGGAGACCCGCCGCGGGGTTGCCCTTGTTGAC
A273P/G274A	F: GTCAACAAGGGCAACCCCGAGCCCGCGCTCCCC CCTTAAACG R: CGTTTAAGGGGGGGAGCGCGGGCTGGGGGTTGCC CTTGTTGAC
L275F	F: GGGCAACCCCCAGGCGGGTTTTCCCCCCTTAAACGGCG R: CGCCGTTTAAGGGGGGAAAACCCGCCTGGGGGTTGCCC
MRS mutants	Forward (F) and Reverse (R) Primers (5'-3')
T10L	F: CCACCTGGTGATCCACCTCATGTCGGACTCAG R: CTGAGTCCGACATGAGGTGGATCACCAGGTGG
P3T	F: GCGCAGACTAATTTCGATCCACACCTTCCACCTGGTG R: CACCAGGTGGAAGGTGTGGATCGAATTAGTCTGCGC
L6T	F: CACCCCTTCCACACGGTGATCCACACC R: GGTGTGGATCACCGTGTGGAAGGGGTG
P3T, T10L	F: GCGCAGACTAATTTCGATCCACACCTTCCACCTGGTG R: CACCAGGTGGAAGGTGTGGATCGAATTAGTCTGCGC
L6T, T10L	F: CACCCCTTCCACACGGTGATCCACCTC R: GAGGTGGATCACCGTGTGGAAGGGGTG

Table 3.1 (Continued)

MRS to MCS10	Forward (F) and Reverse (R) Primers (5'-3')
Round 1	F: GAAAGACGCGCAGACTAATTCGGGCGGCGTCTTCCACCTG GTGATCCACACC R: GGTGTGGATCACCAGGTGGAAGACGCCGCCCGAATT AGTCTGCGCGTCTTTC
Round 2	F: CAGACTAATTCGATCCACCCCGTCATCGCGGTGATCCACA CCATGTCGGA R: CCGACATGGTGTGGATCACCGCGATGACGGGGTGG ATC GAATTAGTCTG
Round 3	F: GACTAATTCGATCCACCCCTTCCACCTGACGGTCATCGTCA TGTCGGACTCAGAAGTCAATCAAGAA R: TTCTTGATTGACTTCTGAGTCCGACATGACGATGACCGTC AGGTGGAAGGGGTGGATCGAATTAGTC
MCS10 to MCS15	Forward (F) and Reverse (R) Primers (5'-3')
Round 1	F: GGCGGCGTCGTCATCGCGACGGTCATCGTCATCACCTAT GTCGGACTCAGAAGTCAATCAAGAAGCTAAGCC R: GGCTTAGCTTCTTGATTGACTTCTGAGTCCGACATAGGT GATGACGATGACCGTCGCGATGACGACGCCGCC
Round 2	F: CGTCATCGCGACGGTCATCGTCATCACCTTGGTGATGAT GTCGGACTCAGAAGTCAATCAAGAAGCTAAGCC R: GGCTTAGCTTCTTGATTGACTTCTGAGTCCGACATCATC ACCAAGGTGATGACGATGACCGTCGCGATGACG

3.3.2 Expression and purification of enzyme variants and fusion substrates

Plasmids containing IAP (wild type and variants) were transformed into *E. coli* Rosetta 2 cells (Novagen). Large scale growth of bacteria, membrane isolation and protein purification steps were carried out as described previously (56), with the following modifications found to improve protein yield: cells were induced with 0.2 mM isopropyl- β -D-1-thiogalactopyranoside (IPTG) at OD_{600nm} = 1.5, followed by growth overnight at 22°C. During nickel affinity purification, weakly bound impurities were first

removed with 5% Buffer B (50 mM Hepes (pH 7.5), 500 mM NaCl, 500 mM imidazole, 0.1% DDM) before the full gradient was applied. Protein purity after size exclusion chromatography (SEC) was assessed by sodium dodecyl sulfate polyacrylamide gel electrophoresis (SDS-PAGE) (12% polyacrylamide) stained with Coomassie. Pure protein was concentrated and exchanged into phosphate-buffered saline (PBS, 10 mM sodium phosphate, pH 7.2, 150 mM NaCl) supplemented with 0.05% DDM using a 15 mL Amicon Ultra 50K MWCO concentrator (Millipore). The protein concentration was measured using a ThermoScientific NanoDrop spectrophotometer. The calculated extinction coefficient, $\epsilon = 33,920 \text{ M}^{-1} \text{ cm}^{-1}$, and molecular mass from the amino acid sequence were obtained by ExPASy ProtParam (155).

Plasmids encoding substrates were transformed into *E coli* BL21 DE3 (Novagen). A single colony was inoculated in 200 mL LB media supplemented with 50 $\mu\text{g mL}^{-1}$ kanamycin except for MCSTV and MCSGG, which were supplemented with 60 $\mu\text{g mL}^{-1}$ ampicillin. Inoculum was grown overnight in an orbital shaker (225 rpm, 37°C). Large cultures (1L) were inoculated with 20 mL of overnight culture and grown until an $\text{OD}_{600\text{nm}} = 0.6 - 0.8$ was reached. After cooling the cultures to 18°C, protein expression was induced with an addition of 1 mM IPTG. Cultures were grown overnight and harvested by centrifugation at 5,000 x g followed by flashed-cooling with liquid nitrogen to store at -80°C. The purification of substrates proteins was carried out as described previously (56) except for MCS15, which was present in a mixture of aggregated and monomeric protein. For MCS15, in addition to nickel and amylose affinity chromatography, SEC using HiLoad 16/600 Superdex 75 pg was used to further fractionate monomer from aggregate. The purity of protein was assessed by Coomassie-

stained SDS-PAGE (12% polyacrylamide). Pure protein was concentrated and exchanged into PBS, 0.05% DDM using a 15 mL Amicon Ultra MWCO 30K concentrator (Millipore). Protein was measured on a ThermoScientific NanoDrop spectrophotometer using a calculated extinction coefficient, $\epsilon = 69,330 \text{ M}^{-1} \text{ cm}^{-1}$, as before (155).

3.3.3 FRET assay and inhibitor studies

Assays with Ren390FRET (Anaspec) were conducted as described previously (56). For C100FRET (Millipore), lyophilized peptide was dissolved in DMSO to generate a stock solution at 1250 μM . A working stock solution (500 μM) was prepared by diluting the original stock with 10 mM sodium phosphate, pH 7.2, 150 mM NaCl (PBS), 0.05% (w/v) DDM. The 500 μM C100FRET working stock was sonicated (Branson ultrasonics corporation) at 50-60 Hz, 117 V, 0.7 Amp for 30 min prior to being diluted to 3-40 μM solutions with PBS with 0.05% DDM and dispensed into black-bottomed, non-binding 96-well plates (Corning). Plates were covered with optical adhesive film (Micro-Amp) and incubated at 37 °C for 30 min, a process that resolved the initial high background from the C100FRET substrate. Freshly purified IAP (0.5 μM , in PBS 0.05% DDM and reconstituted inside 5% (v/v) bicelles (56)) was then added to the substrate solution in the 96-well plate. The fluorescence readings were acquired every 2 min for 2.5 h at 37°C in a Synergy H4 plate reader (BioTek, $\lambda_{\text{ex}} = 350 \pm 9 \text{ nm}$, $\lambda_{\text{em}} = 440 \pm 9 \text{ nm}$). The initial velocity was determined from the fluorescence readings over the first 2 h. The background reading at each substrate concentration was subtracted and the fluorescence reading was converted from arbitrary fluorescence unit (Afu) to concentration of product (nM) by using the standard calibration curve of free NMA. The inner filter effect was not observed for the NMA-DNP donor-acceptor pair. GraphPad Prism 5 software was used

for Michaelis-Menten kinetic analysis as described previously (56). Twelve replicates from independent batches of cell paste and enzyme purification were used in data analysis.

For inhibitor studies, (ZLL)₂ketone (Calbiochem) was dissolved in DMSO to prepare 1 mM stock. (ZLL)₂ketone was diluted to a final 2- to 10-fold molar excess of the enzyme in the activity assay and preincubated with purified enzyme for an hour at 37°C. C100FRET was then added and the assay conducted as above. Kinetics data of nine independent replicates were analyzed as described above.

3.3.4 Gel-based assay

Varying concentrations of mIAP (1-8 μ M), prepared in PBS with 0.05% DDM or 5% (v/v) bicelle, were incubated with MCS10 (5 μ M) at 37°C for 24 h. For time course experiments, 16 μ M of mIAP was incubated with MCS10 (5 μ M) and the reaction was quenched at different time points by adding equal volume of Laemmli SDS-PAGE sample loading dye containing β -mercaptoethanol, followed by storage at -20 °C. For experiments with (ZLL)₂ketone, a range of inhibitor concentration (8-32 μ M) was pre-incubated with 16 μ M of IAP at 37°C before adding MCS10 (5 μ M). The cleavage reaction samples were separated by SDS-PAGE (12% (w/v) polyacrylamide) followed by transfer onto polyvinyl difluoride (PVDF) membrane (MilliPore). Standard Western blot procedures were performed using MBP-probe mouse monoclonal IgG primary antibody (Santa Cruz, 1:1000) and horseradish peroxidase (HRP)-conjugated goat anti-mouse monoclonal IgG secondary antibody (KPL, 1:5000). The PVDF membrane was sprayed with HyGlo Quick Spray (Denville) and visualized on Amersham Imager 600 (GE Healthcare).

For LC-MS analysis, gel assay was set up as described above except that ice-cold acetone (6.5 x sample volume) was added to quench reaction at 24 h for samples containing MCS10 substrate and at 24 h and 48 h for sample containing MRS substrate, followed by storage at -20 °C. After decanting the acetone, samples were analyzed by SDS-PAGE. LC-MS analysis of samples was carried out as described previously (56) with the following modifications. An UltiMate™ 3000 RSLCnano System UPLC system (Dionex) was coupled to a Q Exactive Plus Mass Spectrometer (Thermo Scientific). The Mascot Search engine (Version 2.6.0) was used with Proteome Discoverer 2.1 (Thermo Scientific). Only peptide spectral matches with expectation value of less than 0.01 (“High Confidence”) were used.

For isotopic ^{18}O labelling, first PBS with 0.05% DDM (75 μL) was lyophilized in a Speed Vac (Savant) for 30 min, after which 75 μL of heavy water H_2^{18}O (Cambridge Isotopes) was added. Purified mIAP (16 μM) and either MRS_{WT} or MCS10 (5 μM) was then added to run gel-based assay at 37°C for 24 h. LC-MS analysis of samples was carried out as described above.

3.3.5 CD

CD spectra and thermal melts were acquired on a Jasco J-810 spectropolarimeter equipped with Neslab RTE 111 circulating water bath and a Jasco PTC-4245/15 temperature control system using a 0.1-cm cuvette. CD spectra of IAP variants (5 μM in 20 mM HEPES (pH 7.5), 250 mM NaCl, 0.05% DDM) were acquired from 300-200 nm at room temperature. Data were blank-subtracted and converted to molar ellipticity $\Theta = (\Theta_{\text{obs}} \times 10^6)/(\text{pathlength (mm)} \times c \times n)$, where Θ_{obs} is the observed ellipticity (mdeg) at wavelength λ ; c is the protein or peptide concentration (μM); and n is the number of

residues. CD thermal melt was performed with a 1 °C min⁻¹ increase in temperature from 5 to 89°C. Both CD spectra and thermal were acquired with 15 averaged scans from 300-200 nm at a 200 nm min⁻¹ scan rate. Data at 222 nm were blank-subtracted, converted to molar ellipticity and plotted against temperature in GraphPad Prism 5.

3.3.6 SAXS and *ab initio* modeling

SAXS data for substrate solutions containing ~1 mg/mL of substrate in 20 mM Hepes (pH 7.5), 250 mM NaCl were collected at 12°C using a Rigaku BioSAXS-2000 instrument with 2D Kratky collimation and a rotating Cu anode X-ray source ($\lambda = 1.54187 \text{ \AA}$). Each sample was exposed for a total of 3 hours using multiple scans to confirm consistency between measurements and the absence of radiation damage. Matched buffers measured at an identical instrument configuration were used for background subtraction. Rigaku SAXSLab software was used for data reduction, and yielded a 1D plot of the scattered intensities over the range of momentum transfer $0.0104 < q < 0.6782 \text{ \AA}^{-1}$ [$q = 4\pi \sin(\theta)/\lambda$, 2θ is the scattering angle and λ is the X-ray wavelength].

Three-dimensional reconstruction of the substrate structure from the SAXS data was performed using the ATSAS software suite (156). Briefly, the pair-distribution function $P(r)$ (using $0.0104 < q < 0.3464 \text{ \AA}^{-1}$) was determined from an indirect Fourier transform of the scattering data for each substrate via GNOM. The DAMMIF tool was then used to rapidly generate 17 compact bead representations of the scattering particle. This initial collection of models was clustered using DAMCLUST, and the averaged model from the most populated cluster was used with DAMSTART to generate a fixed core (using a cut-off volume of one half the excluded volume of the particle) for further

refinement in DAMMIN. Ten refined models from DAMMIN (slow-mode) were similarly clustered, and a representative model of the most populated cluster was compared to results from a rigid-body model reconstruction. CORAL was employed for rigid-body modeling, performing translation and rotation of high-resolution PDB structure fragments, as well as constructing dummy atom segments of defined lengths linking between domains and at the C-terminus. MBP used for rigid-body modelling was excised from PDB 5CL1, chain A: residues 1-368. The structure for the SUMO domain was taken from the first of 20 conformers in the collection of NMR structures deposited under PDB 1L2N; the first 20 and C-terminal 5 amino acids are absent in the NMR structure. Dummy atom representations of the linker region containing the substrate target sequence, omitted residues of the SUMO domain, and C-terminal hexahistidine-tag were all constructed using CORAL.

3.4 Results

3.4.1 Enzymatic analysis of mIAP mutants

To assess contributions of particular residues to catalysis (Table 3.2, Figure 3.1A, see below), we employed a continuous kinetics FRET peptide assay in combination with a discontinuous gel-based assay, methodology we reported previously (56). Kinetic assays with mIAP variants were conducted using the fortuitous renin 390 FRET peptide. Due to the incompatibility of the FRET assay components with mass spectrometry analysis, we turned to a gel-based assay that uses a fusion protein (MRS_{WT}) in which the renin substrate IHPFHLVIHT is flanked by *E. coli* maltose binding protein (MBP) and yeast small ubiquitin-like modifier (SUMO). Cleavage profiles from a gel-based assay are analyzed by liquid chromatography tandem mass spectrometry (LC-MS) analysis

(56). In aqueous solution, MRS_{WT} adopts an elongated structure as visualized by the small angle X-ray scattering (SAXS) envelope (Figure 3.1B, Figure 3.2), rendering the desired 10-residue angiotensinogen sequence (IHPPHFLVIHT10) accessible to detergents and mIAP.

Table 3.2. Rationale of mIAP mutation and kinetics parameters associated with each mutant.

IAP variants	Rationale	K_m (μM)	V_{max} (nM min⁻¹)	k_{cat} x10⁻³ (min⁻¹)	(k_{cat}/K_m) x 10⁻³ (μM⁻¹ min⁻¹)
WT		7.8 \pm 0.7	4.1 \pm 0.1	8.1 \pm 0.3	1.0 \pm 0.1
Y161A	Catalytic YD ₁₆₂ motif	8.9 \pm 0.8	1.8 \pm 0.1	3.6 \pm 0.2	0.40 \pm 0.04
Y161F	Catalytic YD ₁₆₂ motif	5.8 \pm 0.5	3.6 \pm 0.1	7.2 \pm 0.6	1.2 \pm 0.5
G219A	Catalytic GxGD ₂₂₀ motif	9.4 \pm 0.6	2.4 \pm 0.2	4.8 \pm 0.2	0.51 \pm 0.04
Q272A	Substrate gating QAGL ₂₇₅ motif.	6.2 \pm 0.6	1.6 \pm 0.1	3.2 \pm 0.1	0.52 \pm 0.05
A273P/G274A	Double mutant to generate presenilin PAL substrate gating motif	4.9 \pm 0.7	0.51 \pm 0.04	1.0 \pm 0.4	0.21 \pm 0.05
L275F	FAD mutation in presenilin; in tertiary structure, located between two catalytic aspartates	3.9 \pm 0.5	1.5 \pm 0.1	3.1 \pm 0.1	0.8 \pm 0.1

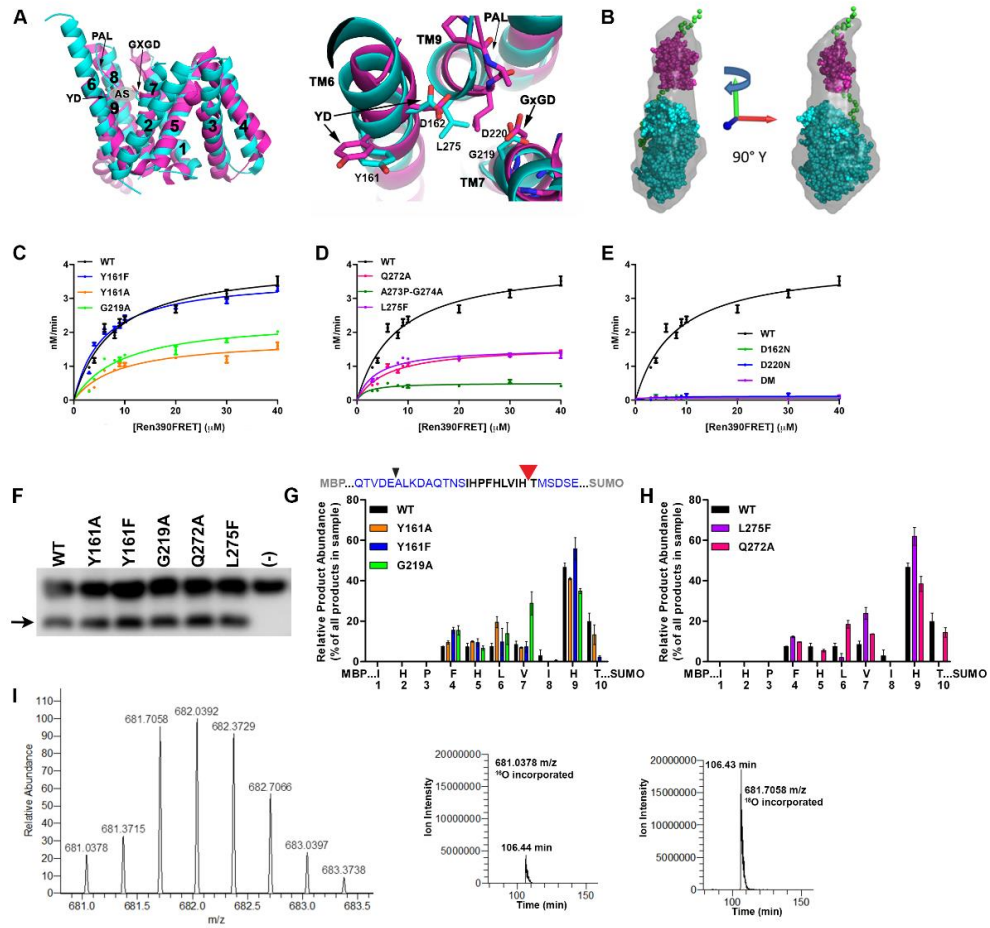


Figure 3.1. Characterization of mIAP mutants. (A) Superposition of mIAP (PDB ID 4HYC, cyan) and presenilin (PDB 5A63 chain B, magenta) structures using secondary structure matching (157). TM helices are numbered from N- to C-terminus. Key sequence motifs highlighted. AS= active site. (B) *Ab initio* model of MRS_{WT} obtained by SAXS. (C, D, E) Michaelis-Menten kinetic analysis of mIAP variant cleavage of Ren390FRET. (F) Gel assay of mIAP mutants using MRS_{WT} substrate. Negative control without enzyme is indicated by (-). The uncut substrate and cleavage products (indicated by arrow) are detected via anti-MBP Western blot. (G, H) Cleavage profiles of MRS substrate were generated by Glu-C digestion of the N-terminal product, facilitated by a C-terminal Glu within MBP (black triangle). Major cleavage site is His₉-Thr₁₀ (red triangle). The relative abundance of each reporter peptide, compared to total peptide spectral matches (PSMs) of seven independent peptide products formed by proteolytic cleavage, is shown. Error bars represent the standard deviation from LC-MS analytical replicates. (I) LC-MS spectrum of reporter peptide (z=3) displaying 350% more ¹⁸O incorporation than ¹⁶O. (Left) The extracted ion current (XIC) for relative abundance of peptide (ALKDAQTNSIHPFHLVIH) with ¹⁶O incorporation (middle) versus ¹⁸O incorporation at the C-terminal of N-terminal product (right) from enzymatic cleavage. Approximately 11.8% of peak at 681.7058 is due to two-¹³C isotope of the ¹⁶O-containing peptide.

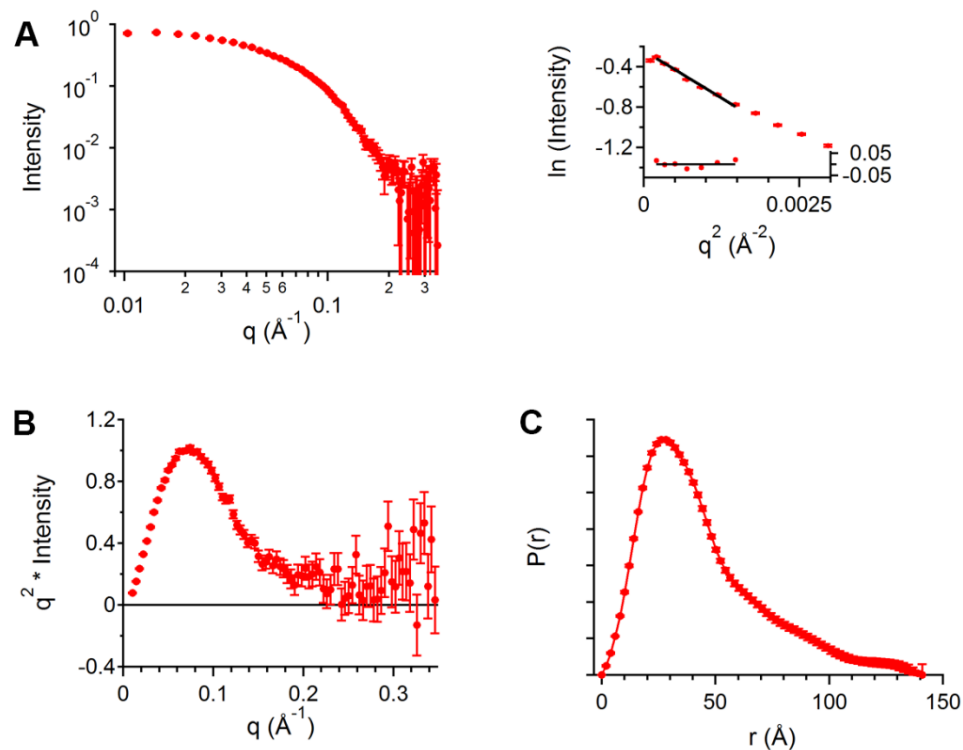


Figure 3.2. SAXS analysis of MRS_{WT} substrate. (A) Buffer-subtracted SAXS $I(q)$ data for MRS at concentration of $\sim 1 \text{ mg mL}^{-1}$. The linear region of the Guinier plot at low- q (right) and the residuals from the fit to the experimental data, such that $q \cdot R_g < 1.3$, yield a radius of gyration (R_g) of $33.6 \pm 0.2 \text{ \AA}$ for MRS_{WT}. (B) A Kratky plot of these same data indicates that MRS_{WT} is well folded. (C) The pairwise distance distribution function $P(r)$ yields a maximum particle dimension (D_{max}) of 141 \AA . The shape of the $P(r)$ function suggests an elongated molecule, or extended domain.

mIAP variants Y161A, Y161F, and G219A within the YD₁₆₂...GxGD₂₂₀ motif and Q272A, L275F on the C-terminal helix near the presenilin PAL motif (Table 3.2) were purified and biophysically characterized as for wild-type (WT). Like WT, all mIAP mutants exhibit α -helical signatures (Figure 3.3). Although the thermal melts did not yield a sigmoidal curve, both WT and mutants display similar curves, indicating relative structural characteristics are retained upon introducing mutations.

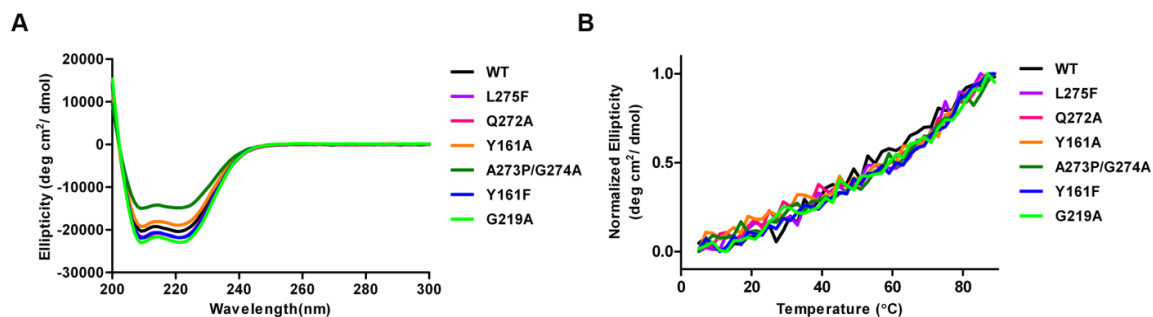


Figure 3.3. Biophysical characterization of mIAP mutants. (A) Circular dichroism (CD) spectra of WT IAP and mutants acquired at 4°C. (B) CD thermal melts over the range of 5-90°C, monitored at 222 nm.

Kinetic and cleavage site profiling reveal that mIAP is largely tolerant to mutation, with primary defects observed in catalytic efficiency and details of processivity. The only variant tested that exhibits Michaelis-Menten kinetic properties indistinguishable from WT is mIAP_{Y161F}, representing the Tyr in the Y161D catalytic motif (Figure 3.1C, Table 3.2). This result indicates that the phenyl ring, but not the hydroxyl group, is the relevant chemical feature needed for catalysis. This result is surprising given the dearth of hydrogen bond donor/acceptors in the active site that might be capable of activating water or stabilizing an anionic tetrahedral intermediate during hydrolysis. In support for the importance of the phenyl ring, catalysis by mIAP_{Y161A} is impaired, with a reduced V_{max} and two-fold lower catalytic efficiency (Figure 3.1C, Table 3.2). The catalytic motif mutant, mIAP_{G219A}, adjacent to the aspartate in GxG219D, and the site of the familial Alzheimer disease (FAD) mutant G384A in presenilin (158,159), exhibits catalytic rates similar to mIAP_{Y161A} (Table 3.2). Previous studies of the G384A presenilin variant (160) and corresponding variant in other SPP homologs (52,161) detected reduced end product via immunoblot. Consistent with our

measurements (Table 3.2), one additional study of the G384A presenilin variant reported two-fold reduced V_{max} compared to WT enzyme (162). While rigidifying this region with the G219A substitution is detrimental to optimal orientation of Asp220 for catalysis, it is noteworthy that the reaction still proceeds.

In terms of substrate entry, replacing the mIAP sequence AGL275 with PAL435 found in presenilin (63,151,152) reduces catalytic efficiency by ~80% compared to WT, indicating PAL is not a favorable substitute (Figure 3.1D, Table 3.2). For mIAP_{L275F}, corresponding to the presenilin L435F FAD mutant (107,163,164), catalytic efficiency is similar to WT, but this is due to the countering effect of a ~60% decrease in V_{max} combined with 50% improvement in K_m (Figure 3.1D, Table 3.2). More favorable substrate binding to the enzyme when the aromatic Phe is present appears to be unfavorable to some aspect of catalysis. For mIAP_{Q272A}, immediately N-terminal to AGL275, catalytic efficiency is half of WT due to decreased V_{max} . K_m remains near that of WT (Figure 3.1D, Table 3.2), so this residue appears not to modulate substrate binding and may instead play a cursory role in positioning other helices for catalysis.

Given the sensitivity of our FRET assay in detecting low levels of cleavage for the aforementioned variants, we tested the hypothesis that polar Asn in place of the negatively charged Asp residues supports catalysis. Each of the catalytic mutants, mIAPD162N, mIAPD220N, and the double mutant (DM) mIAPD162N/D220N were found to be inactive (Figure 3.1E). Thus, the specifically charged state(s) of the aspartic residues are critical for mIAP proteolysis.

Variants of mIAP exhibiting measurable activity in the FRET assay cleave MRS_{WT} (Figure 3.1F) with profiles that mirror WT mIAP, namely, a predominant cut site

at His9-Thr10 (Figure 3.1G,H, Figure 3.4, Supplementary Table S1.xlsx). However, differences in overall cleavage profiles suggest that members of the YD...GxGD and PAL sequence motifs proximal to the catalytic aspartates (Figure 3.1A) influence processivity of IAP cleavage when presented with the renin substrate. For example, mIAPL275F displayed higher cleavage site specificity than WT, with little to no product at positions His5-Leu6, Ile8-His9, Thr10-Met (from SUMO, not in Ren390FRET). Thus, tighter substrate binding by mIAPL275F, reflected in the lower K_m value in the FRET assay, appears to be detrimental to processivity. In addition, for WT-like mIAPY161F, cleavage at Thr10-Met11, the second-most preferred site for WT and beyond the sequence harbored by Ren390FRET, is substantially diminished.

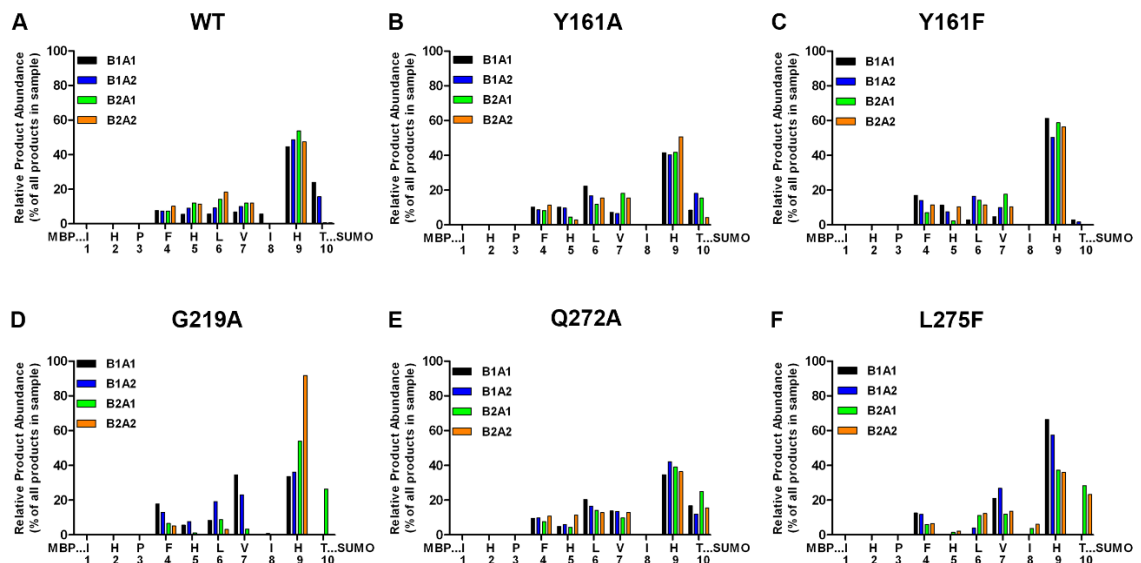


Figure 3.4. All LC-MS replicates for MRS substrates cut by mIAP mutants. MRS cleavage profile processed by (A) WT mIAP, (B) Y161A, (C) Y161F, (D) G219A, (E) Q272A, (F) L275F. For each mutant, B1, biological replicate 1; B2, biological replicate 2; A1, analytical replicate 1; A2, analytical replicate 2. Relative product abundance quantified as described in Figure 3.1. Raw data in Supplementary Table S1.xlsx.

3.4.2 Role of bulk water in mIAP catalysis

In the case of soluble aspartyl proteases, water is activated for nucleophilic attack (165). To test for incorporation of bulk water in mIAP catalysis, we carried out the MRS_{WT} cleavage reaction in the presence of 75% heavy water H₂¹⁸O. LC-MS analysis of the resulting cleavage products reveals robust ¹⁸O incorporation at the C-terminus of the cleavage products, exceeding the observed ¹⁶O incorporation in the expected proportion (Figure 3.1I). To our knowledge, this isotope partitioning experiment is the first to provide direct evidence for a role for bulk water in an IAP.

3.4.3 mIAP cleavage of the presenilin C100 substrate in the ‘γ-site’ region

Kinetic analysis of mIAP was expanded next to a second substrate, C100FRET, which contains the ‘γ-site’ from the γ-secretase C100 substrate (GGVVIATV flanked by N-methyl anthranilate (NMA fluorophore) and lysine-modified with 2-nitrophenol (DNP) quencher, followed by triple D-Arg) associated with Aβ₄₂ production. Adaptation of our continuous assay for this substrate was straightforward; the initial velocity is sustained over the first 2 h of the incubation, and arbitrary fluorescence units (Afu) were converted to product concentration product with a calibration curve using free NMA (Figure 3.5).

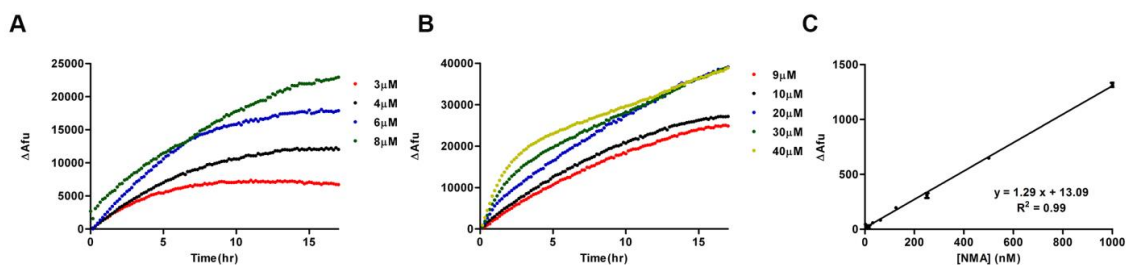


Figure 3.5. C100FRET assay development. (A, B) Determination of initial velocity region from 20 h assay. Fluorescence readings for mIAP incubated with different concentrations of C100FRET are detected for 20 h. Initial velocity is within the first 2 h. (C) Standard calibration curve of NMA plotting the background-subtracted arbitrary fluorescence unit (ΔA_{fu}) against concentration of NMA (nM).

Reactions of mIAP and C100FRET were conducted in n-dodecyl- β -D-maltoside (DDM) and bicelles. mIAP cleaves C100FRET with similar V_{max} in detergent and in bicelles, but K_m is notably more favorable in bicelles (Figure 3.6A, Table 3.3). As expected, catalytic mutants mIAP_{D162A}, mIAP_{D220A}, and mIAP_{D162A/D220A} failed to cleave C100FRET (Figure 3.6A) and (ZLL)₂ketone is a competitive inhibitor of WT mIAP, with the same K_i value we reported previously (56) (Figure 3.6B). For reactions in DDM, V_{max} is nearly four-fold faster and K_m is 20% lower for C100FRET compared to Renin390FRET, resulting in ~5-fold higher catalytic efficiency (Table 3.2). In bicelles, the catalytic efficiency is even more pronounced for C100FRET, 15-fold higher more efficient compared to Renin390FRET. The reason for the dramatic efficiency difference is not immediately obvious, but is consistent with the idea that C100FRET derives from a biological substrate whereas Ren390FRET, while competent for catalysis, is not tailored to IAPs. Overall, our K_m is in the typical low micromolar range, similar to the soluble aspartyl protease renin (134), but mIAP is much less efficient. Prior studies using this substrate to study γ -secretase kinetics did not place absolute scale (166,167), so direct

comparisons are not possible. In other studies, where initial rates were evaluated via immunoblot quantitation after a set incubation time, our K_m is either 10-fold weaker (162) or 30-fold tighter than that of γ -secretase (125).

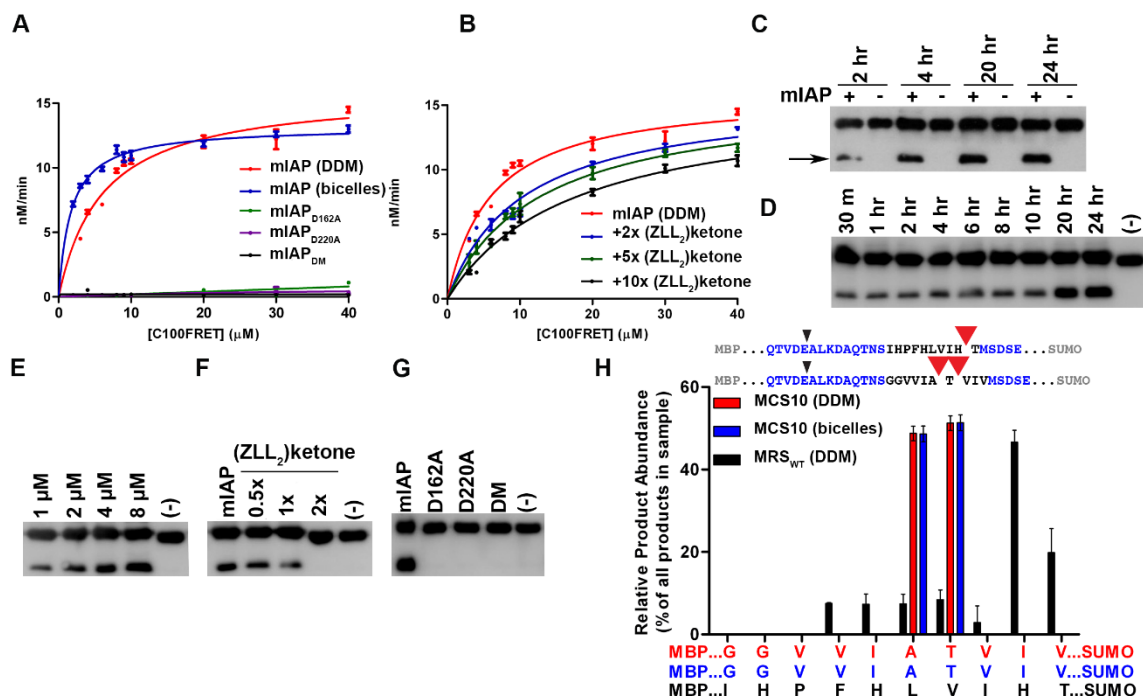


Figure 3.6 mIAP cleavage of C100 γ -site. (A) Michaelis-Menten kinetic analysis of C100FRET cleavage by WT mIAP in DDM and bicelles, and by catalytic mutants (D162A, D220A, and DM) in DDM. (B) Kinetic data for mIAP treated with increasing (ZLL)₂ketone. (C-G) Gel assay using MCS10 and mIAP, visualized by anti-MBP immunoblot. (C) Time course in DDM. (D) Time course in bicelles. (E) Product formation as a function of mIAP concentration. (F) Inhibition by (ZLL)₂ketone. (G) mIAP variants D162A, D220A, and DM are not active. Negative control without enzyme is indicated by (-). The uncut substrate and cleavage product (indicated by arrow) are detected as in Figure 3.1. All LC-MS data are presented in Supplementary Table S2.xlsx. (H) LC-MS analysis of MCS10 cleavage sites by mIAP in DDM and bicelles, compared to MRS_{WT} in DDM

Table 3.3 Kinetic parameters obtained from mIAP cleavage of C100FRET in DDM and bicelles and effect of (ZLL)₂ketone inhibitor

Enzyme	Inhibitor	K _m (μM)	V _{max} (nM min ⁻¹)	k _{cat} x 10 ⁻³ (min ⁻¹)	(k _{cat} /K _m) x 10 ⁻³ (μM ⁻¹ min ⁻¹)
IAP (DDM)	-	6.0 ± 0.7	15.9 ± 0.6	32 ± 1	5.3 ± 0.9
IAP (bicelles)	-	1.7 ± 0.1	13.2 ± 0.2	26 ± 1	16 ± 1
IAP	(ZLL) ₂ ketone				
	2x	10 ± 1	15.8 ± 0.9	32 ± 2	3.0 ± 0.7
IAP	5x	13 ± 2	15.9 ± 0.9	32 ± 2	2.5 ± 0.3
IAP	10x	17 ± 2	15.5 ± 0.8	31 ± 2	1.8 ± 0.3

To identify the cleavage site within the C100FRET sequence, we adapted our gel assay by generating MCS10, an analogous substrate in which the intervening sequence between MBP and SUMO in MRS_{WT} was converted to G₃₇GVVIATVIV₄₈. MCS10 contains the octapeptide sequence of C100FRET plus two more, IV₄₈, from C100. An increase in the N-terminal product was observed over the course of a 2-24 h reaction period in DDM (Figure 3.6C). Paralleling results from C100FRET, the reaction between mIAP and MCS10 in bicelles was faster than in DDM, as product was readily visible within 30 minutes followed by a continued increase over the duration of the experiment (Figure 3.6D). As expected, the reaction is dependent on IAP concentration, is inhibited by (ZLL)₂ketone, catalytic mutants mIAP_{D162A}, mIAP_{D220A} and DM mIAP_{D162A/D220A} are unable to cleave MCS10, and the substrate remains stable throughout the time course of the experiment (Figure 3.6E-G). LC-MS cleavage profiles for MCS10 reveal highly specific cut sites – Ala₄₂-Thr₄₃ and Thr₄₃-Val₄₄ – both in DDM and bicelles (Figure 3.6H, Figure 3.7A, Supplementary Table S2.xlsx). Isotope partitioning again demonstrates the

use of bulk water in the mIAP reaction (Figure 3.8). In sum, like results for mIAP cleavage of the MRS_{WT} substrate, these data indicate the involvement of a site-adjacent Thr residue using a typical protease reaction mechanism involving bulk water.

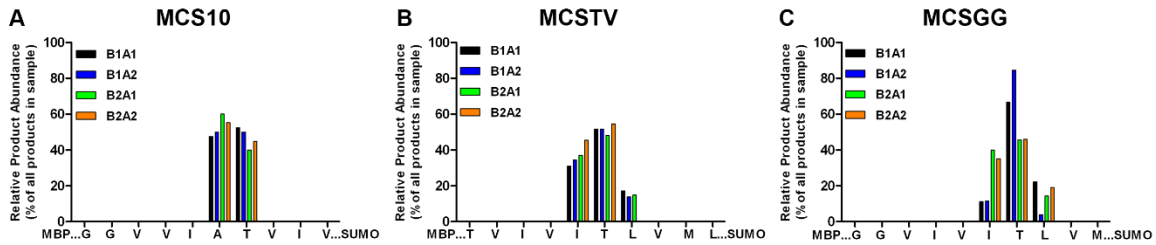


Figure 3.7. All LC-MS replicates for MCS-related substrates cut by mIAP WT. (A) Cleavage profile of MCS10. (B) Cleavage profile of MCSTV. (C) Cleavage profile of MCSGG. For each substrate, B1, biological replicate 1; B2, biological replicate 2; A1, analytical replicate 1; A2, analytical replicate 2. Relative product abundance quantified as described in Figure 3.1. Raw data in Supplementary Table S2.xlsx.

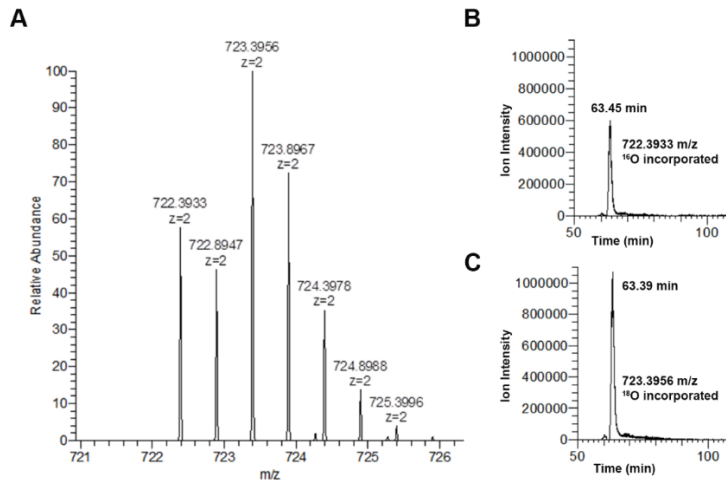


Figure 3.8. MS analysis of MCS10 substrate incubated with mIAP in H₂¹⁸O. (A) MS spectrum of doubly charged ($z=2$) reporter peptide displaying 50% more ¹⁸O incorporation than ¹⁶O. (B, C) The extracted ion current (XIC) for relative abundance of peptide (ALKDAQTNSSGGVVIA) with ¹⁶O incorporation (B) versus ¹⁸O incorporation (C) at the C-terminal of N-terminal product from enzymatic cleavage. Approximately 14.2% of peak at 723.3956 is due to two-¹³C isotope of the ¹⁶O-containing peptide.

The identified cleavage positions for mIAP reacted with MCS10 recapitulates the γ -secretase γ -site cut site leading to Alzheimer-associated A β 42 and A β 43 production but we did not detect even low-level background cleavage at Ile-Ala corresponding to the γ -secretase cleavage product A β 40 (153). Our results differ from a previous study indicating that the same mIAP ortholog cleaves epitope-tagged C100 to release predominantly A β 38 and A β 40, with only a minor product of A β 42 (53), but kinetics were not investigated in that system. Perhaps endoproteolysis of presenilin (168), which was not observed for our mIAP, confers the ability to robustly produce A β 40.

3.4.4 mIAP cleavage of the presenilin C100 substrate in the ‘ ϵ -site’ region

Prior to γ -site cleavage presenilin has been shown to cleave at the C100 ‘ ϵ -site’, which generates A β 48-49 (153). After unsuccessful attempts to generate a fusion substrate containing both sites (MBP- G₃₇GVVIATVIVITLVM-SUMO, MRS15) due to substrate aggregation (Figure 3.9), the isolated ϵ -site was probed by two fusion substrates shifted registers, MCSTV (MBP-T₄₃VIVITLVML-SUMO) and MCSGG (MBP-GG-V₄₄IVITLVM-SUMO) (Figure 3.10A), which includes the flexible Gly-Gly hinge thought to help position ϵ -site in the active site of γ -secretase (169). IAP cleaves both substrates (Figure 3.10B) LC-MS analyses converge on cut sites at three consecutive peptide bonds. The predominant cut site is Thr48-Leu49 (Figure 3.10C, D, Figure 3.7B, C, Supplementary Table S2.xlsx), which corresponds to presenilin-associated peptide A β 48. Whereas the Thr residue of MCS10 γ -site and MCSGG ϵ -site are in register (Figure 3.10C), comparison of MCSTV and MCSGG, which are offset, further supports a chemical preference for Thr over preference of relative position (Figure 3.10D).

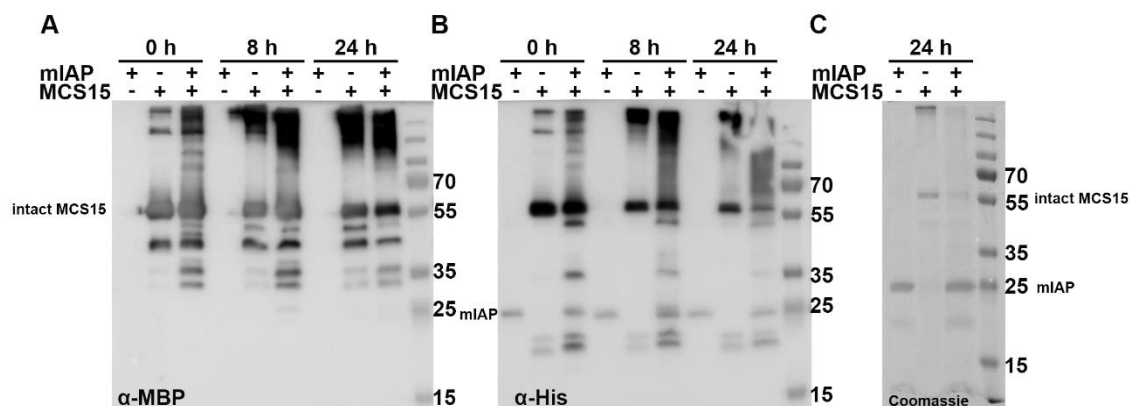


Figure 3.9. Gel assay using MCS15 substrate. (A) Western blot analysis using anti-MBP antibody. A 45 kDa band and high molecular weight species are present in MCS15 after purification even in the absence of IAP. With IAP addition, high molecular weight aggregates are seen immediately, which then grow over the course of 24 h at 37 °C. (B) Corresponding Western blot using anti-hexahistidine antibody detection recapitulates results in (A) but demonstrates the presence of the His-tagged mIAP (~25 kDa) (C) Coomassie-stained SDS-PAGE gel showing IAP and MCS15 at the end of 24 h gel assay.

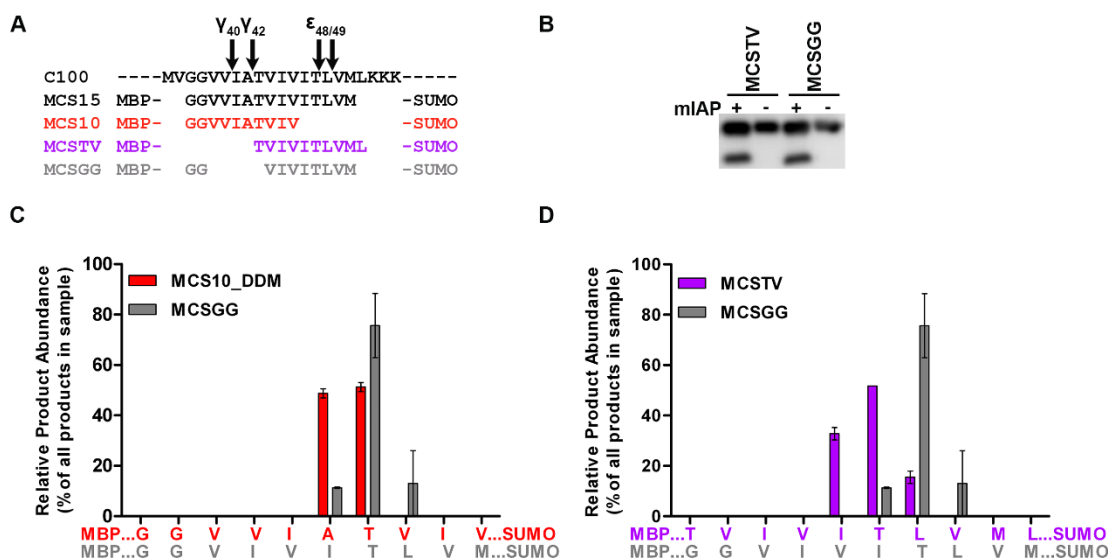


Figure 3.10. mIAP cleavage of C100 ε-site. (A) Overlay of substrates used in this study and relationship to C100 γ- and ε- cleavage sites of γ-secretase. (B) mIAP gel assay using MCSTV and MCSGG substrates. (C, D) MS analysis of MCS10, MCSGG and MCSTV cleavage sites by mIAP in DDM. Quantification and presentation as in Figure 3.1.

3.4.5 Probing substrate specificity by Thr-scanning within the MRS substrate

To further address the interplay between chemical and positional preferences for mIAP cleavage, we introduced Thr substitutions adjacent to His residues in MRS_{WT} (IHP₃FHL₆VIHT₁₀), namely, replacing P₃ or L₆ with Thr, and either retaining or removing the original His₉-Thr₁₀ cut site (MRS_{P3T}, MRS_{P3T/T10L}, MRS_{L6T}, MRS_{L6T/T10L}, Figure 3.11A and (56)). Since cleavage at His₅-Leu₆ was of low abundance in MRS_{WT}, we predicted that replacing Thr₁₀ in MRS_{WT} with Leu (MRS_{T10L}) would disfavor this position as a cleavage site, and serve as a control for positional preference (Figure 3.11A). mIAP cleaves all five MRS Thr-scanning mutants, including MRS_{T10L} where no H-T is present (Figure 3.11B-E, Figure 3.12, Supplementary Table S2.xlsx). The major cleavage position remains the same as for MRS_{WT}, and does not preferentially shift internally for MRS_{L6T}, MRS_{L6T/T10L} (Figure 3.11D), MRS_{P3T} or MRS_{P3T/T10L} (Figure 3.11E). Thus, in contrast with C100 ε-site cleavage, positional preference presides over chemical preferences in this sequence.

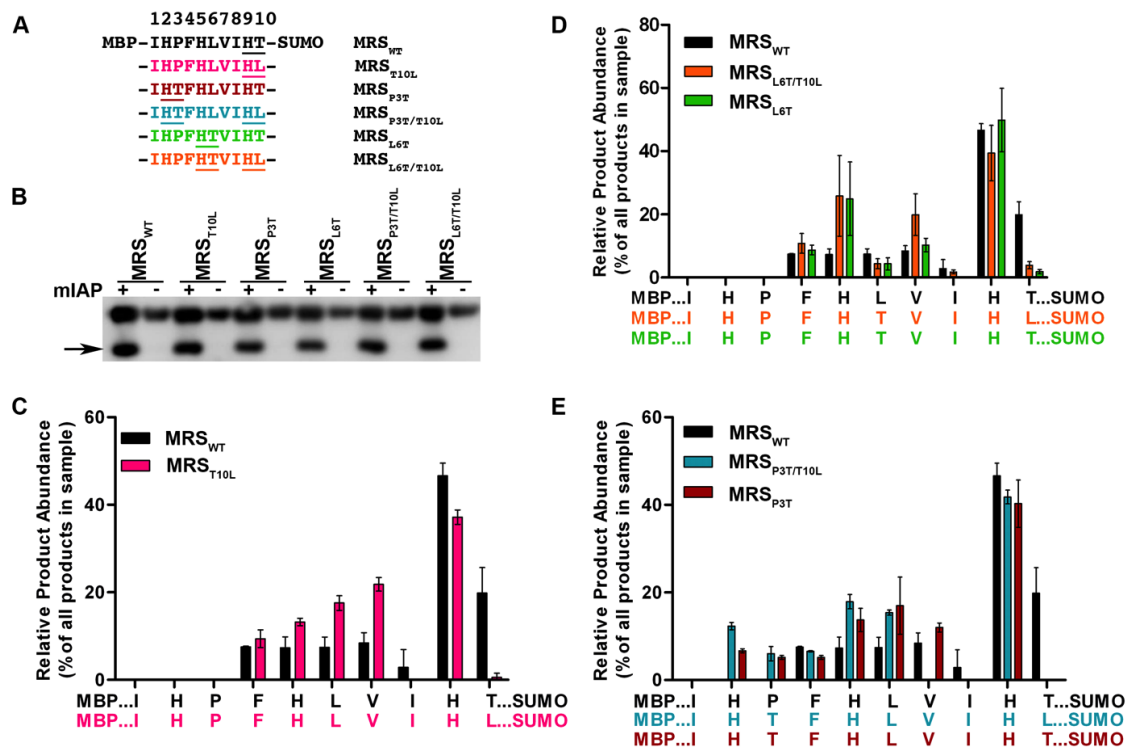


Figure 3.11. Probing substrate specificity of IAP using MRS Thr-scanning mutants. (A) Sequences generated for this study. (B) Gel cleavage assay using mIAP and MRS substrate variants, visualized by anti-MBP immunoblot. (C, D, E) Corresponding LC-MS analysis of reactions from (B) with quantification and presentation as in Figure 3.1. All LC-MS data for MRS substrate variants are presented in Supplementary Table S2.xlsx.

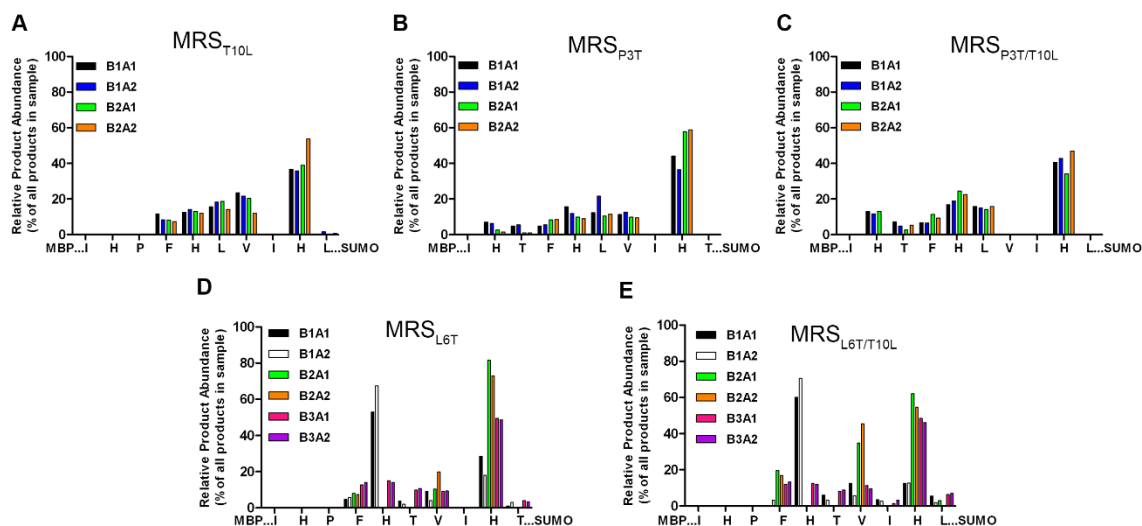


Figure 3.12. All LC-MS replicates for MRS mutant substrates cut by mIAP WT. (A) Cleavage profile of MRS_{T10L}. (B) Cleavage profile of MRS_{P3T}. (C) Cleavage profile of MRS_{P3T/T10L}. (D) Cleavage profile of MRS_{L6T}. (E) Cleavage profile of MRS_{L6T/T10L}. For each substrate, B1, biological replicate 1; B2, biological replicate 2; A1, analytical replicate 1; A2, analytical replicate 2. For MRS_{L6T/T10L} a third biological replicate (B3) was analyzed. Relative product abundance quantified as described in Figure 3.1. Raw data in Supplementary Table S2.xlsx.

3.5 Discussion

Intramembrane proteolysis must be highly regulated in the cell (2), yet contrary to intuition and knowledge of soluble proteases (119,120), data to date do not converge on recognition motifs for IPs within their TM substrate. Cleavage of non-physiological substrates has been demonstrated *in vitro* for S2P (90), IAPs (51-53), rhomboid (10,31,32), and γ -secretase (147). The biological significance of identified substrates is not always clear (170). Related, while helix-breaking residues within the TM segment were once thought to be important for cleavage (33,34,80,90), examples to the contrary appear in the literature (51,52). Confounding the puzzle for IAPs is an additional characteristic of processivity, or ratcheting, of cleavage; that is, IAPs cleave at multiple cut sites, and/or trim TM helices to smaller segments that can eventually be released from

the membrane (171-173). Systematic in vitro studies using purified enzymes, such as ours, can help clarify the physicochemical preferences of IAPs toward their substrates

Overall, our results point to faster kinetics and higher degree of specificity for IAP cleavage than previous studies using other methods. Across the substrates examined, a chemical preference for Thr at the scissile bond emerged, regardless of enzyme or substrate variant used. None of the residues targeted for mutagenesis within mIAP substantially altered cleavage profiles, even where kinetic parameters that might be correlated with specificity, such as K_m , were altered. Processivity was largely confined to residues adjacent to Thr on the substrate, and almost no background cleavage was seen for the biological mIAP substrate compared to the fortuitous renin substrate. Finally, bulk water is incorporated into the product of the hydrolysis reaction, confirming that the chemical reaction is similar to that of soluble aspartyl proteases (165), but how water enters the active site, and the extent to which each Asp functions in a manner similar to those in soluble aspartyl proteases, remain to be elucidated.

mIAP activity toward the presenilin substrate C100FRET is five-fold more efficient than the fortuitous Ren390FRET, reflected in faster V_{max} and lower K_m . There is no difference in cleavage profiles of MCS10 in bicelle or DDM indicating that the presentation of MCS10 to mIAP within DDM micelles and bicelles, and subsequent cleavage processes, are similar. Yet, the K_m is significantly more favorable for the reaction in bicelles, which contains CHAPSO, a cholesterol mimic. Cholesterol is a modulator of both membranes (174,175) and C100 catalysis (176-180). Indeed, C100 is partitioned well inside the lipid bilayer and specifically binds cholesterol (176).

Our study delineates properties and/or roles for specific residues on the enzyme beyond the catalytic Asp. The bulky phenyl ring, but not the hydroxyl group, in the YD₁₆₂ motif on TM helix 6 seems to be the important chemical property at this position. Y161 could orient the substrate in the active site, or it may stabilize residues from another TM helix in the conformation that supports substrate binding. Reinforcing the need for an aromatic residue, but not a proton donor/acceptor at this position, inspection of hundreds of presenilin-like proteins (PFAM PF01080 (181)) reveals that the WD motif is found an alternative to YD (not shown). Likewise, on TM helix 9, both A273P/G274A and L275F within the PAL motif exhibit slowed kinetics, but the K_m is better than for WT. In our pseudo first order reaction setup, the K_m reflects all of the binding events prior to catalysis, which is the slow step. Thus, since the substrate has higher affinity for the mutant enzyme than WT mIAP, impaired hydrolysis rates reflect a problem later in the process, for example, enabling a conformational change or properly that helps properly orient the substrate for catalysis.

The finding that mIAP exhibits a chemical preference for Thr at the scissile bond, when present, is consistent with numerous studies of γ -secretase and C100 describing γ - or ϵ -site cleavage, but the specificity with which mIAP cleaved at these sites containing a Thr across several substrates was unexpected. Thr exhibits average helical propensity (182-184), but intrahelical hydrogen bonds from the Thr side chain induces a more significant bend (185) and thus can displace remaining residues traversing the lipid membrane. Other residues capable of forming intrahelical hydrogen bonds include Ser and Cys (185). TM segments of SPP substrates (preprolactin, HLA-A*0301, and Hepatitis C virus), and γ -secretase substrates (ErbB4, Notch, p75, Delta, Jagged, and

STIM1 (74,76,136,186-190)), harbor Thr, Ser, and Cys residues, but most are not obviously in register with Thr residues in C100. A positional preference relative to the membrane competes for the chemical preference, as demonstrated by the observation that mIAP cleaved all Thr-scanning substrates at the same position as H-T in MRS_{WT}. Notably, in the case of the Notch, the position of cleavage reported previously for presenilin (191) is similar to that of T₄₈-L from C100 (176) with respect to the membrane bilayer (not shown). Our data point to a likelihood of different categories of IAP substrates governed by disparate physicochemical properties. This and other patterns regarding processivity will likely emerge upon further studies with more substrates and other IAP family members, ultimately leading to the ability to better target substrates selectively for therapeutic applications.

4 Chapter 4: Solution structure of an intramembrane aspartyl protease via small angle neutron scattering

4.1 Publication and author contributions

The data presented in Chapter 4 has been published in Biophysical Journal with a citation: Naing, S. H., Oliver, R. C., Weiss, K. L., Urban, V. S., and Lieberman, R. L. (2018) Solution Structure of an Intramembrane Aspartyl Protease via Small Angle Neutron Scattering. *Biophysical journal* **114**, 602-608. Membrane protein deuteration and growth was carried out by Kevin Weiss. The protonated and deuterated membrane protein were purified by Swe Htet Naing under the guidance of Dr. Raquel Lieberman. The small angle neutron scattering (SANS) data collection was performed by Swe Htet Naing, Ryan Oliver and Volker Urban. SANS data analysis and *ab initio* modelling was performed by Ryan Oliver and Volker Urban.

4.2 Introduction

Despite their broad biomedical reach, the structure of active IAPs including the number of subunits in the functional enzyme, has remained ambiguous. Membrane proteins require the presence of a mild detergent or other amphiphilic system to solubilize and stabilize a given membrane protein in an active conformation, which hinders structural characterization using standard analytical techniques used for soluble proteins such as size exclusion chromatography (SEC) or small angle X-ray scattering (SAXS). In the case of SEC, even coupled with multi-angle light scattering, molecular mass determination is only possible when the protein-detergent complex is well separated from empty micelles (192), and in SAXS, the signal from the membrane protein cannot be

isolated from that of the solubilizing agent (193). For IAPs, stoichiometries of one (57) through eight (194) subunits have been proposed. Prior to recent cryo-electron microscopy studies of γ -secretase that indicate a monomer (57), homodimer (145,195-197) was the predominant proposal. Fluorescence lifetime imaging microscopy was used to demonstrate that both SPP (145,196) and presenilins (195,196) are dimers. The lattice arrangement of the 3.8 Å resolution crystal structure of the microbial *M. marisnigri* IAP (WP_011844759.1, MmIAP) ortholog suggests either a dimer or tetramer (54).

To date, no IP has been structurally characterized using small angle neutron scattering (SANS), a method well-suited to study the solution properties of macromolecules and complex multicomponent assemblies like membrane proteins (198). For membrane protein-detergent complexes, the different scattering length densities (SLDs) of each component can be exploited so that only the membrane protein is visualized during the scattering experiment. Typically, the SLDs of the detergent and buffer/solvent are matched by judiciously adjusting the ratio of H₂O and D₂O in the solvent (199) and the signal from the membrane protein can be further enhanced by deuteration during cell growth (198).

Here we report the solution structure of deuterated MmIAP in *n*-dodecyl- β -D-maltopyranoside (DDM) determined by SANS. After deuterating MmIAP, the detergent was fully contrast matched using a specific ratio of hydrogenated and tail-deuterated detergent, and the scattering profile for MmIAP was recorded. The radius of gyration (R_g) calculated for MmIAP from SANS is smaller than the R_g calculated from the crystallographic MmIAP monomer, suggesting a more compact protein in DDM-containing solution. Our SANS study provides new insight into the solution oligomeric

state of MmIAP in detergent solution, as well as bolsters the utility of SANS to characterize other IPs and their membrane-bound substrates.

4.3 Methods

4.3.1 Expression and Purification of Protonated and Deuterated MmIAP

The plasmid containing MmIAP with a C-terminal hexahistidine tag was transformed into *E. coli* Rosetta 2 cells (Novagen, Madison, WI), grown, membrane isolated, and protein purified as described previously for enzyme activity assays(56). Modest modifications were made to scale purification to the higher protein requirement for SANS experiments. Membrane (~2 g) was solubilized in 160 mL of 50 mM Hepes (pH 7.5), 500 mM NaCl, 20 mM imidazole and 1% (w/v) DDM (Anatrace, Maumee, OH) by gentle rocking for 1 hr at 4 °C. Unsolubilized material was removed via ultracentrifugation at 162,000 x g for 45 min. The supernatant containing solubilized membranes was loaded onto a 1-mL HisTrap FF Crude Nickel affinity chromatography column (GE Healthcare, Chicago IL) pre-equilibrated with Buffer A (50 mM Hepes (pH 7.5), 500 mM NaCl, 20 mM imidazole, 0.1% DDM). Prior to elution of MmIAP, weakly bound impurities were removed with 5% Buffer B (50 mM Hepes (pH 7.5), 500 mM NaCl, 500 mM imidazole, 0.1% DDM). Elution of purified MmIAP was accomplished using a linear gradient by mixing Buffer A and 5-60% Buffer B. Elution fractions containing MmIAP were pooled and further purified on a HiPrep 16/60 Sephacryl-S300 (GE Healthcare) using gel filtration buffer (20 mM Hepes (pH 7.5), 250 mM NaCl, 0.05% DDM). Purity of protein was assessed by denaturing sodium dodecyl sulfate polyacrylamide gel electrophoresis (SDS-PAGE) analysis (12% polyacrylamide) stained

with Coomassie and concentration was measured using a NanoDrop spectrophotometer (ThermoScientific, Waltham, MA) ($\epsilon = 33,920 \text{ M}^{-1} \text{ cm}^{-1}$). Prior to SANS measurements, pure (protonated) MmIAP was buffer-exchanged using a 500 μL Amicon Ultra MWCO 50K concentrator (Millipore) into gel filtration buffer containing 22% D_2O (Acros Organic, Geel, Belgium).

Fed-batch cultivation, expression of deuterated MmIAP (*d*-MmIAP), and cell lysis was carried out in the Bio-Deuteration Laboratory at Oak Ridge National Lab (ORNL). Prior to *d*-MmIAP production, *E. coli* Rosetta 2 cells were first adapted to D_2O by transferring an individual colony of transformed cells from a Luria-Broth agar plate to 0.5% (w/v) glycerol minimal medium in H_2O and then subculturing into the same medium with an increasing D_2O content (25, 50, 75 and 90%), 100 $\mu\text{g/mL}$ carbenicillin, and 17 $\mu\text{g/mL}$ chloramphenicol. Once the cells were growing in 90% D_2O medium, a 400 ml preculture was used to inoculate 3.6 L of fresh 90% D_2O medium in a benchtop BioFlo 310 bioreactor system (Eppendorf, Hauppauge, NY) equipped with a 5.5 L working volume vessel. At the outset of the experiment, the temperature was maintained at 30 °C, aeration was maintained throughout at 4 L/min, and agitation was varied from 200 – 800 rpm to maintain dissolved oxygen above a set point of 30% saturation. A solution of 10% (w/v) NaOH in 90% D_2O was added on demand to maintain a $\text{pD} > 7.3$. When the dissolved oxygen spike occurred upon depletion of the 0.5% (w/v) glycerol, a feeding of a solution consisting of 10% (w/v) glycerol and 0.2% MgSO_4 in 90% D_2O was initiated. After approximately 7 hours of feeding, the temperature set point was reduced to 18 °C and *d*-MmIAP expression was induced by adding 1 mM isopropyl- β -D-1-thiogalactopyranoside. Upon harvesting via centrifugation at 6,000 $\times g$ for 45 min, cell

paste containing *d*-MmIAP (~145 g wet cell weight) was suspended (0.1g/mL) in 50 mM Hepes (pH 7.5), 200 mM NaCl containing EDTA-Free SIGMAFAST™ Protease Inhibitor Cocktail Tablets (Sigma Aldrich, St. Louis, MO) and lysed at 15,000 psi via three passages through an EmulsiFlex-C3 homogenizer that was fitted with a chilled heat exchanger (Avestin, Ottawa, ON) and stationed in a 6 °C cold room. Following lysis, cellular debris was removed by centrifugation at 5,000 x *g* for 15 min four times. The supernatant (~1.8 L) was then subjected to ultracentrifugation at 162,000 x *g* for 30 min. The pelleted membrane fraction was washed by resuspension in a Dounce homogenizer and the membrane fraction was again isolated by ultracentrifugation as above. *d*-MmIAP-containing membranes (~22 g) were solubilized by gentle rocking for 0.5 hr at 4 °C in 200 mL of a solution containing 50 mM Hepes (pH 7.5), 500 mM NaCl, 20 mM imidazole, and 4% (w/v) DDM. The membrane resuspension was subjected to ultracentrifugation as above to remove insoluble material.

The supernatant containing the solubilized membrane was purified using the protocol for MmIAP described above except for the following additional steps to maximize yield of purified enzyme. Namely, the flow through fractions from the first nickel affinity chromatography run were diluted in Buffer A lacking detergent to a final concentration of 2% DDM, and purified on the column again. A third round of nickel affinity chromatography was then performed on the flow through, from the second column, which was diluted with Buffer A lacking detergent to 1% DDM. Elution fractions from the three nickel affinity purification runs were pooled, concentrated to two ~900 µL aliquots using a 15 mL Amicon Ultra MWCO 50K concentrator (Millipore), and each loaded onto a HiPrep 16/60 Sephacryl-S300 (GE Healthcare) pre-equilibrated as for

MmIAP above. Fractions containing purified *d*-MmIAP as judged by SDS-PAGE were pooled and a third Sephacryl-S300 column was used to further polish the sample. In a final step, purified *d*-MmIAP was loaded onto a Superose-12 10/300 GL (GE Healthcare) column equilibrated with 20 mM Hepes (pH 7.5), 250 mM NaCl, 48.5% D₂O and 0.05% total DDM, of which 44% (w/v) is tail-deuterated d₂₅-DDM (Anatrace) (Figure 4.1). The final yield was ~ 1 mg of *d*-MmIAP, all of which was used in the SANS experiment.

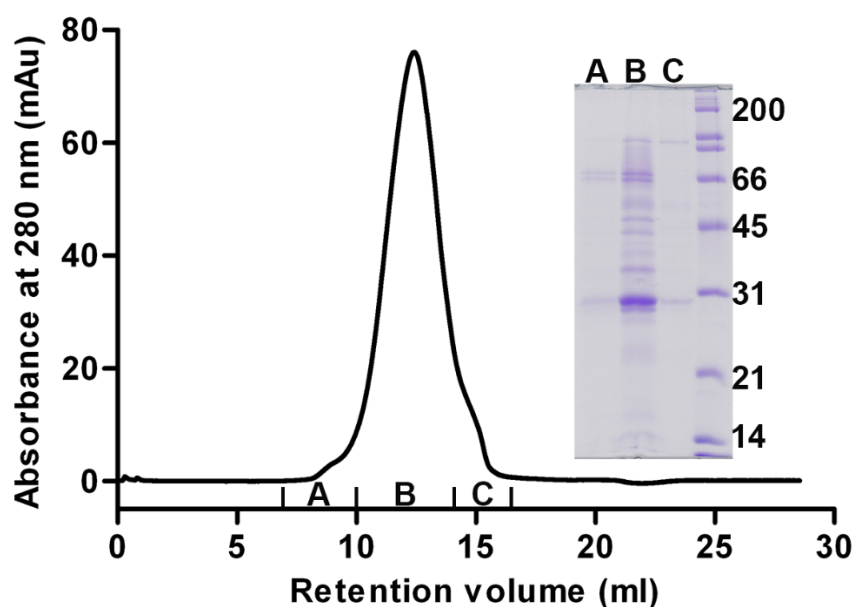


Figure 4.1. *d*-MmIAP purification. Final size exclusion chromatogram (Superose-12 10/300 GL column) for *d*-MmIAP equilibrated with 20 mM Hepes (pH 7.5), 250 mM NaCl, 48.5% D₂O and 0.05% total DDM, of which 44% (w/v) is tail-deuterated d₂₅-DDM (Anatrace). Inset: SDS-PAGE analysis of pooled fractions labeled A, B, C. Region labelled “B” was used in the SANS experiment.

4.3.2 Small-Angle Neutron Scattering Data Collection

SANS data were collected at the Bio-SANS beam line CG-3 of the High-Flux Isotope Reactor at ORNL using a single instrument configuration with 7-meter sample-

to-detector distance. Data were collected at 12 °C using 1mm quartz cells and neutron wavelength of $6 \text{ \AA} \pm 14\%$. The range of momentum transfer Q used was $0.007 < Q < 0.7 \text{ \AA}^{-1}$ ($Q = 4\pi \cdot \sin(\theta)/\lambda$, where 2θ is the scattering angle and λ is the neutron wavelength). Additional descriptions of the instrument and setup have been previously published (200-202). The recorded scattering data were circularly averaged, and reduced to 1D scattering profiles using MantidPlot software (203). Calibration of the SANS data to an absolute scale was performed by measuring a porous silica standard with known intensity at zero angle (extrapolated from a Debye-Bueche plot). Blank buffers containing the same % D_2O as the samples were similarly measured and subtracted from the sample scattering for background correction using a toolkit developed by Dr. Ken Littrell (ORNL) for IgorPro. Subsequent data analysis and modelling of scattering profiles were facilitated with the ATSAS 2.6.1 program suite (EMBL – Hamburg) (156).

4.3.3 SANS Data Analysis and Modelling

An initial estimation of the R_g and forward scattering intensity (I_0) was performed using PRIMUS (204). Core-shell ellipsoid shape models were fit to the scattering data using SasView v4.1 (205). Comparisons of SANS data for *d*-MmIAP to structures of MmIAP and presenilin in the Protein Data Bank (PDB) were conducted with CRYSON (206). For the simulation conditions, a deuteration fraction of 0.75 was used for the protein chain with a D_2O fraction in the solvent of 0.49 to mimic the experimental contrast conditions.

ATSAS software tools were used for further modelling and interpretation of the structural SANS information for *d*-MmIAP in solution with contrast-matched detergent. The first step of this process employed GNOM (207) to generate a pair-distance

distribution function $P(r)$, which described the relative interatomic distances within the scattering particle. Scattering data over the range $0.0106 < Q < 0.585 \text{ \AA}^{-1}$ were used for the real space transformation and subsequent modelling, and provided a $P(r)$ curve with a single peak and D_{max} of 46 \AA . The R_g from the real space transformation was $16.7 \pm 0.2 \text{ \AA}$ with an I_0 of $0.610 \pm 0.001 \text{ cm}^{-1}$. The GNOM output was used for *ab initio* molecular shape generation with DAMMIF and DAMMIN (208,209). The $P(r)$ data were used as an input for fast DAMMIF modelling to create seventeen initial dummy atom models (DAMs). These initial DAMs were aligned and averaged using DAMAVER (210), and one outlier from the seventeen was discarded based on normalized spatial discrepancy (NSD) values as its NSD value exceeded 2 standard deviations from the cluster mean (cluster NSD: 0.708 ± 0.018 , outlier NSD: 0.749). After averaging in DAMAVER, the ‘damstart’ (fixed-core) model was used for refinement with DAMMIN, yielding a single refined SANS envelope. Superimpositions of the SANS envelope with crystal structures were performed using SUPCOMB (211), which minimizes NSD to find the best alignment of the two models.

4.4 Results

4.4.1 SANS Analysis of *d*-MmIAP

SAXS measurements showed, as expected, strong scattering signal from DDM micelles that was similar with and without MmIAP, and initial attempts of SANS experiments using non-deuterated MmIAP, DDM, and D_2O/H_2O were unsuccessful in isolating a signal for MmIAP unperturbed by scattering contributions from the surfactant (Figure 4.2). Therefore, *d*-MmIAP was expressed and purified (Figure 4.1) immediately prior to data collection, using established methods yielding active enzyme (56). Based on

other studies (212), the average deuteration level under growth conditions is 70-75%. Scattering from the *d*-MmIAP protein-detergent complex produced a stronger signal overall as a result of the increased protein contrast relative to the solvent, but contributions from the detergent were still present in the net scattering profile. These results are observed in a comparison of the MmIAP-DDM complex versus *d*-MmIAP-DDM in the same DDM contrast-matched conditions (Figure 4.3).

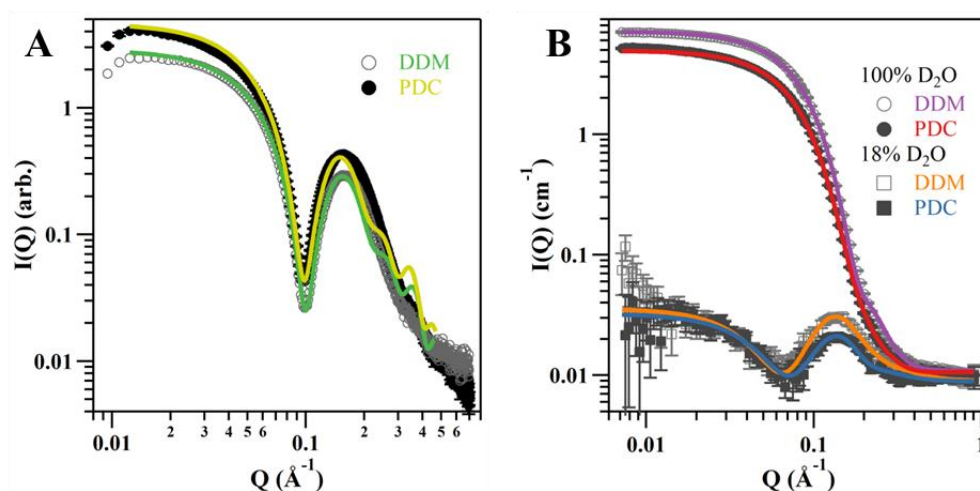


Figure 4.2. Preliminary (A) SAXS and (B) SANS data collected for solutions of micelles (DDM – unfilled markers) and the protein-detergent complex (PDC – filled markers). Strong similarity was observed in scattering profile shapes between these two conditions at all measured contrasts. Core-shell ellipsoid model fits are shown by the solid lines, colored according to the legend.

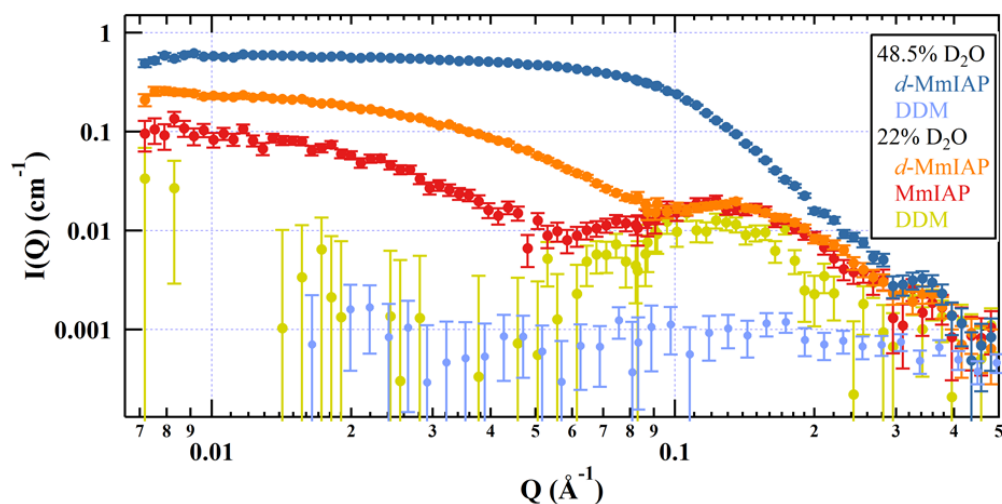


Figure 4.3. SANS contrast match point measurements for DDM micelles, MmIAP with DDM, *d*-MmIAP with DDM (22% D₂O), and *d*-MmIAP with DDM / d25-DDM mixed micelles (48.5% D₂O). Light blue data points reproduced from (213).

To achieve true extinction of any scattering contribution from DDM, a more refined approach was required. The individual contrast match points of hydrophobic DDM alkyl tails and hydrophilic maltoside head groups are 2% and 48.5% D₂O, respectively, which is very far from the overall contrast match point (CMP) of 22% D₂O. This, together with the similar size of both moieties and their distinctive location in a micelle core and shell, produces significant residual scattering, even at 22% D₂O (Figure 4.3, yellow data points, reproduced from (213)). This problem can be resolved by raising the CMP of the DDM micelle core to 48.5% D₂O to match the shell by precisely blending 44% (w/v) tail-deuterated DDM (d25-DDM) with regular DDM (213). Under these complete matching conditions, scattering features from DDM micelles were rendered negligible (Figure 4.3), which is readily apparent by the absence of a secondary maximum in the SANS profile.

The combination of deuterated protein and completely contrast-matched mixed micelles yielded an interpretable SANS profile for the enzyme without interference from buffer and detergent components (Figure 4.3 and Figure 4.4A). Guinier analysis was performed on the low-Q scattering data defined by an upper limit of $Q \cdot R_g < 1.3$, and provided estimates of I_0 and R_g (Figure 4.4B). The measured R_g (16.1 ± 0.5 Å), and a Kratky plot illustrating the folded nature of the scattering object (Figure 4.4C), suggests that MmIAP is most likely monomeric with a compact, globular shape in detergent solution (214). The forward scattering intensity determined from the Guinier fit was 0.60 ± 0.01 cm⁻¹. An indirect Fourier transform of the scattering data provided a plot describing the pair-distance distribution $P(r)$ of intramolecular distances within the particle, constrained by a maximum particle dimension of 46 Å (Figure 4.4D). Molecular weight was estimated from the DAMMIN model and by the method described by Rambo and Tainer (215) (see Figure 4.5 for details). A summary of the physical parameters extracted from the SANS data in comparison to similar values obtained from the final SANS envelope and the PDB model (4HYC, chain A) is presented in Table 4.1. The combination of these results from SANS suggest a monomeric MmIAP size and shape without the formation of higher order oligomers in micellar solution.

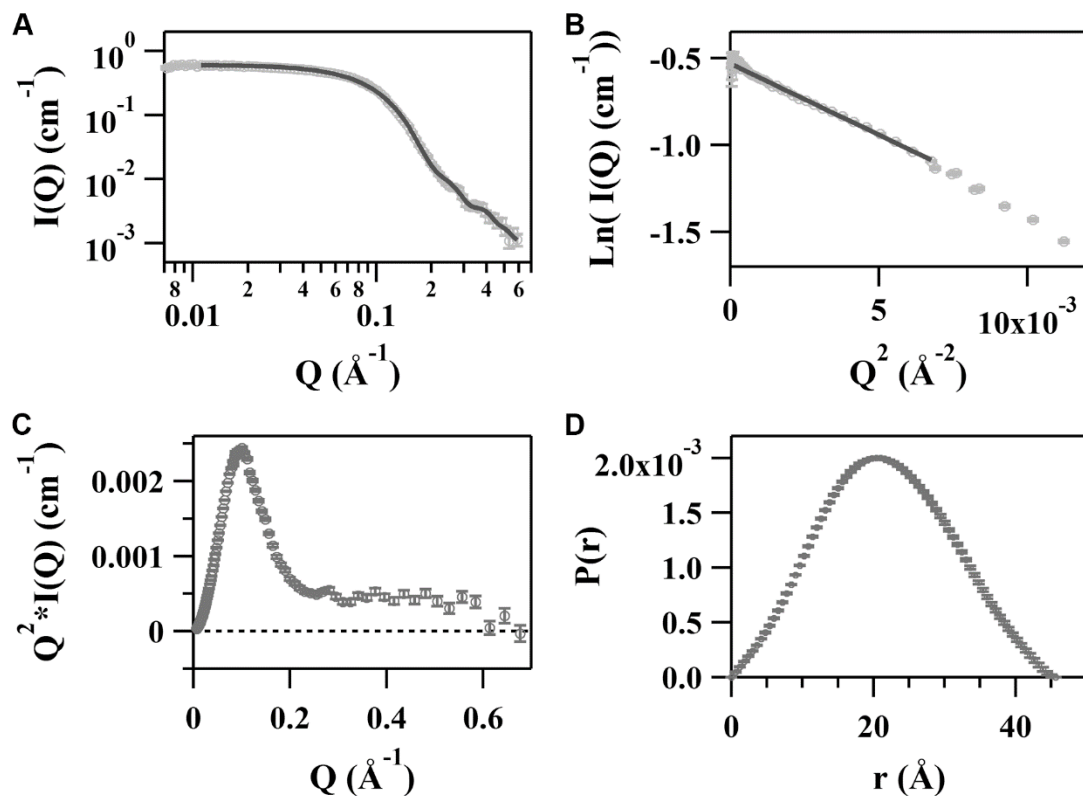


Figure 4.4. SANS data obtained for *d*-MmIAP with contrast-matched DDM / d25-DDM mixed micelles (48.5% D₂O). (A) A plot of the scattered intensity versus Q , a function of the scattering angle, with GNOM fit shown in solid line; (B) Guinier plot of the low angle scattering data with a linear fit in the Guinier region shown in solid line; (C) A Kratky plot of the same scattering data demonstrating the compact, folded shape of the particle; and (D) A pair-distance distribution function $P(r)$ obtained from GNOM representing the distribution of real space distances between scattering centers within the particle.

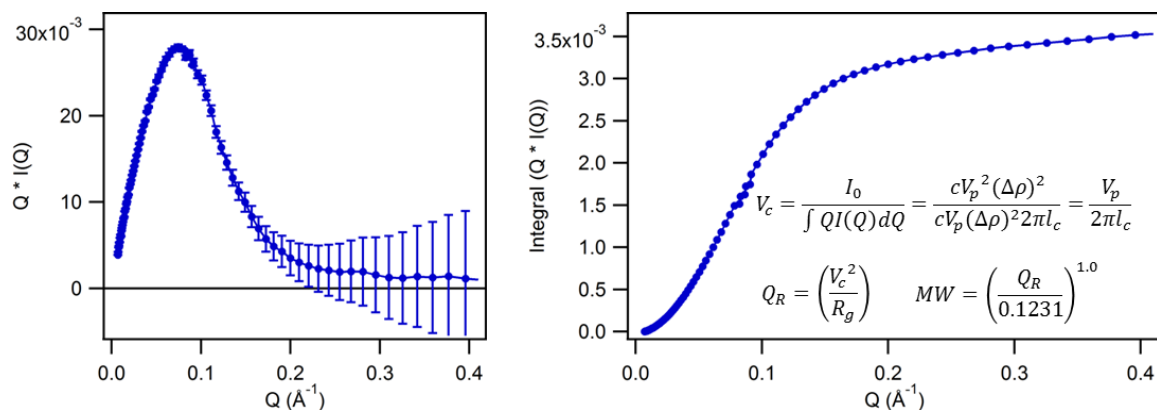


Figure 4.5. Determination of protein molecular weight from the SAS invariant Q_R . Data are replotted first as a modified Kratky plot ($Q^*I(Q)$ vs Q), where flexible and non-flexible proteins, and even unfolded proteins, should converge with zero intensity at high Q . This plot is then integrated to an upper limit defined by the scattering signal decay or plateau of integration ($Q_{max} \approx 0.25$ was used here). The ratio of I_0 to this integrated value determines the volume-of-correlation for the particle to be used in estimating the molecular weight of the particle.

Table 4.1. Summary of physical parameters from the SANS data, reconstructed DAM, and a related PDB entry (4HYC:A).

Radius of Gyration (Å)				D_{max} (Å)			Volume (Å ³)		
Guinier	GNOM	DAM	PDB	GNOM	DAM	PDB	SANS	DAM	PDB
16.1	16.7	16.7	19.4	46.0	47.7	72.9	21,030	20,590	31,258
± 0.5	± 0.2								

4.4.2 Particle molecular volume estimates

The SANS data were placed on absolute intensity scale, and an independent estimation of particle size from the forward scattering intensity (I_0) is therefore in principle possible. The sample molecular weight (MW) can be determined using the calibrated I_0 value, sample concentration (c), and particle contrast ($\Delta\rho$) according to the

following equation:

$$MW = \frac{I_0 \cdot N_A}{c(\Delta\rho \cdot v)^2}$$

where N_A is Avogadro's number, and v is the partial specific volume of the protein (216). However, as Tainer et al. (215) have pointed out, this approach is difficult, given the limits in accuracy of known particle concentration and other factors. SANS experiments also have the added challenge of accurately assessing the particle's neutron contrast, particularly when the particle is a protein expressed in deuterated growth media.

An estimate of the protein contrast was made by inferring the level of deuterium incorporation at non-exchangeable positions in the protein from published empirical evidence. Previous studies suggest that a protein expressed in growth media containing ~90% D₂O yields a protein with 70-75% incorporation of deuterium at the non-exchangeable positions of the protein (212). Particle concentration was estimated to be $2.52 \pm 0.38 \text{ mg} \cdot \text{mL}^{-1}$ by NanoDrop spectrophotometer (ThermoScientific) measurements of the absorbance at 280 nm using a calculated molar extinction coefficient of $33,920 \text{ M}^{-1} \text{ cm}^{-1}$ from the IAP primary sequence. Although no absorbance in this region was observed for protein-free detergent micelle solutions, we cannot completely exclude the possibility that the suspension of membrane protein in detergent micelles interferes with this concentration estimate. From the apparent intensity of our gel electrophoresis data, we place an upper boundary of the concentration at $5 \text{ mg} \cdot \text{mL}^{-1}$. This limit, in conjunction with the uncertainties in particle contrast, yields a total range of uncertainty in molecular weight that is too broad to identify the oligomeric state of MmIAP from I_0 with any useful accuracy.

Conversely, we obtained estimates for the particle volume from two intensity scale independent methods: The DAMMIN model yields a total excluded particle volume of 20,590 Å³ in fair agreement with the calculated volume of monomeric MmIAP (31,258 Å³ from PDB 4HYC, chain A, using VADAR v1.8, Univ. of Alberta, or 40,778 Å³ from primary sequence using MULCh, University of Sydney). The concentration-independent approach described by Rambo and Tainer to determine molecular weight was also employed (215), using the SAS invariant Q_R and the following relationship for proteins:

$$Mass = \left(\frac{Q_R}{0.1231} \right)^{1.0}$$

where $Q_R = V_c^2 \cdot R_g^{-1}$, and V_c is the volume-of-correlation. Additional details and plots used to determine the volume-of-correlation from the integrated area of $Q^*I(Q)$ are provided in Figure 4.5. This approach yields a molecular weight of 16.4 kDa, smaller than a single molecule of MmIAP. Both estimates support the conclusion that MmIAP in solution is a rather small scattering object, a result that is consistent with the hypothesis of MmIAP being monomeric rather than oligomeric.

4.4.3 Comparison to Crystal Structure and *ab initio* Modelling

SANS profiles were calculated from available structures for pertinent enzymes (chain A from MmIAP PDB codes 4HYC, 4HYD, 4HYG, and 4Y6K, and chain B, presenilin from γ -secretase PDB codes 5A63, 5FN2, 5FN3, 5FN4, and 5FN5). The four MmIAP crystal structures are ~3.3-3.9 Å resolution, represent three different space groups, different bound states (apo and inhibited), and are similar to each other with root mean square deviation (r.m.s.d.) of ~0.5-0.8 Å. The five presenilin structures solved by cryo-electron microscopy are 4.0-4.3 Å resolution, and represent four apo states, as well

as one that is bound to an inhibitor. Presenilin shares just 15% identity with MmIAP yet r.m.s.d.s for the two different structures are just $\sim 2.5\text{-}3\text{ \AA}$. CRYSON fits to the experimental data from representative members of each PDB group are shown in Figure 4.6A. The simulated scattering profiles for structural monomers are in relative agreement with the measured scattering profile of *d*-MmIAP in contrast-matched, mixed d25-DDM / DDM micelles (Figure 4.6). Each structure appears somewhat larger than that measured in solution, denoted by the decrease in scattered intensity from the plateau at lower values of Q for the simulated SANS data compared to the measured data, but are much closer to the data than a hypothetical *d*-MmIAP dimer and tetramer (Figure 4.6A). The average R_g from the structure (19.4 \AA , Table 4.1) is also $\sim 3.4\text{ \AA}$ larger than the R_g determined from a Guinier fit to the SANS data ($16.1 \pm 0.5\text{ \AA}$).

Ab initio modeling from *d*-MmIAP SANS data with contrast-matched detergent recapitulates the overall agreement with the available structures. A representative scattering profile from the remaining DAMMIF models demonstrates strong agreement with the experimental data (Figure 4.6A) and the SANS profile of the DAMMIN-refined envelope was indistinguishable from this representative trace. The SANS envelope shown here has a protrusion that is consistent with the predicted position of the long helix 6, which contains the C-terminal GxGD motif, and a well leading to the general vicinity of the catalytic aspartates (Figure 4.6B). We note however, that not all sixteen DAMs show exactly these features in the same location; thus, the fit shown here agrees with the SANS data but this envelope is not the only possible model at this level of detail. The poorest fit is for helix 4, half of which appears to protrude beyond the SANS envelope in

accordance with the larger R_g and D_{max} values (Table 4.1) and calculated scattering intensity at low Q values.

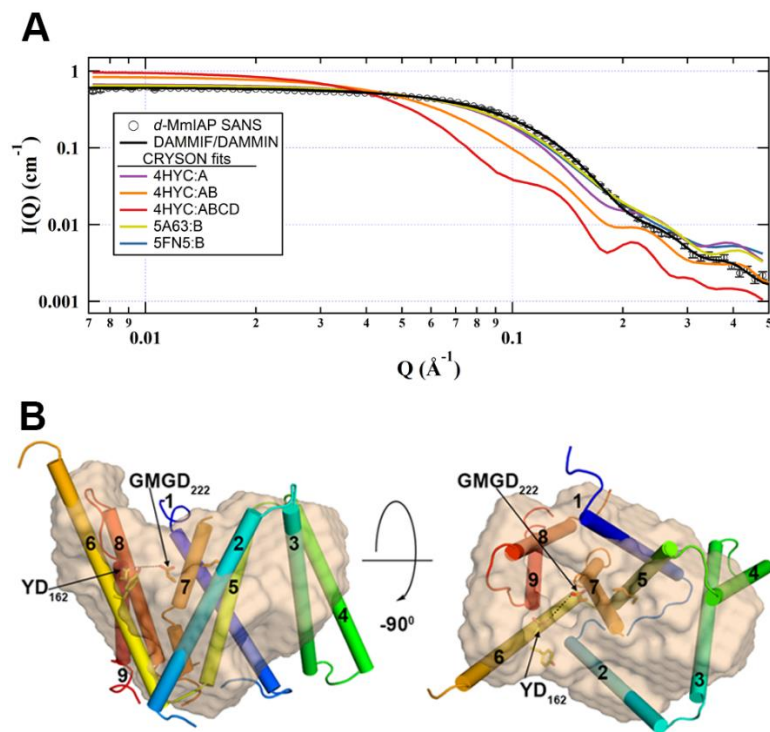


Figure 4.6. CRYSON results and comparison to SANS data. (A) Simulated SANS profiles from CRYSON for representative PDB entries related to intramembrane aspartyl proteases. Scattering from a MmIAP dimer and tetramer were also simulated using chains A and B from 4HYC, or chains A-D from 4HYC, respectively, demonstrating that higher order oligomers are not consistent with the observed scattering. (B) The *ab initio* model was also overlaid with chain A from 4HYC to provide a 3D structural comparison.

4.5 Discussion

Despite the increasing number of available membrane protein structures in the protein data bank determined by X-ray crystallography, nuclear magnetic resonance spectroscopy, and cryo-electron microscopy, the percentage remains very low compared to the total membrane-bound proteome, and determining the oligomerization state of such

proteins in solution remains a major challenge (217-219). Here we used SANS to determine the molecular envelope and oligomerization state of an IAP in solution. Our strategy had three major components: (1) deuterating MmIAP during cell growth to increase the SANS signal from the enzyme (2) utilizing 44% d25-DDM to match the CMP of the hydrophobic tail core with that of the head group of the DDM micelle and (3) contrast matching the overall DDM micelle with 48.5% D₂O to leave only scattering from *d*-MmIAP.

The process of contrast matching to detect only the signal from the membrane protein is inherently challenging (220); micelle-micelle interaction or protein-protein interactions can corrupt low-Q data, and the residual signal from incompletely matched lipid head and tail components limit data interpretation to gross structural changes under defined experimental conditions. Typically, SANS studies of membrane proteins employ the average contrast match point for the solubilizing agent. For example Bu et al. (221) overall contrast-matched the small unilamellar vesicles to detect a change in the oligomeric state of SecA upon nucleotide binding, and Zimmer et al. (222) used the average contrast match for DDM of 22% D₂O to detect differences between truncated and full-length potassium channel KcsA solubilized in DDM under different pH conditions. With our improved understanding of the detergent contributions to neutron scattering (213), reinspection of numerous SANS studies that utilize a similar strategy (150,222-226) suggests that the scattering profile exhibits contributions due to incompletely matched surfactant or lipid components. Thus, our recent efforts have been aimed at improving the contrast matching protocol by matching the hydrophobic tail of the detergent to its head group prior to contrast matching the overall micelle with D₂O.

One prior study used an analogous strategy with sodium dodecyl sulfate (227), but the current study is the first such application to study a membrane enzyme solubilized in DDM, a more mild detergent with a larger headgroup (218). The theoretical basis for the approach with DDM was recently reported (213), and resulted in a strong interpretable signal free of contribution from the detergent.

The *d*-MmIAP *ab initio* model in solution is consistent with an approximately spherical monomeric protein, not a dimer or higher ordered species suggested in earlier biochemical experiments for SPP and other human IAP family members. Interestingly, the experimentally determined R_g (16.1 ± 0.5 Å) from SANS is somewhat smaller than the calculated R_g (19.4 Å) from a monomer chain of crystalline MmIAP, indicating a more compact structure is present in solution. This finding agrees with the observation that crystallized MmIAP was trapped in an inactive conformation, with the two aspartates too far apart for catalysis. Detergent identity and concentration are well known to affect crystallization properties (91,228). In the case of the MmIAP crystal structure, perhaps the limited proteolytic digestion of the enzyme or mutations introduced to enhance crystallizability (54), led to a less compact bundle of transmembrane helices.

Alternatively, the dynamic detergent micelles present during crystallization might affect the lattice (229-231), as would be expected for an α -helical membrane protein with predominantly membrane immersed helices (232). Our sample for SANS was prepared using the same methods as for our enzymatic study where it is active for nearly a week after purification (56), suggesting our SANS envelope reflects that of an active enzyme in detergent solution, but whether the protein remains a monomer in the presence of substrate is an open question for further study.

5 Chapter 5: Future directions

5.1 Introduction

Robust, fast and high throughput FRET-based continuous assay was developed to study the kinetics of IAP. High resolution LC-MS/MS study was also developed to identify cleavage sites of substrates. Small-angle neutron scattering study of IAP yielded a solution structure of IAP free from detergent micelles signal. Techniques, that we developed, contribute to the better understanding of physiochemical properties governing IAP proteolysis. However, there are several major outstanding questions that remain to be answered: how does substrate enter active site, how does IAP discriminate natural substrate from non-substrate etc. Substrate repertoire will be extended to better understand the substrate specificity of IAP. In addition, how familial Alzheimer's disease-linked mutations found on C100 substrate affect IAP proteolysis will be identified. Moreover, using cross-linking technique and SANS, interaction between substrate, enzyme and lipid environment will be elucidated

5.2 Evaluate quantitatively the effects of FAD mutations within the C100 substrate on IAP kinetics and cleavage preferences

In addition to heritable mutations in presenilin leading to Alzheimer's disease, are mutations in amyloid precursor protein (www.alzforum.org/mutations). The FAD-linked mutations within the C100 substrate sequence (e.g. T43I, T43A, I45T) affect the catalytic efficiency of γ -secretase and increase the ratio of A β 42/40, a poor prognosticator for Alzheimer disease pathogenesis (233). However, how these C100 substrate mutations influence the cleavage specificity of γ -secretase remains elusive.

My thesis work demonstrated that our IAP ortholog cleaves at two consecutive γ -sites, A₄₂-T₄₃-V₄₄, similar to γ -secretase production of A β ₄₂-A β ₄₃. Thus, the methodology developed in this thesis could be applied to decode the effects of these mutations on kinetics and cleavage site preferences. Since the chemical preference towards Thr is removed in T43I and T43A mutants, I hypothesize these will not be cleaved by our IAP whereas with I45T, I hypothesize a new cleavage sites at V₄₄-T₄₅-V₄₆. Of interest is whether the original γ -site cleavage or the site adjacent to T₄₅ will be the predominant, tying into positional preferences for the IAP-substrate pair.

5.3 Clarify sequence preferences for IAP cleavage by expanding the substrate repertoire tested using assays developed in this thesis

Among 90 substrates for γ -secretase and 30 substrates for SPP, some are not biological substrates and there is no consensus motif among substrates (5,59). The factors influencing the substrate recognition and specificity of IAP remain elusive. Results of this thesis demonstrate that the substrate specificity of IAP is influenced by chemical preference for Thr as well as positional preference. By screening additional biological substrates of presenilin and SPP, substrate and positional preferences of IAP will be better defined. The selected substrates (Table 5.1) include proteins that play essential role in a number of biological processes and are related to human diseases (5,59). To assess cleavage site preferences, fusion protein substrates analogous to MRS and MCS will be generated with the transmembrane segments in Table 5.1 and then subjected to IAP cleavage and LC-MS analysis. I hypothesize that IAP will cleave some substrates (preprolactin, HLA-A, hepatitis C virus, Swine Fever Virus and ErbB4) preferentially at a polar residue, Thr or Ser, analogous to MRS and MCS. Some substrates (Notch, p75,

Delta, Jagged) do not have these residues, however. Cysteine might play a surrogate role for threonine at the scissile bond, but these may instead be forming dimers (234). In this case, I hypothesize that positional preferences will guide the predominant cleavage site.

After cleavage sites are analyzed, FRET-based substrates will be synthesized where a fluorophore/quencher pair (e.g. EDANS/DABCYL) will be attached on the termini of 10 amino acid peptide substrate containing the identified cut site. Kinetic parameters associated with each substrate cleavage by IAP will be measured and compared. Since a significant improvement in catalytic efficiency was observed upon using C100FRET compared to non-natural Ren390FRET substrate, we hypothesize there will be a higher catalytic efficiency with the natural substrates of presenilin and SPP even when paired with a microbial ortholog.

Table 5.1. Selected substrates where proposed cut site is underlined

Substrate	Sequence
Proposed chemical preference at cut site	
Preprolactin	MDSKGSSQKGSRLLLL <u>V</u> SNLLLCQGVV
HLA-A*0301	MAVMAPRTL ¹ LLLL <u>S</u> GALALTQTWA
Hepatitis C virus	PGCSFSIFLLALL <u>S</u> CLTVPASA
Swine Fev. virus	RKKLEKALLAWAVIT <u>I</u> LLYQPVAA
ErbB4	TPLIAAGVIGGLFILVIVGL <u>T</u> FAVYVRRK
Proposed positional preference at cut site	
Notch	AQLHFM ¹ YVAAAFVLLFFVG <u>C</u> GVLLSRKRR
P75	LIPVY <u>C</u> SILAAVVVGLVAYIAF
Delta	MLLLGVA ¹ AVVVC <u>V</u>
Jagged	LWLACVVLC <u>V</u> WWT

5.4 Characterize the substrate-enzyme complex

The current available crystal and electron microscopy structures of IAPs are in an active conformation, providing little insight into how substrates enter into the hydrophilic active site from the hydrophobic lipid membrane. The predominant proposal for substrate entry involves TM6 containing the YD motif and TM9, containing the presenilin PAL motif. It is possible to characterize the substrate-enzyme interaction and conformational changes of substrate and enzyme that occur upon binding using SANS. The ability of the SANS method to mask one component by matching its scattering length density with the background highlights the key component of interest in a macromolecular complex. In our case, substrate and enzyme are two components whose conformational changes will be monitored while the other is made invisible by matching with the background. The detergent micelles will be rendered invisible with the help of tail-deuterated DDM and D₂O as described in Chapter 4.

First, molecular envelope of IAP with and without substrate peptide will be compared to observe the conformation changes of IAP upon peptide binding. IAP will be deuterated to increase the contrast between the IAP and the background containing the SANS-invisible small substrate peptide. The final *ab initio* model of apo and substrate-bound IAP, processed from initial neutron scattering data, will be compared to probe the structural changes of IAP that occur upon substrate binding. In order to trap IAP in a substrate-bound state, a catalytic inactive mutant (D162A/N, D220A/N), which has been found to be able to bind to substrate peptide yet fail to cleave the peptide (56), should be used. Alternatively, non-hydrolyzable substrate analogs could also be used with WT IAP in this experiment.

Second, the molecular envelope of the substrate with and without IAP will be compared. In order to determine what orientation substrate takes to enter the active site of IAP, the fusion substrate, MCS (or other fusion protein substrate of interest) instead of the small peptide, will be used so that the substrate is visible. The SANS experiment will be carried out on the IAP/MCS complex in which both proteins are deuterated, providing the molecular envelope for the complex as one unit. Protonated IAP, which can be rendered invisible by matching with the background, will be used in complex with deuterated MRS to visualize only the substrate in the enzyme-bound state. The difference in size of MBP (~45 kDa) and SUMO (~12 kDa), that are flanking the desired substrate region on MRS substrate, will allow us to easily identify their position respective to IAP, thereby determining the orientation of substrate in the active site of IAP. It may also be possible to deduce the route of substrate entry on the IAP. The IAP-bound state of the fusion substrates will be compared to the unbound fusion substrates evaluated by SAXS, using methods for MRS in Chapter 3, to probe evaluate changes of MRS upon binding the enzyme.

REFERENCES

1. Urban, S., and Freeman, M. (2002) Intramembrane proteolysis controls diverse signalling pathways throughout evolution. *Current opinion in genetics & development* **12**, 512-518
2. Brown, M., Ye, J., Rawson, R., and Goldstein, J. (2000) Regulated Intramembrane Proteolysis A Control Mechanism Conserved from Bacteria to Humans. *Cell* **100**, 391-398
3. Wolfe, M. S., and Kopan, R. (2004) Intramembrane proteolysis: theme and variations. *Science* **305**, 1119-1123
4. McCarthy, A. J., Coleman-Vaughan, C., and McCarthy, J. V. (2017) Regulated intramembrane proteolysis: emergent role in cell signalling pathways. *Biochemical Society transactions* **45**, 1185-1202
5. Langosch, D., Scharnagl, C., Steiner, H., and Lemberg, M. K. (2015) Understanding intramembrane proteolysis: from protein dynamics to reaction kinetics. *Trends in biochemical sciences* **40**, 318-327
6. Wolfe, M. S. (2009) Intramembrane proteolysis. *Chemical reviews* **109**, 1599-1612
7. Urban, S. (2016) A guide to the rhomboid protein superfamily in development and disease. *Seminars in cell & developmental biology* **60**, 1-4
8. Verhelst, S. H. L. (2017) Intramembrane proteases as drug targets. *The FEBS journal* **284**, 1489-1502
9. Mentrup, T., Looock, A. C., Fluhrer, R., and Schroder, B. (2017) Signal peptide peptidase and SPP-like proteases - Possible therapeutic targets? *Biochimica et biophysica acta* **1864**, 2169-2182
10. Arutyunova, E., Panwar, P., Skiba, P. M., Gale, N., Mak, M. W., and Lemieux, M. J. (2014) Allosteric regulation of rhomboid intramembrane proteolysis. *The EMBO journal* **33**, 1869-1881
11. Kinch, L. N., Ginalski, K., and Grishin, N. V. (2006) Site-2 protease regulated intramembrane proteolysis: sequence homologs suggest an ancient signaling cascade. *Protein science : a publication of the Protein Society* **15**, 84-93
12. Boyartchuk, V. L., Ashby, M. N., and Rine, J. (1997) Modulation of Ras and a-factor function by carboxyl-terminal proteolysis. *Science* **275**, 1796-1800

13. Ponting, C. P., Hutton, M., Nyborg, A., Baker, M., Jansen, K., and Golde, T. E. (2002) Identification of a novel family of presenilin homologues. *Human molecular genetics* **11**, 1037-1044
14. Wasserman, J. D., and Freeman, M. (1997) Control of EGF receptor activation in *Drosophila*. *Trends in cell biology* **7**, 431-436
15. Mayer, U., and Nusslein-Volhard, C. (1988) A group of genes required for pattern formation in the ventral ectoderm of the *Drosophila* embryo. *Genes & development* **2**, 1496-1511
16. Schweitzer, R., and Shilo, B. Z. (1997) A thousand and one roles for the *Drosophila* EGF receptor. *Trends in genetics : TIG* **13**, 191-196
17. Sibley, L. D. (2013) The roles of intramembrane proteases in protozoan parasites. *Biochimica et biophysica acta* **1828**, 2908-2915
18. Mesak, L. R., Mesak, F. M., and Dahl, M. K. (2004) Expression of a novel gene, gluP, is essential for normal *Bacillus subtilis* cell division and contributes to glucose export. *BMC microbiology* **4**, 13
19. Stevenson, L. G., Strisovsky, K., Clemmer, K. M., Bhatt, S., Freeman, M., and Rather, P. N. (2007) Rhomboid protease AarA mediates quorum-sensing in *Providencia stuartii* by activating TatA of the twin-arginine translocase. *Proceedings of the National Academy of Sciences of the United States of America* **104**, 1003-1008
20. Bergbold, N., and Lemberg, M. K. (2013) Emerging role of rhomboid family proteins in mammalian biology and disease. *Biochimica et biophysica acta* **1828**, 2840-2848
21. Chan, E. Y., and McQuibban, G. A. (2013) The mitochondrial rhomboid protease: its rise from obscurity to the pinnacle of disease-relevant genes. *Biochimica et biophysica acta* **1828**, 2916-2925
22. Song, W., Liu, W., Zhao, H., Li, S., Guan, X., Ying, J., Zhang, Y., Miao, F., Zhang, M., Ren, X., Li, X., Wu, F., Zhao, Y., Tian, Y., Wu, W., Fu, J., Liang, J., Wu, W., Liu, C., Yu, J., Zong, S., Miao, S., Zhang, X., and Wang, L. (2015) Rhomboid domain containing 1 promotes colorectal cancer growth through activation of the EGFR signalling pathway. *Nature communications* **6**, 8022
23. Dusterhoft, S., Kunzel, U., and Freeman, M. (2017) Rhomboid proteases in human disease: Mechanisms and future prospects. *Biochimica et biophysica acta* **1864**, 2200-2209

24. Lemberg, M. K., Menendez, J., Misik, A., Garcia, M., Koth, C. M., and Freeman, M. (2005) Mechanism of intramembrane proteolysis investigated with purified rhomboid proteases. *The EMBO journal* **24**, 464-472
25. Urban, S., Lee, J. R., and Freeman, M. (2001) Drosophila rhomboid-1 defines a family of putative intramembrane serine proteases. *Cell* **107**, 173-182
26. Wu, Z., Yan, N., Feng, L., Oberstein, A., Yan, H., Baker, R. P., Gu, L., Jeffrey, P. D., Urban, S., and Shi, Y. (2006) Structural analysis of a rhomboid family intramembrane protease reveals a gating mechanism for substrate entry. *Nature structural & molecular biology* **13**, 1084-1091
27. Lemieux, M. J., Fischer, S. J., Cherney, M. M., Bateman, K. S., and James, M. N. (2007) The crystal structure of the rhomboid peptidase from Haemophilus influenzae provides insight into intramembrane proteolysis. *Proceedings of the National Academy of Sciences of the United States of America* **104**, 750-754
28. Wang, Y., Zhang, Y., and Ha, Y. (2006) Crystal structure of a rhomboid family intramembrane protease. *Nature* **444**, 179-180
29. Baker, R. P., Young, K., Feng, L., Shi, Y., and Urban, S. (2007) Enzymatic analysis of a rhomboid intramembrane protease implicates transmembrane helix 5 as the lateral substrate gate. *Proceedings of the National Academy of Sciences of the United States of America* **104**, 8257-8262
30. Brooks, C. L., Lazareno-Saez, C., Lamoureux, J. S., Mak, M. W., and Lemieux, M. J. (2011) Insights into substrate gating in H. influenzae rhomboid. *Journal of molecular biology* **407**, 687-697
31. Dickey, S. W., Baker, R. P., Cho, S., and Urban, S. (2013) Proteolysis inside the membrane is a rate-governed reaction not driven by substrate affinity. *Cell* **155**, 1270-1281
32. Lazareno-Saez, C., Arutyunova, E., Coquelle, N., and Lemieux, M. J. (2013) Domain swapping in the cytoplasmic domain of the Escherichia coli rhomboid protease. *Journal of molecular biology* **425**, 1127-1142
33. Strisovsky, K., Sharpe, H. J., and Freeman, M. (2009) Sequence-specific intramembrane proteolysis: identification of a recognition motif in rhomboid substrates. *Molecular cell* **36**, 1048-1059
34. Zoll, S., Stanchev, S., Began, J., Skerle, J., Lepsik, M., Peclinovska, L., Majer, P., and Strisovsky, K. (2014) Substrate binding and specificity of rhomboid intramembrane protease revealed by substrate-peptide complex structures. *The EMBO journal* **33**, 2408-2421

35. Chen, K., Gu, L., Xiang, X., Lynch, M., and Zhou, R. (2012) Identification and characterization of five intramembrane metalloproteases in *Anabaena variabilis*. *Journal of bacteriology* **194**, 6105-6115
36. Nohturfft, A., DeBose-Boyd, R. A., Scheek, S., Goldstein, J. L., and Brown, M. S. (1999) Sterols regulate cycling of SREBP cleavage-activating protein (SCAP) between endoplasmic reticulum and Golgi. *Proceedings of the National Academy of Sciences of the United States of America* **96**, 11235-11240
37. Nohturfft, A., Yabe, D., Goldstein, J. L., Brown, M. S., and Espenshade, P. J. (2000) Regulated step in cholesterol feedback localized to budding of SCAP from ER membranes. *Cell* **102**, 315-323
38. Duncan, E. A., Dave, U. P., Sakai, J., Goldstein, J. L., and Brown, M. S. (1998) Second-site cleavage in sterol regulatory element-binding protein occurs at transmembrane junction as determined by cysteine panning. *The Journal of biological chemistry* **273**, 17801-17809
39. Sakai, J., Duncan, E. A., Rawson, R. B., Hua, X., Brown, M. S., and Goldstein, J. L. (1996) Sterol-regulated release of SREBP-2 from cell membranes requires two sequential cleavages, one within a transmembrane segment. *Cell* **85**, 1037-1046
40. Feng, L., Yan, H., Wu, Z., Yan, N., Wang, Z., Jeffrey, P. D., and Shi, Y. (2007) Structure of a site-2 protease family intramembrane metalloprotease. *Science* **318**, 1608-1612
41. Manolaridis, I., Kulkarni, K., Dodd, R. B., Ogasawara, S., Zhang, Z., Bineva, G., O'Reilly, N., Hanrahan, S. J., Thompson, A. J., Cronin, N., Iwata, S., and Barford, D. (2013) Mechanism of farnesylated CAAX protein processing by the intramembrane protease Rce1. *Nature* **504**, 301-305
42. Pei, J., and Grishin, N. V. (2001) Type II CAAX prenyl endopeptidases belong to a novel superfamily of putative membrane-bound metalloproteases. *Trends in biochemical sciences* **26**, 275-277
43. Michaelis, S., and Barrowman, J. (2012) Biogenesis of the *Saccharomyces cerevisiae* pheromone α -factor, from yeast mating to human disease. *Microbiology and molecular biology reviews : MMBR* **76**, 626-651
44. Christiansen, J. R., Kolandaivelu, S., Bergo, M. O., and Ramamurthy, V. (2011) RAS-converting enzyme 1-mediated endoproteolysis is required for trafficking of rod phosphodiesterase 6 to photoreceptor outer segments. *Proceedings of the National Academy of Sciences of the United States of America* **108**, 8862-8866
45. Winter-Vann, A. M., and Casey, P. J. (2005) Post-prenylation-processing enzymes as new targets in oncogenesis. *Nature reviews. Cancer* **5**, 405-412

46. Michaelson, D., Ali, W., Chiu, V. K., Bergo, M., Silletti, J., Wright, L., Young, S. G., and Philips, M. (2005) Postprenylation CAAX processing is required for proper localization of Ras but not Rho GTPases. *Molecular biology of the cell* **16**, 1606-1616
47. Kim, E., Ambroziak, P., Otto, J. C., Taylor, B., Ashby, M., Shannon, K., Casey, P. J., and Young, S. G. (1999) Disruption of the mouse Rce1 gene results in defective Ras processing and mislocalization of Ras within cells. *The Journal of biological chemistry* **274**, 8383-8390
48. Bergo, M. O., Leung, G. K., Ambroziak, P., Otto, J. C., Casey, P. J., Gomes, A. Q., Seabra, M. C., and Young, S. G. (2001) Isoprenylcysteine carboxyl methyltransferase deficiency in mice. *The Journal of biological chemistry* **276**, 5841-5845
49. Pei, J., Kim, B. H., and Grishin, N. V. (2008) PROMALS3D: a tool for multiple protein sequence and structure alignments. *Nucleic acids research* **36**, 2295-2300
50. Weihofen, A., and Martoglio, B. (2003) Intramembrane-cleaving proteases: controlled liberation of proteins and bioactive peptides. *Trends in cell biology* **13**, 71-78
51. Sato, T., Nyborg, A. C., Iwata, N., Diehl, T. S., Saido, T. C., Golde, T. E., and Wolfe, M. S. (2006) Signal peptide peptidase: biochemical properties and modulation by nonsteroidal antiinflammatory drugs. *Biochemistry* **45**, 8649-8656
52. Torres-Arancivia, C., Ross, C. M., Chavez, J., Assur, Z., Dolios, G., Mancina, F., and Ubarretxena-Belandia, I. (2010) Identification of an archaeal presenilin-like intramembrane protease. *PloS one* **5**, e13072
53. Dang, S., Wu, S., Wang, J., Li, H., Huang, M., He, W., Li, Y. M., Wong, C. C., and Shi, Y. (2015) Cleavage of amyloid precursor protein by an archaeal presenilin homologue PSH. *Proceedings of the National Academy of Sciences of the United States of America* **112**, 3344-3349
54. Li, X., Dang, S., Yan, C., Gong, X., Wang, J., and Shi, Y. (2013) Structure of a presenilin family intramembrane aspartate protease. *Nature* **493**, 56-61
55. Sun, L., Zhao, L., Yang, G., Yan, C., Zhou, R., Zhou, X., Xie, T., Zhao, Y., Wu, S., Li, X., and Shi, Y. (2015) Structural basis of human gamma-secretase assembly. *Proceedings of the National Academy of Sciences of the United States of America* **112**, 6003-6008

56. Naing, S. H., Vukoti, K. M., Drury, J. E., Johnson, J. L., Kalyoncu, S., Hill, S. E., Torres, M. P., and Lieberman, R. L. (2015) Catalytic Properties of Intramembrane Aspartyl Protease Substrate Hydrolysis Evaluated Using a FRET Peptide Cleavage Assay. *ACS chemical biology* **10**, 2166-2174
57. Bai, X. C., Yan, C., Yang, G., Lu, P., Ma, D., Sun, L., Zhou, R., Scheres, S. H., and Shi, Y. (2015) An atomic structure of human gamma-secretase. *Nature* **525**, 212-217
58. Weihofen, A., Binns, K., Lemberg, M. K., Ashman, K., and Martoglio, B. (2002) Identification of signal peptide peptidase, a presenilin-type aspartic protease. *Science* **296**, 2215-2218
59. Voss, M., Schroder, B., and Fluhrer, R. (2013) Mechanism, specificity, and physiology of signal peptide peptidase (SPP) and SPP-like proteases. *Biochimica et biophysica acta* **1828**, 2828-2839
60. Narayanan, S., Sato, T., and Wolfe, M. S. (2007) A C-terminal region of signal peptide peptidase defines a functional domain for intramembrane aspartic protease catalysis. *The Journal of biological chemistry* **282**, 20172-20179
61. Wang, J., Beher, D., Nyborg, A. C., Shearman, M. S., Golde, T. E., and Goate, A. (2006) C-terminal PAL motif of presenilin and presenilin homologues required for normal active site conformation. *Journal of neurochemistry* **96**, 218-227
62. Wang, J., Brunkan, A. L., Hecimovic, S., Walker, E., and Goate, A. (2004) Conserved "PAL" sequence in presenilins is essential for gamma-secretase activity, but not required for formation or stabilization of gamma-secretase complexes. *Neurobiology of disease* **15**, 654-666
63. Sato, C., Takagi, S., Tomita, T., and Iwatsubo, T. (2008) The C-terminal PAL motif and transmembrane domain 9 of presenilin 1 are involved in the formation of the catalytic pore of the gamma-secretase. *The Journal of neuroscience : the official journal of the Society for Neuroscience* **28**, 6264-6271
64. De Strooper, B., Iwatsubo, T., and Wolfe, M. S. (2012) Presenilins and gamma-secretase: structure, function, and role in Alzheimer Disease. *Cold Spring Harbor perspectives in medicine* **2**, a006304
65. Ito, E., Oka, K., Etcheberrigaray, R., Nelson, T. J., McPhie, D. L., Tofel-Grehl, B., Gibson, G. E., and Alkon, D. L. (1994) Internal Ca²⁺ mobilization is altered in fibroblasts from patients with Alzheimer disease. *Proceedings of the National Academy of Sciences of the United States of America* **91**, 534-538

66. Tu, H., Nelson, O., Bezprozvanny, A., Wang, Z., Lee, S. F., Hao, Y. H., Serneels, L., De Strooper, B., Yu, G., and Bezprozvanny, I. (2006) Presenilins form ER Ca²⁺ leak channels, a function disrupted by familial Alzheimer's disease-linked mutations. *Cell* **126**, 981-993
67. Murayama, M., Tanaka, S., Palacino, J., Murayama, O., Honda, T., Sun, X., Yasutake, K., Nihonmatsu, N., Wolozin, B., and Takashima, A. (1998) Direct association of presenilin-1 with beta-catenin. *FEBS letters* **433**, 73-77
68. Soriano, S., Kang, D. E., Fu, M., Pestell, R., Chevallier, N., Zheng, H., and Koo, E. H. (2001) Presenilin 1 negatively regulates beta-catenin/T cell factor/lymphoid enhancer factor-1 signaling independently of beta-amyloid precursor protein and notch processing. *The Journal of cell biology* **152**, 785-794
69. Zhang, Z., Hartmann, H., Do, V. M., Abramowski, D., Sturchler-Pierrat, C., Staufenbiel, M., Sommer, B., van de Wetering, M., Clevers, H., Saftig, P., De Strooper, B., He, X., and Yankner, B. A. (1998) Destabilization of beta-catenin by mutations in presenilin-1 potentiates neuronal apoptosis. *Nature* **395**, 698-702
70. Cox, R. T., McEwen, D. G., Myster, D. L., Duronio, R. J., Loureiro, J., and Peifer, M. (2000) A screen for mutations that suppress the phenotype of *Drosophila armadillo*, the beta-catenin homolog. *Genetics* **155**, 1725-1740
71. Noll, E., Medina, M., Hartley, D., Zhou, J., Perrimon, N., and Kosik, K. S. (2000) Presenilin affects arm/beta-catenin localization and function in *Drosophila*. *Developmental biology* **227**, 450-464
72. Xia, X., Qian, S., Soriano, S., Wu, Y., Fletcher, A. M., Wang, X. J., Koo, E. H., Wu, X., and Zheng, H. (2001) Loss of presenilin 1 is associated with enhanced beta-catenin signaling and skin tumorigenesis. *Proceedings of the National Academy of Sciences of the United States of America* **98**, 10863-10868
73. Martoglio, B., and Golde, T. E. (2003) Intramembrane-cleaving aspartic proteases and disease: presenilins, signal peptide peptidase and their homologs. *Human molecular genetics* **12 Spec No 2**, R201-206
74. Lemberg, M. K., Bland, F. A., Weihofen, A., Braud, V. M., and Martoglio, B. (2001) Intramembrane proteolysis of signal peptides: an essential step in the generation of HLA-E epitopes. *Journal of immunology (Baltimore, Md. : 1950)* **167**, 6441-6446
75. Fluhner, R., Grammer, G., Israel, L., Condrón, M. M., Haffner, C., Friedmann, E., Bohland, C., Imhof, A., Martoglio, B., Teplow, D. B., and Haass, C. (2006) A gamma-secretase-like intramembrane cleavage of TNFalpha by the GxGD aspartyl protease SPPL2b. *Nature cell biology* **8**, 894-896

76. McLauchlan, J., Lemberg, M. K., Hope, G., and Martoglio, B. (2002) Intramembrane proteolysis promotes trafficking of hepatitis C virus core protein to lipid droplets. *The EMBO journal* **21**, 3980-3988
77. Nyborg, A. C., Ladd, T. B., Jansen, K., Kukar, T., and Golde, T. E. (2006) Intramembrane proteolytic cleavage by human signal peptide peptidase like 3 and malaria signal peptide peptidase. *FASEB journal : official publication of the Federation of American Societies for Experimental Biology* **20**, 1671-1679
78. Krawitz, P., Haffner, C., Fluhrer, R., Steiner, H., Schmid, B., and Haass, C. (2005) Differential localization and identification of a critical aspartate suggest non-redundant proteolytic functions of the presenilin homologues SPPL2b and SPPL3. *The Journal of biological chemistry* **280**, 39515-39523
79. Casso, D. J., Tanda, S., Biehs, B., Martoglio, B., and Kornberg, T. B. (2005) Drosophila signal peptide peptidase is an essential protease for larval development. *Genetics* **170**, 139-148
80. Lemberg, M. K., and Martoglio, B. (2002) Requirements for signal peptide peptidase-catalyzed intramembrane proteolysis. *Molecular cell* **10**, 735-744
81. Lichtenthaler, S. F., and Steiner, H. (2007) Sheddases and intramembrane-cleaving proteases: RIPPers of the membrane. Symposium on Regulated Intramembrane Proteolysis. *EMBO Reports* **8**, 537-541
82. Lichtenthaler, S. F., Haass, C., and Steiner, H. (2011) Regulated intramembrane proteolysis--lessons from amyloid precursor protein processing. *Journal of neurochemistry* **117**, 779-796
83. Struhl, G., and Adachi, A. (2000) Requirements for presenilin-dependent cleavage of notch and other transmembrane proteins. *Molecular cell* **6**, 625-636
84. Marambaud, P., Shioi, J., Serban, G., Georgakopoulos, A., Sarner, S., Nagy, V., Baki, L., Wen, P., Efthimiopoulos, S., Shao, Z., Wisniewski, T., and Robakis, N. K. (2002) A presenilin-1/gamma-secretase cleavage releases the E-cadherin intracellular domain and regulates disassembly of adherens junctions. *The EMBO journal* **21**, 1948-1956
85. Tomita, T., Tanaka, S., Morohashi, Y., and Iwatsubo, T. (2006) Presenilin-dependent intramembrane cleavage of ephrin-B1. *Molecular neurodegeneration* **1**, 2
86. Uemura, K., Kihara, T., Kuzuya, A., Okawa, K., Nishimoto, T., Ninomiya, H., Sugimoto, H., Kinoshita, A., and Shimohama, S. (2006) Characterization of sequential N-cadherin cleavage by ADAM10 and PS1. *Neuroscience letters* **402**, 278-283

87. von Heijne, G. (1985) Signal sequences. The limits of variation. *Journal of molecular biology* **184**, 99-105
88. von Heijne, G. (1983) Patterns of amino acids near signal-sequence cleavage sites. *European journal of biochemistry / FEBS* **133**, 17-21
89. Hubbard, S. J. (1998) The structural aspects of limited proteolysis of native proteins. *Biochimica et biophysica acta* **1382**, 191-206
90. Kroos, L., and Akiyama, Y. (2013) Biochemical and structural insights into intramembrane metalloprotease mechanisms. *Bba-Biomembranes* **1828**, 2873-2885
91. Seddon, A. M., Curnow, P., and Booth, P. J. (2004) Membrane proteins, lipids and detergents: not just a soap opera. *Biochimica et biophysica acta* **1666**, 105-117
92. Tummala, R., Green-Church, K. B., and Limbach, P. A. (2005) Interactions between sodium dodecyl sulfate micelles and peptides during matrix-assisted laser desorption/ionization mass spectrometry (MALDI-MS) of proteolytic digests. *Journal of the American Society for Mass Spectrometry* **16**, 1438-1446
93. Zhang, N., and Li, L. (2004) Effects of common surfactants on protein digestion and matrix-assisted laser desorption/ionization mass spectrometric analysis of the digested peptides using two-layer sample preparation. *Rapid communications in mass spectrometry : RCM* **18**, 889-896
94. Karas, M., Bahr, U., Ingendoh, A., Nordhoff, E., Stahl, B., Strupat, K., and Hillenkamp, F. (1990) Principles and applications of matrix-assisted UV laser desorption ionization mass-spectrometry. *Analytica Chimica Acta* **241**, 175-185
95. Rosinke, B., Strupat, K., Hillenkamp, F., Rosenbusch, J., Dencher, N., Kruger, U., and Galla, H. J. (1995) Matrix-assisted laser desorption/ionization mass-spectrometry (MALDI-MS) of membrane-proteins and noncovalent complexes. *Journal of Mass Spectrometry* **30**, 1462-1468
96. Schnaible, V., Michels, J., Zeth, K., Freigang, J., Welte, W., Buhler, S., Glocker, M. O., and Przybylski, M. (1997) Approaches to the characterization of membrane channel proteins (porins) by UV MALDI-MS. *International Journal of Mass Spectrometry* **169**, 165-177
97. Wallace, B. A. (2009) Protein characterisation by synchrotron radiation circular dichroism spectroscopy. *Quarterly reviews of biophysics* **42**, 317-370
98. Cascio, M., and Wallace, B. A. (1995) Effects of local environment on the circular dichroism spectra of polypeptides. *Analytical biochemistry* **227**, 90-100

99. Chen, Y., and Wallace, B. A. (1997) Secondary solvent effects on the circular dichroism spectra of polypeptides in non-aqueous environments: influence of polarisation effects on the far ultraviolet spectra of alamethicin. *Biophysical chemistry* **65**, 65-74
100. Mao, D., and Wallace, B. A. (1984) Differential light scattering and absorption flattening optical effects are minimal in the circular dichroism spectra of small unilamellar vesicles. *Biochemistry* **23**, 2667-2673
101. Wallace, B. A., and Mao, D. (1984) Circular dichroism analyses of membrane proteins: an examination of differential light scattering and absorption flattening effects in large membrane vesicles and membrane sheets. *Analytical biochemistry* **142**, 317-328
102. Wallace, B. A., and Teeters, C. L. (1987) Differential absorption flattening optical effects are significant in the circular dichroism spectra of large membrane fragments. *Biochemistry* **26**, 65-70
103. Krueger-Koplin, R. D., Sorgen, P. L., Krueger-Koplin, S. T., Rivera-Torres, I. O., Cahill, S. M., Hicks, D. B., Grinius, L., Krulwich, T. A., and Girvin, M. E. (2004) An evaluation of detergents for NMR structural studies of membrane proteins. *Journal of Biomolecular NMR* **28**, 43-57
104. Shi, G., Lee, J. R., Grimes, D. A., Racacho, L., Ye, D., Yang, H., Ross, O. A., Farrer, M., McQuibban, G. A., and Bulman, D. E. (2011) Functional alteration of PARL contributes to mitochondrial dysregulation in Parkinson's disease. *Human molecular genetics* **20**, 1966-1974
105. Guan, M., Su, L., Yuan, Y. C., Li, H., and Chow, W. A. (2015) Nelfinavir and nelfinavir analogs block site-2 protease cleavage to inhibit castration-resistant prostate cancer. *Scientific reports* **5**, 9698
106. Mohammed, I., Hampton, S. E., Ashall, L., Hildebrandt, E. R., Kutlik, R. A., Manandhar, S. P., Floyd, B. J., Smith, H. E., Dozier, J. K., Distefano, M. D., Schmidt, W. K., and Dore, T. M. (2016) 8-Hydroxyquinoline-based inhibitors of the Rce1 protease disrupt Ras membrane localization in human cells. *Bioorganic & medicinal chemistry* **24**, 160-178

107. Sherrington, R., Rogaev, E. I., Liang, Y., Rogaeva, E. A., Levesque, G., Ikeda, M., Chi, H., Lin, C., Li, G., Holman, K., Tsuda, T., Mar, L., Foncin, J. F., Bruni, A. C., Montesi, M. P., Sorbi, S., Rainero, I., Pinessi, L., Nee, L., Chumakov, I., Pollen, D., Brookes, A., Sanseau, P., Polinsky, R. J., Wasco, W., Da Silva, H. A., Haines, J. L., Perkicak-Vance, M. A., Tanzi, R. E., Roses, A. D., Fraser, P. E., Rommens, J. M., and St George-Hyslop, P. H. (1995) Cloning of a gene bearing missense mutations in early-onset familial Alzheimer's disease. *Nature* **375**, 754-760
108. Sato, T., Diehl, T. S., Narayanan, S., Funamoto, S., Ihara, Y., De Strooper, B., Steiner, H., Haass, C., and Wolfe, M. S. (2007) Active gamma-secretase complexes contain only one of each component. *The Journal of biological chemistry* **282**, 33985-33993
109. Kimberly, W. T., LaVoie, M. J., Ostaszewski, B. L., Ye, W., Wolfe, M. S., and Selkoe, D. J. (2003) Gamma-secretase is a membrane protein complex comprised of presenilin, nicastrin, Aph-1, and Pen-2. *Proceedings of the National Academy of Sciences of the United States of America* **100**, 6382-6387
110. Edbauer, D., Winkler, E., Regula, J. T., Pesold, B., Steiner, H., and Haass, C. (2003) Reconstitution of gamma-secretase activity. *Nature cell biology* **5**, 486-488
111. Shah, S., Lee, S. F., Tabuchi, K., Hao, Y. H., Yu, C., LaPlant, Q., Ball, H., Dann, C. E., 3rd, Sudhof, T., and Yu, G. (2005) Nicastrin functions as a gamma-secretase-substrate receptor. *Cell* **122**, 435-447
112. Niimura, M., Isoo, N., Takasugi, N., Tsuruoka, M., Ui-Tei, K., Saigo, K., Morohashi, Y., Tomita, T., and Iwatsubo, T. (2005) Aph-1 contributes to the stabilization and trafficking of the gamma-secretase complex through mechanisms involving intermolecular and intramolecular interactions. *The Journal of biological chemistry* **280**, 12967-12975
113. Luo, W. J., Wang, H., Li, H., Kim, B. S., Shah, S., Lee, H. J., Thinakaran, G., Kim, T. W., Yu, G., and Xu, H. (2003) PEN-2 and APH-1 coordinately regulate proteolytic processing of presenilin 1. *The Journal of biological chemistry* **278**, 7850-7854
114. Thinakaran, G., Borchelt, D. R., Lee, M. K., Slunt, H. H., Spitzer, L., Kim, G., Ratovitsky, T., Davenport, F., Nordstedt, C., Seeger, M., Hardy, J., Levey, A. I., Gandy, S. E., Jenkins, N. A., Copeland, N. G., Price, D. L., and Sisodia, S. S. (1996) Endoproteolysis of presenilin 1 and accumulation of processed derivatives in vivo. *Neuron* **17**, 181-190

115. Brunkan, A. L., Martinez, M., Walker, E. S., and Goate, A. M. (2005) Presenilin endoproteolysis is an intramolecular cleavage. *Molecular and cellular neurosciences* **29**, 65-73
116. De Strooper, B., Vassar, R., and Golde, T. (2010) The secretases: enzymes with therapeutic potential in Alzheimer disease. *Nature reviews. Neurology* **6**, 99-107
117. Ranganathan, P., Weaver, K. L., and Capobianco, A. J. (2011) Notch signalling in solid tumours: a little bit of everything but not all the time. *Nature reviews. Cancer* **11**, 338-351
118. Doody, R. S., Raman, R., Farlow, M., Iwatsubo, T., Vellas, B., Joffe, S., Kieburtz, K., He, F., Sun, X., Thomas, R. G., Aisen, P. S., Siemers, E., Sethuraman, G., and Mohs, R. (2013) A phase 3 trial of semagacestat for treatment of Alzheimer's disease. *The New England journal of medicine* **369**, 341-350
119. Hedstrom, L. (2002) Serine protease mechanism and specificity. *Chem. Rev.* **102**, 4501-4524
120. Dunn, B. M. (2002) Structure and mechanism of the pepsin-like family of aspartic peptidases. *Chem. Rev.* **102**, 4431-4458
121. Erez, E., Fass, D., and Bibi, E. (2009) How intramembrane proteases bury hydrolytic reactions in the membrane. *Nature* **459**, 371-378
122. Osenkowski, P., Ye, W., Wang, R., Wolfe, M. S., and Selkoe, D. J. (2008) Direct and potent regulation of gamma-secretase by its lipid microenvironment. *The Journal of biological chemistry* **283**, 22529-22540
123. Fraering, P. C., Ye, W., Strub, J. M., Dolios, G., LaVoie, M. J., Ostaszewski, B. L., van Dorsselaer, A., Wang, R., Selkoe, D. J., and Wolfe, M. S. (2004) Purification and characterization of the human gamma-secretase complex. *Biochemistry* **43**, 9774-9789
124. Wolfe, M. S. (2008) Inhibition and modulation of gamma-secretase for Alzheimer's disease. *Neurotherapeutics : the journal of the American Society for Experimental NeuroTherapeutics* **5**, 391-398
125. Kamp, F., Winkler, E., Trambauer, J., Ebke, A., Fluhner, R., and Steiner, H. (2015) Intramembrane Proteolysis of beta-Amyloid Precursor Protein by gamma-Secretase Is an Unusually Slow Process. *Biophys. J.* **108**, 1229-1237
126. van den Ent, F., and Lowe, J. (2006) RF cloning: a restriction-free method for inserting target genes into plasmids. *Journal of biochemical and biophysical methods* **67**, 67-74

127. Sambrook J, R. D. (2001) *Molecular cloning: a laboratory manual*, Cold Spring Harbor Laboratory Press. 3 v. p., Cold Spring Harbor, N.Y
128. Gasteiger, E., Hoogland, C., Gattiker, A., Duvaud, S., Wilkins, M. R., Appel, R. D., and Bairoch, A. (2005) Protein Identification and Analysis Tools on the ExPASy Server. *The Proteomics Protocols Handbook*, 571-607
129. Jaulent, A. M., Fahy, A. S., Knox, S. R., Birtley, J. R., Roque-Rosell, N., Curry, S., and Leatherbarrow, R. J. (2007) A continuous assay for foot-and-mouth disease virus 3C protease activity. *Analytical biochemistry* **368**, 130-137
130. Ujwal, R., and Bowie, J. U. (2011) Crystallizing membrane proteins using lipidic bicelles. *Methods (San Diego, Calif.)* **55**, 337-341
131. Nyborg, A. C., Herl, L., Berezovska, O., Thomas, A. V., Ladd, T. B., Jansen, K., Hyman, B. T., and Golde, T. E. (2006) Signal peptide peptidase (SPP) dimer formation as assessed by fluorescence lifetime imaging microscopy (FLIM) in intact cells. *Molecular neurodegeneration* **1**, 16
132. Lorsch, J. R. (2014) Practical steady-state enzyme kinetics. *Methods in enzymology* **536**, 3-15
133. Haass, C. (2002) New hope for Alzheimer disease vaccine. *Nature medicine* **8**, 1195-1196
134. Holzman, T. F., Chung, C. C., Edalji, R., Egan, D. A., Martin, M., Gubbins, E. J., Krafft, G. A., Wang, G. T., Thomas, A. M., Rosenberg, S. H., and et al. (1991) Characterization of recombinant human renin: kinetics, pH-stability, and peptidomimetic inhibitor binding. *Journal of protein chemistry* **10**, 553-563
135. Capobianco, J. O., Lerner, C. G., and Goldman, R. C. (1992) Application of a fluorogenic substrate in the assay of proteolytic activity and in the discovery of a potent inhibitor of *Candida albicans* aspartic proteinase. *Anal. Biochem.* **204**, 96-102
136. Weihofen, A., Lemberg, M. K., Ploegh, H. L., Bogoy, M., and Martoglio, B. (2000) Release of signal peptide fragments into the cytosol requires cleavage in the transmembrane region by a protease activity that is specifically blocked by a novel cysteine protease inhibitor. *The Journal of biological chemistry* **275**, 30951-30956
137. Otto, J. C., Kim, E., Young, S. G., and Casey, P. J. (1999) Cloning and characterization of a mammalian prenyl protein-specific protease. *J. Biol. Chem.* **274**, 8379-8382

138. Kornilova, A. Y., Das, C., and Wolfe, M. S. (2003) Differential effects of inhibitors on the gamma-secretase complex. Mechanistic implications. *The Journal of biological chemistry* **278**, 16470-16473
139. Sato, T., Ananda, K., Cheng, C. I., Suh, E. J., Narayanan, S., and Wolfe, M. S. (2008) Distinct pharmacological effects of inhibitors of signal peptide peptidase and gamma-secretase. *The Journal of biological chemistry* **283**, 33287-33295
140. Nyborg, A. C., Kornilova, A. Y., Jansen, K., Ladd, T. B., Wolfe, M. S., and Golde, T. E. (2004) Signal peptide peptidase forms a homodimer that is labeled by an active site-directed gamma-secretase inhibitor. *The Journal of biological chemistry* **279**, 15153-15160
141. Fuwa, H., Takahashi, Y., Konno, Y., Watanabe, N., Miyashita, H., Sasaki, M., Natsugari, H., Kan, T., Fukuyama, T., Tomita, T., and Iwatsubo, T. (2007) Divergent synthesis of multifunctional molecular probes to elucidate the enzyme specificity of dipeptidic gamma-secretase inhibitors. *ACS Chem. Biol.* **2**, 408-418
142. Morohashi, Y., Kan, T., Tominari, Y., Fuwa, H., Okamura, Y., Watanabe, N., Sato, C., Natsugari, H., Fukuyama, T., Iwatsubo, T., and Tomita, T. (2006) C-terminal fragment of presenilin is the molecular target of a dipeptidic gamma-secretase-specific inhibitor DAPT (N-[N-(3,5-difluorophenacetyl)-L-alanyl]-S-phenylglycine t-butyl ester). *The Journal of biological chemistry* **281**, 14670-14676
143. Walsh, D. M., Klyubin, I., Fadeeva, J. V., Cullen, W. K., Anwyl, R., Wolfe, M. S., Rowan, M. J., and Selkoe, D. J. (2002) Naturally secreted oligomers of amyloid beta protein potently inhibit hippocampal long-term potentiation in vivo. *Nature* **416**, 535-539
144. Klebe, G. (2013) Aspartic Protease Inhibitors. in *Drug Design* (Klebe, G. ed.), Springer Berlin Heidelberg. pp 533-564
145. Nyborg, A. C., Jansen, K., Ladd, T. B., Fauq, A., and Golde, T. E. (2004) A signal peptide peptidase (SPP) reporter activity assay based on the cleavage of type II membrane protein substrates provides further evidence for an inverted orientation of the SPP active site relative to presenilin. *J. Biol. Chem.* **279**, 43148-43156
146. Dev, K. K., Chatterjee, S., Osinde, M., Stauffer, D., Morgan, H., Kobialko, M., Dengler, U., Rueeger, H., Martoglio, B., and Rovelli, G. (2006) Signal peptide peptidase dependent cleavage of type II transmembrane substrates releases intracellular and extracellular signals. *European journal of pharmacology* **540**, 10-17

147. Haapasalo, A., and Kovacs, D. M. (2011) The many substrates of presenilin/gamma-secretase. *J Alzheimers Dis* **25**, 3-28
148. Petersen, T. N., Brunak, S., von Heijne, G., and Nielsen, H. (2011) SignalP 4.0: discriminating signal peptides from transmembrane regions. *Nature methods* **8**, 785-786
149. Tewksbury, D. A., Dart, R. A., and Travis, J. (1981) The amino terminal amino acid sequence of human angiotensinogen. *Biochem. Biophys. Res. Commun.* **99**, 1311-1315
150. Kumar-Singh, S., Theuns, J., Van Broeck, B., Pirici, D., Vennekens, K., Corsmit, E., Cruts, M., Dermaut, B., Wang, R., and Van Broeckhoven, C. (2006) Mean age-of-onset of familial alzheimer disease caused by presenilin mutations correlates with both increased Abeta42 and decreased Abeta40. *Human mutation* **27**, 686-695
151. Tolia, A., Horre, K., and De Strooper, B. (2008) Transmembrane domain 9 of presenilin determines the dynamic conformation of the catalytic site of gamma-secretase. *The Journal of biological chemistry* **283**, 19793-19803
152. Wolfe, M. S. (2013) Toward the structure of presenilin/gamma-secretase and presenilin homologs. *Biochimica et biophysica acta* **1828**, 2886-2897
153. Takami, M., Nagashima, Y., Sano, Y., Ishihara, S., Morishima-Kawashima, M., Funamoto, S., and Ihara, Y. (2009) gamma-Secretase: successive tripeptide and tetrapeptide release from the transmembrane domain of beta-carboxyl terminal fragment. *The Journal of neuroscience : the official journal of the Society for Neuroscience* **29**, 13042-13052
154. Chow, V. W., Mattson, M. P., Wong, P. C., and Gleichmann, M. (2010) An overview of APP processing enzymes and products. *Neuromolecular Med* **12**, 1-12
155. Gasteiger, E., Hoogland, C., Gattiker, A., Duvaud, S. e., Wilkins, M. R., Appel, R. D., and Bairoch, A. (2005) Protein Identification and Analysis Tools on the ExPASy Server. in *The Proteomics Protocols Handbook* (Walker, J. M. ed.), Humana Press, Totowa, NJ. pp 571-607
156. Petoukhov, M. V., Franke, D., Shkumatov, A. V., Tria, G., Kikhney, A. G., Gajda, M., Gorba, C., Mertens, H. D. T., Konarev, P. V., and Svergun, D. I. (2012) New developments in the ATSAS program package for small-angle scattering data analysis. *J. Appl. Crystallogr.* **45**, 342-350

157. Krissinel, E., and Henrick, K. (2004) Secondary-structure matching (SSM), a new tool for fast protein structure alignment in three dimensions. *Acta Crystallogr. D* **60**, 2256-2268
158. Cruts, M., Theuns, J., and Van Broeckhoven, C. (2012) Locus-specific mutation databases for neurodegenerative brain diseases. *Hum Mutat* **33**, 1340-1344
159. De Jonghe, C., Cras, P., Vanderstichele, H., Cruts, M., Vanderhoeven, I., Smouts, I., Vanmechelen, E., Martin, J. J., Hendriks, L., and Van Broeckhoven, C. (1999) Evidence that Abeta42 plasma levels in presenilin-1 mutation carriers do not allow for prediction of their clinical phenotype. *Neurobiology of disease* **6**, 280-287
160. Steiner, H., Kostka, M., Romig, H., Basset, G., Pesold, B., Hardy, J., Capell, A., Meyn, L., Grim, M. L., Baumeister, R., Fichteler, K., and Haass, C. (2000) Glycine 384 is required for presenilin-1 function and is conserved in bacterial polytopic aspartyl proteases. *Nature cell biology* **2**, 848-851
161. Fluhner, R., Fukumori, A., Martin, L., Grammer, G., Haug-Kroper, M., Klier, B., Winkler, E., Kremmer, E., Condron, M. M., Teplow, D. B., Steiner, H., and Haass, C. (2008) Intramembrane proteolysis of GXGD-type aspartyl proteases is slowed by a familial Alzheimer disease-like mutation. *The Journal of biological chemistry* **283**, 30121-30128
162. Chavez-Gutierrez, L., Bammens, L., Benilova, I., Vandersteen, A., Benurwar, M., Borgers, M., Lismont, S., Zhou, L., Van Cleynenbreugel, S., Esselmann, H., Wiltfang, J., Serneels, L., Karran, E., Gijzen, H., Schymkowitz, J., Rousseau, F., Broersen, K., and De Strooper, B. (2012) The mechanism of gamma-Secretase dysfunction in familial Alzheimer disease. *The EMBO journal* **31**, 2261-2274
163. Veugelen, S., Saito, T., Saido, T. C., Chavez-Gutierrez, L., and De Strooper, B. (2016) Familial Alzheimer's Disease Mutations in Presenilin Generate Amyloidogenic Abeta Peptide Seeds. *Neuron* **90**, 410-416
164. Szaruga, M., Munteanu, B., Lismont, S., Veugelen, S., Horre, K., Mercken, M., Saido, T. C., Ryan, N. S., De Vos, T., Savvides, S. N., Gallardo, R., Schymkowitz, J., Rousseau, F., Fox, N. C., Hopf, C., De Strooper, B., and Chavez-Gutierrez, L. (2017) Alzheimer's-Causing Mutations Shift Abeta Length by Destabilizing gamma-Secretase-Abeta Interactions. *Cell* **170**, 443-456.e414
165. Theron, L. W., and Divol, B. (2014) Microbial aspartic proteases: current and potential applications in industry. *Appl Microbiol Biotechnol* **98**, 8853-8868

166. Farmery, M. R., Tjernberg, L. O., Pursglove, S. E., Bergman, A., Winblad, B., and Naslund, J. (2003) Partial purification and characterization of gamma-secretase from post-mortem human brain. *The Journal of biological chemistry* **278**, 24277-24284
167. Takeo, K., Tanimura, S., Shinoda, T., Osawa, S., Zahariev, I. K., Takegami, N., Ishizuka-Katsura, Y., Shinya, N., Takagi-Niidome, S., Tominaga, A., Ohsawa, N., Kimura-Someya, T., Shirouzu, M., Yokoshima, S., Yokoyama, S., Fukuyama, T., Tomita, T., and Iwatsubo, T. (2014) Allosteric regulation of gamma-secretase activity by a phenylimidazole-type gamma-secretase modulator. *Proceedings of the National Academy of Sciences of the United States of America* **111**, 10544-10549
168. Fukumori, A., Fluhner, R., Steiner, H., and Haass, C. (2010) Three-amino acid spacing of presenilin endoproteolysis suggests a general stepwise cleavage of gamma-secretase-mediated intramembrane proteolysis. *The Journal of neuroscience : the official journal of the Society for Neuroscience* **30**, 7853-7862
169. Pester, O., Barrett, P. J., Hornburg, D., Hornburg, P., Probstle, R., Widmaier, S., Kutzner, C., Durrbaum, M., Kapurniotu, A., Sanders, C. R., Scharnagl, C., and Langosch, D. (2013) The backbone dynamics of the amyloid precursor protein transmembrane helix provides a rationale for the sequential cleavage mechanism of gamma-secretase. *Journal of the American Chemical Society* **135**, 1317-1329
170. Shen, J. (2014) Function and dysfunction of presenilin. *Neurodegener Dis* **13**, 61-63
171. Beel, A. J., and Sanders, C. R. (2008) Substrate specificity of gamma-secretase and other intramembrane proteases. *Cell Mol Life Sci*
172. Morishima-Kawashima, M. (2014) Molecular mechanism of the intramembrane cleavage of the beta-carboxyl terminal fragment of amyloid precursor protein by gamma-secretase. *Front Physiol* **5**, 463
173. Bolduc, D. M., Montagna, D. R., Seghers, M. C., Wolfe, M. S., and Selkoe, D. J. (2016) The amyloid-beta forming tripeptide cleavage mechanism of gamma-secretase. *Elife* **5**
174. Khelashvili, G., Mondal, S., Andersen, O. S., and Weinstein, H. (2010) Cholesterol modulates the membrane effects and spatial organization of membrane-penetrating ligands for G-protein coupled receptors. *The journal of physical chemistry. B* **114**, 12046-12057
175. Yeagle, P. L. (1991) Modulation of membrane function by cholesterol. *Biochimie* **73**, 1303-1310

176. Barrett, P. J., Song, Y., Van Horn, W. D., Hustedt, E. J., Schafer, J. M., Hadziselimovic, A., Beel, A. J., and Sanders, C. R. (2012) The amyloid precursor protein has a flexible transmembrane domain and binds cholesterol. *Science* **336**, 1168-1171
177. Song, Y., Hustedt, E. J., Brandon, S., and Sanders, C. R. (2013) Competition between homodimerization and cholesterol binding to the C99 domain of the amyloid precursor protein. *Biochemistry* **52**, 5051-5064
178. Wood, W. G., Li, L., Muller, W. E., and Eckert, G. P. (2014) Cholesterol as a causative factor in Alzheimer's disease: a debatable hypothesis. *Journal of neurochemistry* **129**, 559-572
179. Maulik, M., Westaway, D., Jhamandas, J. H., and Kar, S. (2013) Role of cholesterol in APP metabolism and its significance in Alzheimer's disease pathogenesis. *Molecular neurobiology* **47**, 37-63
180. Li, Y. M., Lai, M. T., Xu, M., Huang, Q., DiMuzio-Mower, J., Sardana, M. K., Shi, X. P., Yin, K. C., Shafer, J. A., and Gardell, S. J. (2000) Presenilin 1 is linked with gamma-secretase activity in the detergent solubilized state. *Proceedings of the National Academy of Sciences of the United States of America* **97**, 6138-6143
181. Finn, R. D., Coghill, P., Eberhardt, R. Y., Eddy, S. R., Mistry, J., Mitchell, A. L., Potter, S. C., Punta, M., Qureshi, M., Sangrador-Vegas, A., Salazar, G. A., Tate, J., and Bateman, A. (2016) The Pfam protein families database: towards a more sustainable future. *Nucleic acids research* **44**, D279-285
182. Blaber, M., Zhang, X. J., and Matthews, B. W. (1993) Structural basis of amino acid alpha helix propensity. *Science* **260**, 1637-1640
183. Chakrabartty, A., Kortemme, T., and Baldwin, R. L. (1994) Helix propensities of the amino acids measured in alanine-based peptides without helix-stabilizing side-chain interactions. *Protein science : a publication of the Protein Society* **3**, 843-852
184. Pace, C. N., and Scholtz, J. M. (1998) A helix propensity scale based on experimental studies of peptides and proteins. *Biophysical journal* **75**, 422-427
185. Ballesteros, J. A., Deupi, X., Olivella, M., Haaksma, E. E., and Pardo, L. (2000) Serine and threonine residues bend alpha-helices in the chi(1) = g(-) conformation. *Biophysical journal* **79**, 2754-2760
186. Martoglio, B., Graf, R., and Dobberstein, B. (1997) Signal peptide fragments of preprolactin and HIV-1 p-gp160 interact with calmodulin. *The EMBO journal* **16**, 6636-6645

187. Ikeuchi, T., and Sisodia, S. S. (2003) The Notch ligands, Delta1 and Jagged2, are substrates for presenilin-dependent "gamma-secretase" cleavage. *The Journal of biological chemistry* **278**, 7751-7754
188. Zampieri, N., Xu, C. F., Neubert, T. A., and Chao, M. V. (2005) Cleavage of p75 neurotrophin receptor by alpha-secretase and gamma-secretase requires specific receptor domains. *The Journal of biological chemistry* **280**, 14563-14571
189. Lee, H. J., Jung, K. M., Huang, Y. Z., Bennett, L. B., Lee, J. S., Mei, L., and Kim, T. W. (2002) Presenilin-dependent gamma-secretase-like intramembrane cleavage of ErbB4. *The Journal of biological chemistry* **277**, 6318-6323
190. Tong, B. C., Lee, C. S., Cheng, W. H., Lai, K. O., Foskett, J. K., and Cheung, K. H. (2016) Familial Alzheimer's disease-associated presenilin 1 mutants promote gamma-secretase cleavage of STIM1 to impair store-operated Ca²⁺ entry. *Sci Signal* **9**, ra89
191. Deatherage, C. L., Lu, Z., Kroncke, B. M., Ma, S., Smith, J. A., Voehler, M. W., McFeeters, R. L., and Sanders, C. R. (2017) Structural and biochemical differences between the Notch and the amyloid precursor protein transmembrane domains. *Science advances* **3**, e1602794
192. Gimpl, K., Klement, J., and Keller, S. (2016) Characterising protein/detergent complexes by triple-detection size-exclusion chromatography. *Biol Proced Online* **18**, 4
193. Perez, J., and Koutsioubas, A. (2015) Memprot: a program to model the detergent corona around a membrane protein based on SEC-SAXS data. *Acta Crystallogr D Biol Crystallogr* **71**, 86-93
194. Miyashita, H., Maruyama, Y., Isshiki, H., Osawa, S., Ogura, T., Mio, K., Sato, C., Tomita, T., and Iwatsubo, T. (2011) Three-dimensional structure of the signal peptide peptidase. *The Journal of biological chemistry* **286**, 26188-26197
195. Cervantes, S., Saura, C. A., Pomares, E., Gonzalez-Duarte, R., and Marfany, G. (2004) Functional implications of the presenilin dimerization: reconstitution of gamma-secretase activity by assembly of a catalytic site at the dimer interface of two catalytically inactive presenilins. *The Journal of biological chemistry* **279**, 36519-36529
196. Herl, L., Lleo, A., Thomas, A. V., Nyborg, A. C., Jansen, K., Golde, T. E., Hyman, B. T., and Berezovska, O. (2006) Detection of presenilin-1 homodimer formation in intact cells using fluorescent lifetime imaging microscopy. *Biochem. Biophys. Res. Commun.* **340**, 668-674

197. Schroeter, E. H., Ilagan, M. X., Brunkan, A. L., Hecimovic, S., Li, Y. M., Xu, M., Lewis, H. D., Saxena, M. T., De Strooper, B., Coonrod, A., Tomita, T., Iwatsubo, T., Moore, C. L., Goate, A., Wolfe, M. S., Shearman, M., and Kopan, R. (2003) A presenilin dimer at the core of the gamma-secretase enzyme: insights from parallel analysis of Notch 1 and APP proteolysis. *Proc. Natl. Acad. Sci. U S A* **100**, 13075-13080
198. Breyton, C., Gabel, F., Lethier, M., Flayhan, A., Durand, G., Jault, J. M., Juillan-Binard, C., Imbert, L., Moulin, M., Ravaud, S., Hartlein, M., and Ebel, C. (2013) Small angle neutron scattering for the study of solubilised membrane proteins. *The European physical journal. E, Soft matter* **36**, 71
199. Jacques, D. A., and Trewthella, J. (2010) Small-angle scattering for structural biology--expanding the frontier while avoiding the pitfalls. *Protein science : a publication of the Protein Society* **19**, 642-657
200. Lynn, G. W., Heller, W., Urban, V., Wignall, G. D., Weiss, K., and Myles, D. A. (2006) Bio-SANS - A dedicated facility for neutron structural biology at oak ridge national laboratory. *Physica B* **385-86**, 880-882
201. Heller, W. T., Urban, V. S., Lynn, G. W., Weiss, K. L., O'Neill, H. M., Pingali, S. V., Qian, S., Littrell, K. C., Melnichenko, Y. B., Buchanan, M. V., Selby, D. L., Wignall, G. D., Butler, P. D., and Myles, D. A. (2014) The Bio-SANS instrument at the High Flux Isotope Reactor of Oak Ridge National Laboratory. *J. Appl. Crystallogr.* **47**, 1238-1246
202. He, L. L., Do, C., Qian, S., Wignall, G. D., Heller, W. T., Littrell, K. C., and Smith, G. S. (2015) Corrections for the geometric distortion of the tube detectors on SANS instruments at ORNL. *Nucl Instrum Meth A* **775**, 63-70
203. Arnold, O., Bilheux, J. C., Borreguero, J. M., Buts, A., Campbell, S. I., Chapon, L., Doucet, M., Draper, N., Leal, R. F., Gigg, M. A., Lynch, V. E., Markvardsen, A., Mikkelsen, D. J., Mikkelsen, R. L., Miller, R., Palmen, K., Parker, P., Passos, G., Perring, T. G., Peterson, P. F., Ren, S., Reuter, M. A., Savici, A. T., Taylor, J. W., Taylor, R. J., Tolchenoy, R., Zhou, W., and Zikoysky, J. (2014) Mantid-Data analysis and visualization package for neutron scattering and mu SR experiments. *Nucl. Instrum. Meth. A* **764**, 156-166
204. Konarev, P. V., Volkov, V. V., Sokolova, A. V., Koch, M. H. J., and Svergun, D. I. (2003) PRIMUS: a Windows PC-based system for small-angle scattering data analysis. *J. Appl. Crystallogr.* **36**, 1277-1282

205. Doucet, M., Cho, J. H., Alina, G., Bakker, J., Bouwman, W., Butler, P., Campbell, K., Gonzales, M., Heenan, R., Jackson, A., Juhas, P., King, S., Kienzle, P., Krzywon, J., Markvardsen, A., Nielsen, T., O'Driscoll, L., Potrzebowski, W., Ferraz Leal, R., Richter, T., Rozycko, P., and Washinton, A. (2017) SasView version 4.1.
206. Svergun, D. I., Richard, S., Koch, M. H. J., Sayers, Z., Kuprin, S., and Zaccai, G. (1998) Protein hydration in solution: Experimental observation by x-ray and neutron scattering. *Proc. Natl. Acad. Sci. U S A* **95**, 2267-2272
207. Svergun, D. (1992) Determination of the regularization parameter in indirect-transform methods using perceptual criteria. *J. Appl. Crystallogr.* **25**, 495-503
208. Svergun, D. I. (1999) Restoring low resolution structure of biological macromolecules from solution scattering using simulated annealing. *Biophys. J.* **76**, 2879-2886
209. Franke, D., and Svergun, D. I. (2009) DAMMIF, a program for rapid ab-initio shape determination in small-angle scattering. *J. Appl. Crystallogr.* **42**, 342-346
210. Volkov, V. V., and Svergun, D. I. (2003) Uniqueness of ab initio shape determination in small-angle scattering. *Journal of Applied Crystallography* **36**, 860-864
211. Kozin, M. B., and Svergun, D. I. (2001) Automated matching of high- and low-resolution structural models. *Journal of Applied Crystallography* **34**, 33-41
212. Leiting, B., Marsilio, F., and O'Connell, J. F. (1998) Predictable deuteration of recombinant proteins expressed in Escherichia coli. *Anal. Biochem.* **265**, 351-355
213. Oliver, R. C., Pingali, S. V., and Urban, V. S. (2017) Designing mixed detergent micelles for uniform neutron contrast. *J. Phys. Chem. Lett.* **8**, 5041-5046
214. Glatter, O., and Kratky, O. (1982) *Small angle x-ray scattering*, Academic Press, London; New York
215. Rambo, R. P., and Tainer, J. A. (2013) Accurate assessment of mass, models and resolution by small-angle scattering. *Nature* **496**, 477-+
216. Zaccai, N. R., Serdyuk, I. N., and Zaccai, J. (2017) *Methods in Molecular Biophysics*, Cambridge University Press
217. Parker, J. L., and Newstead, S. (2016) Membrane protein crystallisation: current trends and future perspectives. in *Next Generation in Membrane Protein Structure Determination*. pp 61-72

218. Prive, G. G. (2007) Detergents for the stabilization and crystallization of membrane proteins. *Methods (San Diego, Calif.)* **41**, 388-397
219. le Maire, M., Champeil, P., and Moller, J. V. (2000) Interaction of membrane proteins and lipids with solubilizing detergents. *Biochimica et biophysica acta* **1508**, 86-111
220. Hunt, J. F., McCrea, P. D., Zaccari, G., and Engelman, D. M. (1997) Assessment of the aggregation state of integral membrane proteins in reconstituted phospholipid vesicles using small angle neutron scattering11Edited by M. F. Moody. *J. Mol. Biol.* **273**, 1004-1019
221. Bu, Z., Wang, L., and Kendall, D. A. (2003) Nucleotide binding induces changes in the oligomeric state and conformation of Sec A in a lipid environment: a small-angle neutron-scattering study. *J. Mol. Biol.* **332**, 23-30
222. Zimmer, J., Doyle, D. A., and Grossmann, J. G. (2006) Structural Characterization and pH-Induced Conformational Transition of Full-Length KcsA. *Biophys. J.* **90**, 1752-1766
223. Cardoso, M. B., Smolensky, D., Heller, W. T., and O'Neill, H. (2009) Insight into the structure of light-harvesting complex II and its stabilization in detergent solution. *J. Phys. Chem. B* **113**, 16377-16383
224. Johs, A., Hammel, M., Waldner, I., May, R. P., Laggner, P., and Prassl, R. (2006) Modular structure of solubilized human apolipoprotein B-100. Low resolution model revealed by small angle neutron scattering. *J. Biol. Chem.* **281**, 19732-19739
225. Nogales, A., Garcia, C., Perez, J., Callow, P., Ezquerra, T. A., and Gonzalez-Rodriguez, J. (2010) Three-dimensional model of human platelet integrin α IIb β 3 in solution obtained by small angle neutron scattering. *J. Biol. Chem.* **285**, 1023-1031
226. Tang, K. H., Urban, V. S., Wen, J., Xin, Y., and Blankenship, R. E. (2010) SANS investigation of the photosynthetic machinery of *Chloroflexus aurantiacus*. *Biophys. J.* **99**, 2398-2407
227. Clifton, L. A., Johnson, C. L., Solovyova, A. S., Callow, P., Weiss, K. L., Ridley, H., Le Brun, A. P., Kinane, C. J., Webster, J. R. P., Holt, S. A., and Lakey, J. H. (2012) Low Resolution Structure and Dynamics of a Colicin-Receptor Complex Determined by Neutron Scattering. *Journal of Biological Chemistry* **287**, 337-346
228. Anandan, A., and Vrielink, A. (2016) Detergents in Membrane Protein Purification and Crystallisation. in *Next Generation in Membrane Protein Structure Determination*. pp 13-28

229. Grishammer, R. (2017) New approaches towards the understanding of integral membrane proteins: a structural perspective on G protein-coupled receptors. *Protein science : a publication of the Protein Society*
230. Moraes, I., Evans, G., Sanchez-Weatherby, J., Newstead, S., and Stewart, P. D. S. (2014) Membrane protein structure determination The next generation. *Bba-Biomembranes* **1838**, 78-87
231. Wiener, M. C. (2004) A pedestrian guide to membrane protein crystallization. *Methods (San Diego, Calif.)* **34**, 364-372
232. Schulz, G. E. (2011) A new classification of membrane protein crystals. *Journal of molecular biology* **407**, 640-646
233. Xu, T. H., Yan, Y., Kang, Y., Jiang, Y., Melcher, K., and Xu, H. E. (2016) Alzheimer's disease-associated mutations increase amyloid precursor protein resistance to gamma-secretase cleavage and the Abeta42/Abeta40 ratio. *Cell discovery* **2**, 16026
234. Nadezhdin, K. D., Garcia-Carpio, I., Goncharuk, S. A., Mineev, K. S., Arseniev, A. S., and Vilar, M. (2016) Structural Basis of p75 Transmembrane Domain Dimerization. *The Journal of biological chemistry* **291**, 12346-12357

VITA

Swe Htet Naing

Swe was born in Mandalay, Myanmar. He graduated from No. (16) Basic Education High School, Mandalay in 2004 with flying colors earning him top eleven ranking in the whole country of Myanmar. Then he went to University of Medicine Mandalay for 2 years where he realized he wanted to pursue research career in Biochemistry. In 2008, he came to United States of America to study Biochemistry at Bates College in Lewiston, Maine. He graduated from Bates College in May 2012 with a B.S. degree in Biochemistry. He then came to Georgia Institute of Technology in Atlanta, Georgia for his PhD degree in Biochemistry. He did his doctorate research on intramembrane aspartyl protease (IAP) under the guidance of Dr. Raquel Lieberman. His PhD research is funded by NSF MCB 0845445 to RLL, NIH R01GM112662 R01GM118744, PEW scholars to RLL, and School of Biological Sciences startup (M.P.T.).